technical note technical note

FAA WJH Technical Center
00093332

Effect of Underwing Frost on Transport Aircraft Takeoff Performance

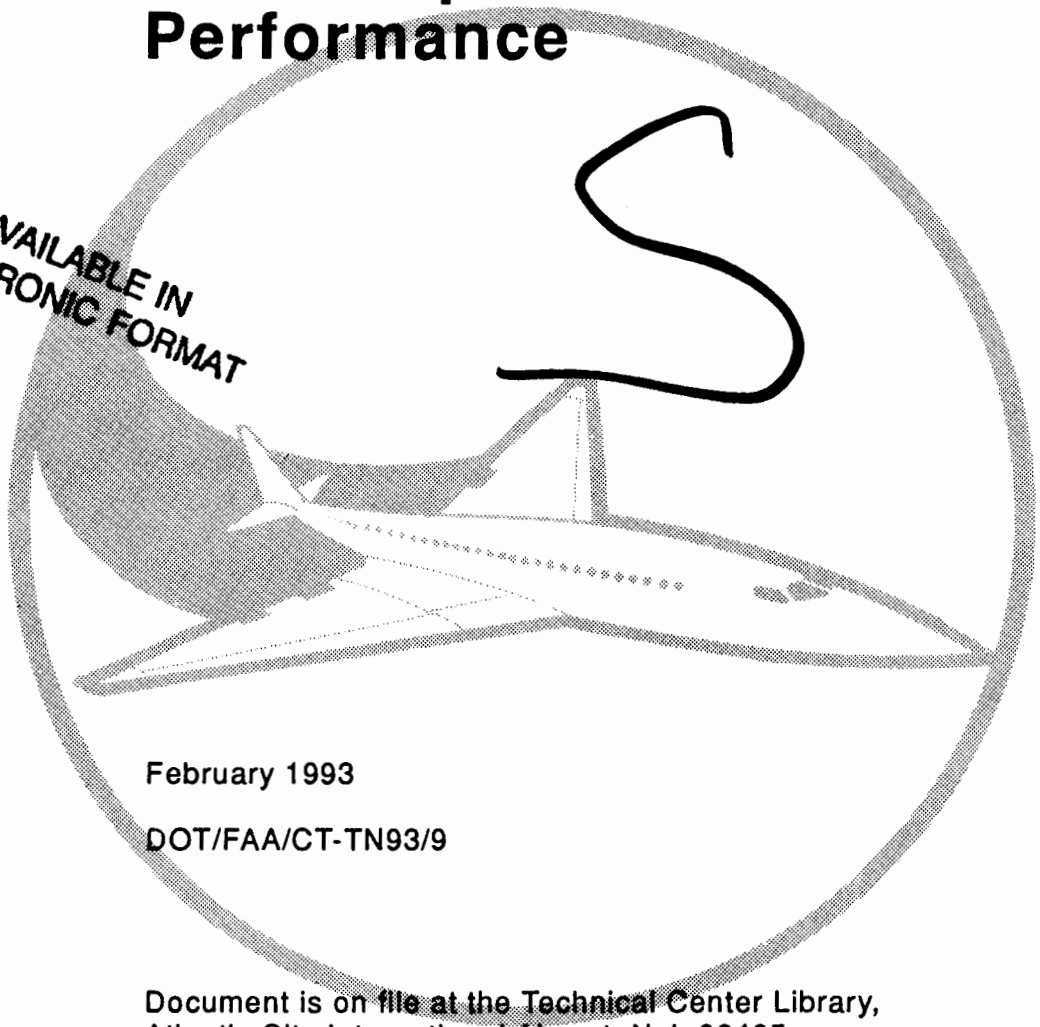

AVAILABLE IN ELECTRONIC FORMAT

February 1993

DOT/FAA/CT-TN93/9

Document is on file at the Technical Center Library, Atlantic City International Airport, N.J. 08405

U.S. Department of Transportation
Federal Aviation Administration

Technical Center
Atlantic City International Airport, N.J. 08405

NOTICE

This document is disseminated under the sponsorship of the U.S. Department of Transportation in the interest of information exchange. The United States Government assumes no liability for the contents or use thereof.

The United States Government does not endorse products or manufacturers. Trade or manufacturers' names appear herein solely because they are considered essential to the objective of this report.

Technical Report Documentation Page

1. Report No.	2. Government Accession No.	3. Recipient's Catalog No.
DOT/FAA/CT-TN93/9		

4. Title and Subtitle	5. Report Date
EFFECT OF UNDERWING FROST ON TRANSPORT AIRCRAFT TAKEOFF PERFORMANCE	February 1993
	6. Performing Organization Code
7. Author(s) Michael B. Bragg and Douglas C. Heinrich	8. Performing Organization Report No.
9. Performing Organization Name and Address Department of Aeronautical and Astronautical Engineering University of Illinois Urbana-Champaign, Illinois	10. Work Unit No. (TRAIS)
	11. Contract or Grant No. DTA03-92-C-00013
12. Sponsoring Agency Name and Address U.S. Department of Transportation Federal Aviation Administration Technical Center Atlantic City International Airport, NJ 08405	13. Type of Report and Period Covered Technical Note
	14. Sponsoring Agency Code ACD-230

15. Supplementary Notes

FAA Project Manager: James T. Riley

16. Abstract

The effect of underwing frost on transport aircraft takeoff and climb performance was studied. Underwing frost occurs when the lower surface of the wing is cooled by cold-soaked fuel in the wing tanks and frost accretes prior to takeoff. A two-dimensional test was performed in the NASA Langley Low-Turbulence Pressure Tunnel on a typical high-lift airfoil with leading-edge slat and trailing-edge flap. Frost was simulated on the lower surface using distributed roughness particles. The test was conducted at a Mach number of 0.2 and chord Reynolds numbers from 5 to 16 million. The effects of the frost were generally small with the largest effects occurring for the slat open case with the frost starting at 12 percent chord. In this situation the frost actually contaminated the upper surface boundary layer. The 2-D data were extrapolated to 3-D for a typical twin-jet and four-jet aircraft. Drag increases were converted into weight penalties to maintain clean aircraft climb angles, and maximum lift penalties were presented as stall speed changes or weight penalties to maintain clean aircraft stall speeds. The largest weight penalties were incurred to maintain the clean stall speed, but all effects were small considering the conservative assumptions made in the analysis.

17. Key Words	18. Distribution Statement
Takeoff Performance Underwing Frost High-Lift Wing	Document is on file at the Technical Center Library, Atlantic City International Airport, New Jersey 08405

19. Security Classif. (of this report)	20. Security Classif. (of this page)	21. No. of Pages	22. Price
Unclassified	Unclassified	92	

Form DOT F 1700.7 (8-72) Reproduction of completed page authorized

ACKNOWLEDGEMENTS

Many people contributed to the success of this program. Steve Wells, then a graduate student at the University of Illinois, was the test engineer on site at NASA Langley for the entire test program. Steve put in long hours on this two shift test and as always performed superbly. At NASA Langley, the program would not have been possible without the generous support of Dr. Steve Robinson. The staff of the Low-Turbulence Pressure Tunnel ran our test very professionally. Bob McGhee generously contributed his expertise to help plan the test and interpret the data. Douglas aircraft contributed significantly by allowing us to use their wind tunnel model. Douglas also provided model support throughout the test. Walt Valarezo and Chet Dominik were extremely helpful in assisting in the test planning and preparation, conducting the test, and in analyzing the results. Their knowledge of high-lift aerodynamics and LTPT testing was invaluable. Thanks also to Ralph Brumby of Douglas for the information he provided on the operational side of the underwing frost problem. Eugene Hill and Thomas Zierten of Boeing were very helpful in the planning stage of the wind tunnel test.

TABLE OF CONTENTS

Section	Page
EXECUTIVE SUMMARY	xi
1. INTRODUCTION	1
1.1 Background	1
2. FROST AND ICE MODELLING	2
2.1 Underwing Frost Locations	4
3. EXPERIMENTAL PROCEDURE AND DATA REDUCTION	4
3.1 Tunnel and Model Description	5
3.2 Frost Simulation and Boundary-Layer Trips	5
3.3 Test Plan	7
3.4 Description of Data and Errors	8
4. AIRCRAFT ANALYSIS METHODS	9
4.1 Example Aircraft	9
4.2 2-D Increments in Drag and Maximum Lift	10
4.3 3-D Drag and Maximum Lift Increments	10
4.4 Takeoff Ground Roll Analysis	12
4.5 Single-Engine Climb	12
4.6 V_{stall} and ΔW From $C_{L,max}$ Analysis	13
5. RESULTS AND DISCUSSION OF THE AIRFOIL DATA	13
5.1 High-Lift Aerodynamics and the Baseline Data	14
5.2 Slat Closed Results	16
5.3 Slat Open Results	17
5.4 Summary	18
6. RESULTS AND DISCUSSION OF AIRCRAFT ANALYSIS	19
6.1 2-Jet Transport	19
6.2 4-Jet Transport	20
7. SUMMARY	21
7.1 Summary and Conclusions	22
7.2 Limitations of the Study	23
7.3 Recommendations	24

8. REFERENCES 25

APPENDIX - REYNOLDS NUMBER EFFECTS

LIST OF TABLES

1	Aircraft frost/ice roughness simulation	28
2	Desired model roughness simulation values	29
3	Actual simulation with measured densities	30
4	Model lower-surface boundary-layer transition strips, "trips"	31
5	Underwing frost test run number matrix	32
6	2-jet aircraft data	33
7	4-jet aircraft data	34
8	Minimum required climb gradients	35
9	Baseline cases for the frost/ice cases modelled	36
10	3-D data uncertainty from 2-D data uncertainty	37
11	Effect of typical frost (simulation 1 and 1a) on the 2-jet aircraft	38
12	Effect of large frost/ice (simulation 2 and 2a) on the 2-jet aircraft	39
13	Effect of large ice (simulation 4) on the 2-jet aircraft	40
14	Effect of typical frost (simulations 1 and 1a) on the 4-jet aircraft	41
15	Effect of large frost/ice (simulations 2 and 2a) on the 4-jet aircraft	42
16	Effect of large ice (simulation 4) on the 4-jet aircraft	43

LIST OF ILLUSTRATIONS

1	MD-80 wing planform	44
2a	B727 wing planform	45
2b	B737 wing planform	46
2c	B747 wing planform	47
2d	B757 wing planform	48
2e	B767 wing planform	49
3	Frost accretion	50
4	Airfoil model in takeoff configuration	51
5	High-lift transport airfoil installed in the low-turbulence pressure tunnel	52
6	Underwing frost simulation installed on the airfoil lower surface from 12-60% chord	53
7	Close-up of the frost simulation with 1/100 in^2 overlay	54
8	Transport aircraft takeoff	55
9	Flow on 2-D high-lift airfoils	56
10	Boundary layer transition modelling	57
11	Reynolds number comparison of drag polars for the slat closed clean airfoil	58
12	Reynolds number comparison of lift curves for the slat closed clean airfoil	59
13	Slat position comparison of drag polars for the clean airfoil at Re=9M	60
14	Slat position comparison of lift curves for the clean airfoil at Re=9M	61
15	Slat open comparison of drag polars for the clean airfoil versus trip 2 at Re=9M	62
16	Slat closed comparison of drag polars for clean airfoil versus trip 2 at Re=9M	63
17	Slat closed comparison of drag polars for frost cases and trip 2 at Re=9M	64
18	Slat closed comparison of lift curves for the frost cases and trip 2 at Re=9M	65
19	Slat closed comparison of drag polars for the ice cases and trip 2 at Re=9M	66
20	Drag coefficient increases from the slat closed trip 2 baseline at Re=9M	67
21	Max lift coefficient increase from the slat closed trip 2 baseline at Re=9M	68
22	Drag coefficient increase from the slat closed trip 4 baseline at Re=9M	69
23	Max lift coefficient increase from the slat closed trip 4 baseline at Re=9M	70
24	Slat open comparison of drag polars for the ice, trip 2 and clean cases at Re=9M	71
25	Slat open comparison of lift curves for the ice, trip 2 and clean cases	

	at Re=9M	72
26	Drag coefficient increase from the slat open trip 2 baseline at Re=9M	73
27	Max lift coefficient increase from the slat open trip 2 baseline at Re=9M	74
28	Drag coefficient increase from the slat open trip 4 baseline at Re=9M	75
29	Max lift coefficient increase from the slat open trip 4 baseline at Re=9M	76
30	Drag coefficient increase from the slat open trip 4 baseline at Re=9M	77
31	Max lift coefficient increase from the slat open trip 4 baseline at Re=9M	78
A.1	Drag coefficient increase from the slat closed trip 2 baseline for large frost/ice	A-2
A.2	Max lift coefficient increase from the slat closed trip 2 baseline for large frost/ice	A-3
A.3	Drag coefficient increase from the slat closed trip 2 baseline for typical frost	A-4
A.4	Max lift coefficient increase from the slat closed trip 2 baseline for typical frost	A-5

NOMENCLATURE

SYMBOL	DESCRIPTION
AR	wing aspect ratio, b^2/S
b	wing span
c	airfoil chord length
C_d	airfoil drag coefficient, Drag/qc
C_D	aircraft drag coefficient, Drag/qS
C_l	airfoil lift coefficient, Lift/qc
C_L	aircraft lift coefficient, Lift/qs
e_0	Oswald's efficiency factor
k	roughness height
	induced drag coefficient, $1/(\pi e_0 AR)$
q	air dynamic pressure, 0.5*air density*V^2
S	wing area
t	frost thickness
T	engine thrust
V	aircraft velocity
W	aircraft weight
x	airfoil chordwise position
y	aircraft spanwise position
α	airfoil or aircraft angle of attack
γ	aircraft flight path angle
Δ	change in a quantity (frost value - clean value)
Λ	wing sweep angle

SUBSCRIPTS

frost	frost case
LOF	aircraft liftoff
max	maximum value
R	aircraft rotation
s or stall	aircraft stall
0	minimum value
1	critical engine failure
2	takeoff climb

EXECUTIVE SUMMARY

The effect of underwing frost on transport aircraft takeoff and climb performance was studied. Underwing frost occurs when the lower surface of the wing is cooled by cold-soaked fuel in the wing tanks and frost accretes prior to takeoff. A two-dimensional test was performed in the NASA Langley Low-Turbulence Pressure Tunnel on a typical high-lift airfoil with leading-edge slat and trailing-edge flap. Frost was simulated on the lower surface using distributed roughness particles. The test was conducted at a Mach number of 0.2 and chord Reynolds numbers from 5 to 16 million. The effects of the frost were generally small with the largest effects occurring for the slat open case with the frost starting at 12 percent chord. In this situation the frost actually contaminated the upper surface boundary layer. The 2-D data were extrapolated to 3-D for a typical twin-jet and four-jet aircraft. Drag increases were converted into weight penalties to maintain clean aircraft climb angles and maximum lift penalties were presented as stall speed changes or weight penalties to maintain clean aircraft stall speeds. The largest weight penalties were incurred to maintain the clean stall speed, but all effects were small considering the conservative assumptions made in the analysis.

1. INTRODUCTION

Transport aircraft usually cruise for extended periods of time at high altitude where the ambient temperature is well below freezing. Under these conditions the fuel in the wing tanks will drop to a very low temperature. The fuel in this case is often referred to as being cold-soaked. When the aircraft descends for landing, the fuel remains at this very low temperature for some time. After landing, the remaining fuel in the wing tanks can cool the wing lower surface to temperatures below freezing. The wing area affected is very dependent upon the amount of fuel remaining, its temperature and the design of the wing structure and the tanks.

If the subsequent ground level humidity is high, moisture in the air will form frost on the aircraft wings in the location of the cold fuel. In some cases, ice may form if the frost partially melts and the water then flows toward the fuselage due to wing dihedral and refreezes. The frost usually occurs on the undersurface of the wing and back from the leading edge. It has generally been believed that the roughness is small and not in a critical location. However, any roughness on a wing will cause an aerodynamic effect. It is well known that frost on the wing upper surface can cause severe aerodynamic and aircraft performance penalties. This investigation was conducted to evaluate the effect of cold-soaked-fuel underwing frost on transport aircraft takeoff performance and to calculate aircraft weight penalties, if any, to return the aircraft to its original clean-wing performance.

1.1 Background

Many researchers have studied the effect of roughness on airfoils, wings and aircraft performance. Ljungstroem[1] studied experimentally the effect of upper surface frost on 2-D airfoil performance. These airfoils had high lift devices, but only upper surface and leading-edge frost was investigated. Bragg[2] looked at the effect of roughness from several different sources on laminar flow airfoils. While this study did include some consideration of overall aircraft performance, again only leading-edge roughness was considered. A correlation of roughness effects on maximum lift was presented by Brumby[3]. This study also considered only upper surface and leading-edge roughness. Lynch et. al.[4] conducted experimental measurements on a multi-element airfoil with a leading-edge device and roughness in the NASA Langley Low-Turbulence Pressure Tunnel. Testing over a range of Reynolds numbers from 2.5 to 18 million, they noted difficulty in applying low Reynolds number data to high Reynolds number applications. These studies, and many more not discussed here, all have investigated the effect of leading-edge or upper surface frost or roughness. Results on lower surface frost effects on aerodynamics are not available.

Computational and empirically based studies of frost and roughness effects have been performed with upper surface and leading-edge roughness. Bragg[5] and later Kind[6]

developed 2-D computational methods to predict roughness effects on single-component airfoils. While neither study looked at lower surface frost, the methods are appropriate for such an application. Kind also reports some detailed work on classifying frost by its effect on the turbulent boundary layer. Studies on the effect of frost or roughness on the takeoff performance of aircraft have been reported by Dietenberger[7] and van Hengst and Boer[8]. Both of these reports use empirical methods based on experimental data as input to computational takeoff analyses. Therefore, the analysis methods have been developed, but what is missing is the experimental data on lower surface roughness or frost effects on airfoils.

2. FROST AND ICE MODELLING

In an effort to determine the effect of frost on the bottom surface of a transport aircraft wing it is first necessary to model the frost accurately. To achieve this, papers pertaining to frost have been studied to determine the proper range of the roughness height to chord ratio and density values.

Brumby[3] reports that at the lower limit of frost formation the frost grains have an effective diameter of approximately 0.004". The frost continues to grow to 0.015" at which point further growth is usually in the form of frail needles. Thompson[9] and Langston[10] both discuss the large needles and their tendency to be blown off during the takeoff run. Thompson[9] states that these needles usually blow off at speeds from 20 to 40 mph. Langston[10] found that typical frost grains were from 0.003 to 0.015 inches in height on metallic surfaces and slightly smaller on painted surfaces. "Spikey" frost needles[9] have sizes up to 1/8 or even 1/4 inches.

A later study conducted by Kind and Lawrysyn[6,11] revealed that frost samples as thick as 1 mm (0.039") could be grown on flat plates. This was the largest value of frost reported by Kind. Kind's study was the most extensive frost study conducted in the last few years and he chose a frost height of 0.4 mm as a typical value. However, van Hengst and Boer[8] tested simulated frost which corresponded to a frost height of 2.0 mm on a Fokker 50. This work preceded Kind's frost study, and their choice of 2.0 mm is not consistent with the recent frost data.

Langston[10] and Brumby[12] both discuss the phenomenon of frost growth building upon the lower layers. This building upon itself leads to the difference between the thickness of the frost and the aerodynamic roughness height. Figure 3 sketches this concept where t is shown as the frost thickness and k the aerodynamic roughness height. This distinction is important for the very thick frost sometimes measured, but is seldom made in the literature. While the overall thickness may cause some very small changes in the wing contour, it is the aerodynamic roughness that causes the aerodynamic

penalties. In the work performed here, it is the aerodynamic roughness height which was simulated.

To model the frost correctly, it is also necessary to model the frost density. According to Kind's study[6,11], the full-scale densities for the heights considered range from 12 to 30 particles per square inch. In determining a density, Kind counted only the highest 20 percent of the frost grains. These frost roughness density data are the most reliable available. By scaling this for the model an accurate representation can be obtained for the model frost.

Another problem which must be considered is how to model the case of melting and refreezing of the frost. Frost on the outboard lower surface, where the amount of fuel in the tanks may be small, can melt as the surface gradually becomes warmer. The water droplet from the melted frost then run towards the wing root due to the wing dihedral and eventually refreeze in a droplet type shape[12]. Ice may also form due to water splashed up onto the wings from the runway[12]. Very little data is available on this subject, but a plausible result would be a lower roughness density than the frost with a roughness consisting of frozen droplets with a height on the order of 1/16 to 1/8th of an inch.

Table 1 summarizes the recommended frost/ice values to be simulated for the test. Note that an average full-scale chord of 12.21 ft was used to nondimensionalize the roughness heights. Simulation #1 is a typical frost grain size and is similar to that used by Kind[6]. Simulation #2 provides an upper bound on frost grain roughness and a simulation of ice beads. Simulation #2 is referred to as large frost/ice. Simulation #3 was not tested and is, therefore, not presented. Simulation #4 is a worst case simulation and can be interpreted as the situation in which the frost melts and the water droplets refreeze. Simulation #4, which is 1/8th inch full scale, may be larger than is seen in practice, but is included as an upper bound on the frost/ice roughness problem. Simulation #4 is referred to as large ice.

The weight of the frost should also be considered. Thompson[9] provided measurements of the weight per unit area of several actual frost accretions. Although these data are difficult to relate to the 3 frost/ice simulations proposed here, a very approximate number in terms of grams of frost per square foot is given in Table 1.

Applying the roughness, particularly the very small grit, is very difficult. Sandpaper was considered as a possibility for modelling the frost as Ljungstrom[1] had done. However, sandpaper has a backing which is too large, and which would appear as a 2-dimensional step. Applying sandgrain roughness directly to the model surface with adhesive was also considered, but according to Kind[6,11], the ratio of sandgrain height to frost height varies widely. Also, if sandgrain roughness were to be used, the amount of grit to be applied would be excessive and difficult to apply. Consequently, considering the problems involved with the sandgrain roughness and the range of model frost heights necessary, it appears the logical choice is to use either Ballotini beads or grit. This

combination was shown to successfully model frost on the upper surface of this model in tests run by Lynch and Valarezo[4]. The exact method for applying and documenting the roughness is discussed in a later section.

2.1 Underwing Frost Wing Locations

Underwing frost forms on the wing undersurface of transport aircraft when the cold fuel remaining in the wing tanks cools the lower surface. Thus, it is necessary to know the wing tank locations to predict the region of possible frost formation. The wing fuel tanks are located between the wing spars and extend from the wing root toward the tip. Information on the wing fuel tank location for various aircraft was requested from Boeing and Douglas Aircraft.

The information in Figs. 1 and 2 are what was received. Figure 1 shows the wing spar location on a MD80 wing. The fuel tank is assumed to occupy the entire chordwise extent between the spars. This is approximately from 12 to 60 percent chord. No information on the spanwise extent of the wing tanks was obtained. Information on the various Boeing aircraft which was received is presented in Fig. 2. For the Boeing aircraft the forward spar, and therefore the forward tank location, is at approximately 20 percent chord. The most aft location of the wing tanks is approximately 60 to 65 percent. The tanks extend from the wing root to approximately the 70 percent span location.

3. EXPERIMENTAL PROCEDURE AND DATA REDUCTION

To evaluate the effect of underwing frost on aircraft takeoff performance, it was first necessary to determine what type of wind tunnel test should be performed. The ideal case would have been to perform a 3-D test at the correct R_e. However, the facilities to test a 3-D model at the correct R_e do not exist, and even if such facilities did exist, this type of test would be prohibitively expensive. The second level is to test a 2-D airfoil at the correct R_e and to extrapolate the results to 3-D. This type of test allows the roughness to scale geometrically with the wing chord since the boundary layer scales geometrically. The lowest level would have been to conduct the test on a transport airfoil section in a low-speed wind tunnel. This type of test would have required complex frost scaling and extrapolation to the correct R_e. However, since drag is sensitive to R_e, and the added complexity of a 3-D test would be aircraft dependant, the 2-D test at the correct R_e was chosen.

It should be noted that the Reynolds numbers tested were low for large transport aircraft. However, since the k/c values were based on a chord for a typical small transport, these effects tend to cancel. That is, for the large transports the k/c values for a given frost simulation are too large. Then testing at a low Reynolds number where

the boundary layer is too thick, provides reasonable scaling of k to the boundary-layer thickness.

3.1 Tunnel and Model Description.

A typical high-lift transport airfoil was tested at the Low-Turbulence Pressure Tunnel (LTPT) at NASA Langley Research Center in Hampton, Virginia. The LTPT is a single-return closed throat wind tunnel with a 3' wide, 7.5' long and 7.5' high test section. It is capable of running at pressures up to 10 atmospheres to increase the density, and consequently, allow tests at Reynolds numbers near flight at low subsonic Mach numbers typical of takeoff and climb. Boundary-layer suction was used on the sidewalls to maintain the two-dimensionality of the model flowfield.

The airfoil model used in this study was representative of current supercritical airfoils in use on transport aircraft. Specifically, the airfoil consisted of a leading-edge slat, a main element and a single-element flap. The cross section is shown in Fig. 4. The airfoil had a chord of 22" and spanned the 3.5 ft wide tunnel test section. This model was made available by Douglas Aircraft Company and designated LB-546F. Figure 5 shows a photograph of the model in the tunnel. The airfoil was tested with the slat deflected 20 degrees and the flap deflected 15.6 degrees. Flap and slat gap geometry is defined in Fig 4. The airfoil was tested with the slat open and closed to model typical current, and possible future, airfoil takeoff configurations.

The aerodynamic coefficients were measured by instrumenting the airfoil with a centerline tap row with 142 taps. The surface pressures were measured and recorded using a personal computer interfaced with an electronically scanned pressure system. The pressure distribution was integrated to obtain airfoil lift and pitching moment coefficients. The model lift coefficient was also available from the facility sidewall balance system. Other balance components were not reliable due to the operation of the sidewall suction system. Balance lift coefficient compared well with the pressure data, however, only pressure derived lift data are presented in this report. The drag coefficient data was obtained from a wake survey probe downstream of the model and on the model centerline. The probe measured the local flow total pressure, static pressure and flow direction. These values measured through the wake are integrated to obtain the airfoil drag coefficient.

3.2 Frost Simulation and Boundary Layer Trips

Using the mean aerodynamic chord for the typical twin-jet aircraft studied, and a model scale of 0.15, the heights and densities of the frost were geometrically scaled. This maintained the ratio of the roughness height to chord ratio and the same number of roughness elements per nondimensional area. This process resulted in the values of density and roughness height presented in Table 2. The frost or ice simulations used extended from the 12 to 60 or 20 to 60 percent chord location on the lower surface of the

airfoil. The 12% and 20% chord values for the leading edge of the frost were chosen because they correspond approximately to the range of values for the leading edge of the main fuel tanks in current transport aircraft, Figs. 1 and 2. The 60% chord location corresponds to the trailing edge of the fuel tanks for typical current transport aircraft. Figure 6 shows the lower surface of the model with roughness applied from 12 to 60 percent chord. Note the presence of the large slat and flap support brackets on the model. Roughness was not applied on the model lower surface between the tunnel wall and the first set of brackets on each side.

The frost on the undersurface of the wing was modelled using Ballotini beads. Ballotini beads were chosen because of their low variance in diameter and their availability in the required sizes. A practical problem was to find a fast and accurate way to apply the roughness to the model to achieve the desired densities for each of the specified roughness heights. The problem of application was further complicated by the fact that the roughness elements had to be applied to the airfoil's undersurface while the model was installed in the tunnel.

To solve this problem, a roughness applicator was designed to provide a uniform distribution of the roughness elements. This was achieved by supplying low-pressure air to a pressure vessel with a diverging nozzle at the exit. The air pressure into the device was regulated and usually approximately 10 psig. The pressure vessel was partially filled with Ballotini beads prior to the application. By directing the nozzle upward and pressurizing the vessel, roughness elements were applied to the model lower surface.

The proper adhesive for applying the roughness was also studied and several options were considered. The first of these was hair spray. Hair spray is water soluble and is, therefore, attractive since hazardous chemicals are not required to remove it from the model. However, this option was not chosen because it was felt that the high dynamic pressure in the tunnel required a better adhesive for the roughness.

The next approach considered was to use spray paint for the adhesive. However, there was concern that the thickness of the paint would be as large as the smallest grit. Therefore, the thickness of typical paint applications were measured and several averaged to obtain a value of paint thickness of 0.0005 in. This was well below the smallest diameter grit tested of 0.003 in. The first paint tested was clear coat. However, the photographs used for documentation showed that clear adhesives did not obscure finishing marks on the aluminum model making the roughness difficult to see. When colored spray paints were used the grit was more visible. Red spray paint was chosen because it provided the best combination of adhesive and visual characteristics.

The final problem addressed was how to achieve the correct density during application. A near-real-time method was required. Magnifying glasses and video cameras were considered, but neither proved to be satisfactory. Therefore, it was decided that after an application of roughness, a 35mm camera with a 1:2.5 macro lens

and 10X teleconverter would be used to spot check several locations to verify the density of roughness elements. A clear plastic ruler with a grid of 0.01 in^2 squares inscribed was laid on the surface to supply a reference area. From this spot check, areas requiring further modification were identified and corrected. This process was continued until an acceptable roughness distribution was achieved for the 12% chord case. Once the 12% chord cases were run for a given frost case, the 12% chord to 20% chord portion of the roughness elements was removed from the model. This was done for ease of application and to provide the same density for the 12 and 20% chord cases.

Finally, using the camera the roughness elements were photographed at 20 stations. Six of these locations were equally spaced on each side of the centerline tap row and the remaining 8 locations were located between the outer flap brackets with 2 leading and 2 trailing edge locations on each side. A typical close-up photograph of the roughness used to document the density is shown in Fig. 7. This is simulation #2 with a roughness element size of 0.009 in. and an average density of 480 particles/in^2. Using the photographs, the roughness elements per unit area were counted and averaged to provide an applied roughness density value, Table 3.

Due to the wing sweep and pressure gradients on the wing lower surface, it was believed that the airfoil lower surface boundary-layer should be turbulent from the attachment line. Boeing flight tests[13] had indicated that the undersurface was turbulent from the attachment line. However, the lower-surface boundary layer on 2-D high-lift models are known to have extensive laminar flow. Therefore, for proper aerodynamic simulation, the boundary-layer transition on the lower surface had to be fixed. It was decided to place the trip at the same locations as the leading edge of the frost. This would provide correct baselines for comparison of the aerodynamic coefficients.

The boundary-layer trip strip height was evaluated using the method outlined by Braslow[14]. Using this method, the required trip strip height was calculated given the desired transition location, Mach number and Reynolds number at the trip location. The trip was formed by applying a strip of the red paint adhesive 1/8 inch wide in the chordwise direction. The appropriate grit size was then applied at the desired density and documented in the same way as the frost simulations. The trip values used are presented in Table 4.

3.3 Test Plan

The plan for the test involved running alpha sweeps on a number of model configurations at various Reynolds numbers. Initially, a Reynolds number of 16 million was to be the primary Reynolds number with some runs at 5 and 9 million for Reynolds number sensitivity tests. However, through much of the test program, the main air compressor at the tunnel was not operational and a smaller compressor was used. The smaller compressor had difficulty maintaining the required tunnel pressure for R_e = 16 million and required an excessive time period to reach this pressure. As a result, data

were also acquired at 12 million and the primary Reynolds number for the test was reduced to 9 million to save time. Earlier research by Lynch et. al.[4] had shown the Reynolds number effects on a similar model to be small in most cases between 9 and 16 million.

For all cases, the slat was set to 20 deg. and the flap was set to 15.6 deg. The slat was set in both the open and sealed configuration for the test. Ballotini beads were applied as a trip strip to produce the proper boundary-layer state or to simulate the frost or ice. Since most current transport aircraft takeoff slat sealed, slat open data were only taken at one Reynolds number, 9 million.

Several model configurations were tested. These included the baseline cases of the clean model with no transition strips or frost. Next, to model the turbulent boundary-layer on the undersurface of the airfoil, 3 transition strip configurations were tested. To model the frost, 5 different configurations were tested. These include typical frost from 12-60% chord and 20-60% chord, large frost/ice at 12-60% chord and 20-60% chord and large ice from 12-60% chord. The configurations which were run and the Reynolds numbers tested are summarized in Table 5.

3.4 Description of Data and Errors

Using the test set-up described, data were taken at angles of attack ranging from 0 to 20 deg. At each angle-of-attack, the tunnel conditions, surface pressure data and balance data were recorded. The pressure distribution was integrated to obtain the sectional lift coefficient and the sectional pitching moment coefficient. At all angles of attack, except those near stall, wake surveys were taken from which the sectional drag coefficient was obtained. Since it was known that the airfoil drag coefficient around V_2 would be very important in the later analysis, 2 wake surveys were take at 9, 10 and 11 degrees angle of attack. These values were later averaged to improve data quality.

Repeatability tests were performed by taking two or more measurements while fixed at a given test condition and for a few configurations by repeating an entire angle-of-attack sweep, a test run. Repeating entire runs showed that the maximum lift coefficient was repeatable to within 0.03, and repeating specific data points showed that the sectional drag coefficient was repeatable to within 2 drag counts (0.0002). While these values are small, the uncertainty in the data was of the same order of magnitude as the increments observed from the addition of frost.

All of the coefficient data were corrected for tunnel wall and blockage effects using the method outlined in Rae and Pope[15]. This was performed by NASA LTPT personnel using standard procedures. The data presented in this report have all been corrected for tunnel wall interference and blockage effects.

4. AIRCRAFT ANALYSIS METHODS

Using the 2-D data acquired in the LTPT, it was necessary to extrapolate the results to typical transport aircraft. Two hypothetical aircraft were used for the study; a twin-jet aircraft with a gross weight of 140000 lbs. and a 4-jet aircraft with a gross weight of 775000 lbs. Using these aircraft, it was possible to bracket the range of aircraft that were expected to be affected by this phenomenon. A summary of the values used to model the aircraft is presented in Tables 6 and 7. Figure 8, modified from a similar figure from McCormick[16], shows a transport aircraft takeoff including the airspeeds and climb segments defined in the FAR's. The most important terms for the present analysis are: 1) V_2 - the takeoff climb speed which must be attained by the aircraft at or before reaching an altitude of 35 feet, 2) first segment climb - the part of the takeoff climb between when the aircraft reaches V_{LOF} and when the landing gear is retracted, and 3) second segment climb - the part of the takeoff climb between gear retraction and flap retraction (attaining the enroute aircraft configuration).

4.1 Example Aircraft

Since actual aircraft performance values are proprietary, and this study was to be applicable to all transport aircraft, it was decided to use aircraft performance values which correspond to typical values an aircraft of a given class might have. Since, the formation of the underwing frost requires the aircraft to become cold soaked at altitude, this phenomenon primarily effects jet transports and only jet transports were considered in this study. Further, to cover the range of jet transports currently flying, the study was performed on a typical twin-jet and a typical 4-jet aircraft.

To model these aircraft, it was necessary to define the configuration data, the thrust model, the drag polar, and the takeoff velocities. The configuration data were defined by identifying the values of actual aircraft in the specified classes and then selecting representative values. This method was used to obtain the reference area, the span, the aspect ratio, the tip and root chords, the dihedral, and the fuel tank locations.

The thrust model was created by geometrically scaling an equation presented by McCormick[16]. This equation relates the thrust to the velocity of the aircraft for a typical jumbo jet. To scale the thrust model, the maximum static thrust desired was defined and the coefficients of the thrust model were multiplied by the ratio of the maximum static thrust required over the max static thrust presented by McCormick. These thrust equations were then used to calculate the takeoff and climb performance of each aircraft and are of the form

$$T = A \times V^2 + B \times V + C$$

FAA WJH Technical Center
00093332

The drag polar of the aircraft studied was generated by following a method outlined by Lan and Roskam[17] which predicts the drag polars of aircraft for preliminary design purposes. Using the configuration data for the aircraft, the parasite drag coefficient was built up considering contributions from the fuselage, the engines, the horizontal and vertical tail and the wing. To predict the induced drag, an Oswald's efficiency factor of 0.6 was assumed, and the induced drag coefficient was calculated.

The takeoff velocities were calculated by first evaluating the 1-g stall speed for each aircraft. By following the Federal Aviation Regulations part 25, it was possible to define minimum velocities in terms of the stall speed for each of the takeoff velocities defined in part 25. The actual values of the takeoff velocities for the 2 hypothetical aircraft were chosen to be somewhat higher than the minimum values allowed, as is typical practice. It should be noted that FAR part 25 bases the takeoff velocities on a flight test obtained stall speed that is about 6% higher than the 1g stall speed[17] given in Tables 6 and 7. This explains why V_1 and V_R in Table 7 are less than V_{s1g}.

After completing the procedure described above to determine the aircraft values, the 2 aircrafts' single-engine-out takeoff and climb performance was calculated. It was found in both cases that the aircraft were both second segment climb limited. Since the intent was to be conservative in the analysis, thrust values were adjusted for both aircraft to fix their single-engine out climb performance in segment 2 at the minimum value allowed.

4.2 2-D Increments in Drag and Maximum Lift

To calculate the 2-D increments in drag and maximum lift, it was necessary to first choose an appropriate baseline for each case. The increment in $C_{l,max}$ was evaluated by subtracting the highest C_l value recorded for the appropriate baseline case from the highest C_l value recorded the frost/ice case. For the drag increment, the most critical case is the effect of drag on the first and second segment climb performance. This corresponds to a velocity V_2 which was estimated to occur at a lift coefficient in the range of 2.55 to 2.65. It was assumed that the aircraft would continue to be flown at the velocity V_2, therefore the drag increment should be calculated at fixed lift coefficient, not at fixed angle of attack. The drag was interpolated for the frost and baseline cases to obtain drag coefficients at lift coefficients of 2.55, 2.60 and 2.65. From the frost/ice drag coefficient values at these 3 lift coefficients the baseline values were subtracted to obtain 3 drag coefficient increments. These 3 increments were then averaged to obtain a single value of ΔC_d.

4.3 3-D Drag and Maximum Lift Increments

Once the 2-D increments were obtained, the values were extrapolated to 3-D values of $\Delta C_{L,max}$ and ΔC_{D0}. Initially, a nonlinear lifting line method was attempted as a means of calculating the 3-D values from the 2-D measurements. However, due to

spanwise viscous effects not modelled by this simple inviscid scheme, the results were unsatisfactory. No other simple computational methods were available to obtain 3-D lift and drag values on a swept wing from 2-D data. Therefore, simple preliminary design methods were used to estimate the 3-D aircraft values of lift and drag due to the frost.

To achieve the maximum lift increment from the 2-D values the preliminary design method from Raymer[18] was used. Raymer's method was intended to estimate the change in aircraft 3-D maximum lift due to the deployment of a partial span high-lift system for which the sectional maximum lift coefficient was known. The method was modified for use here, and assumes that the frost affects only that part of the wing which has a high-lift system. That is, that the frost covers the entire lower surface of the wing under the fuel tanks and that this is exactly the same part of the wing which has trailing-edge high-lift devices. The equation used after modification is

$$\Delta C_{L_{MAX}} = \Delta C_{l_{max}} \times \cos\Lambda \times \frac{S_{frost}}{S}$$

The drag of subsonic aircraft is often represented using a drag polar of the form

$$C_D = C_{D_o} + \frac{C_L^2}{\pi e_0 AR}$$

With the first term representing the parasite drag and the second term the induced drag or drag due to lift. Before flow separation occurs on the wing, the addition of frost can be considered as an increase in the skin friction of the area of the wing affected, S_{frost}. Consequently, an increment due to the frost was applied only to the parasite drag, and to be conservative, the ratio approach used by Raymer to estimate maximum lift was utilized without the cosine term. Therefore, the equation used to modify the parasite drag term C_{d0} was as follows

$$\Delta C_{D_o} = \Delta C_{d_o} \times \frac{S_{frost}}{S}$$

Note then that no change was made in the induced drag term due to the frost since this effect was assumed to be small. However, the drag polar is of primary importance only in the lift coefficient range about V_2, therefore the ΔC_{d0} value used in the above equation is that taken at lift coefficients about V_2 as described in section 4.2 above. Assuming the effect of frost on the induced drag is indeed small, this procedure should provide an excellent modified drag polar in the range of interest.

4.4 Takeoff Ground Roll Analysis

Using the 3-D increments in $C_{L,max}$ and C_{D0}, these values were applied to the example aircraft to determine the effect of the frost on the ground roll distance during takeoff. A computer program to calculate takeoff performance based on the solution of the governing ordinary differential equation as formulated by McCormick[17] was written. It was assumed that an engine was lost at V_1 during the takeoff roll and the aircraft proceeded to liftoff at V_{LOF}. It is well known that drag plays a secondary role in determining aircraft takeoff ground roll. The maximum drag increase predicted only increased the calculated ground roll by 15 feet. Therefore, the effect of underwing frost on takeoff distance was negligible and the data will not be presented here.

4.5 Single-Engine Climb

The example aircraft in Tables 6 and 7 used in this study both just met the second segment, one-engine-out climb requirements for their class, Table 8. If underwing frost exists on an aircraft, and the parasite drag is increased, the aircraft climb angle will be decreased. An adjustment must be made or the aircraft climb angle may fall below that required by part 25. If it is assumed that the aircraft climbs at the same calibrated airspeed, an aircraft weight reduction can be calculated which will allow the frosted aircraft to maintain the same climb angle as the clean aircraft. Therefore, a lighter aircraft at the same airspeed has a reduction in the climb lift coefficient. For small climb angles this results approximately in a reduction in the induced drag to balance the increase in parasite drag due to the frost.

To determine the aircraft weight to maintain the same climb performance, first note that the climb angle is given by

$$\sin\gamma = \frac{T-D}{W}$$

Setting the climb angle with and without frost equal, assuming that the aircraft velocity, air density and thrust are the same with or without the frost, the required change in the aircraft weight can be shown to be

$$k\Delta C_L^2 + (2kC_L + \sin\gamma)\Delta C_L + \Delta C_{D_0} = 0$$

where

$$\Delta C_L = \frac{\Delta W}{qS}$$

and k is the induced drag coefficient ($1/(\pi e_0 AR)$), q is the dynamic pressure, S is the reference area, γ is the clean (baseline) one-engine-out climb angle, ΔC_{D0} is the change in the parasite drag coefficient, and C_L is the original lift coefficient.

The procedure used to calculate the weight penalties for both segment 1 and segment 2 one-engine-out climbs was the same. First, the climb angle for that segment for the clean (baseline) aircraft at maximum gross weight and maximum thrust was calculated. Next, the modified drag polar for the underwing frost case of interest was found. Then the equation above was used to calculate the change in weight required with frost to maintain the same climb angle.

4.6 V_{stall} and ΔW From $C_{L,max}$ Analysis

Since the losses in $C_{L,max}$ are small for underwing frost, primarily the stall margin is effected. To evaluate the loss of the stall margin, the increase in the 1-g stall speed resulting from the loss of $C_{L,max}$ was evaluated. The stall speed of a transport aircraft is required to be known to within 0.5 knots. Therefore, examining the change in stall speed due to underwing frost provides insight into the magnitude of the effect on maximum lift. The following equation was used to calculate the change in the stall speed due to the change in $C_{L,max}$.

$$\Delta V_S = V_S\left[\left(\frac{C_{L_{max}}}{C_{L_{max}} + \Delta C_{L_{max}}}\right)^{1/2} - 1\right]$$

Another approach which was considered was to create a weight penalty to restore the original stall margin. This was done by setting the stall speed constant for the aircraft with and without frost. Thus, an aircraft climbing out at V_2 will have the same margin to V_{stall} with or without underwing frost. Therefore as $C_{L,max}$ is lost, the maximum gross takeoff weight was reduced to compensate for this effect. The analysis resulted in the following relation.

$$\Delta W = \frac{\Delta C_{L_{max}}}{C_{L_{max}}} W$$

5. RESULTS AND DISCUSSION OF THE AIRFOIL DATA

This section presents the data obtained at the LTPT. First, a brief discussion of some of the more important aerodynamic concepts is presented. Then the high-lift airfoil data with simulated frost is compared to the various baseline data.

5.1 High-Lift Aerodynamics and the Baseline Data

For a two-dimensional four-element airfoil, the major characteristics of this flowfield are identified in Fig. 9[19]. The main points of interest for this study are the attachment line and the laminar bubble on the main element. The airfoil shown here is taken from a section of a 3-D swept wing. The attachment line on a 3-D wing is the equivalent of the stagnation point on a 2-D airfoil. However, the spanwise flow is not brought to rest, hence, it is not a true stagnation point, but an attachment line. Forward of the attachment line, the flow goes over the upper surface and below or aft of this line it flows back over the lower surface.

Transition on a swept wing is different than on a 2-D airfoil or a straight wing. Additional transition mechanisms exist which tend to promote much earlier transition. Note that Mack and McMasters[19] show transition at the attachment line in Fig 9. This is usually the case on the lower surface where the lower-surface boundary layer is turbulent everywhere aft of the attachment line. However, in the upper-surface boundary layer the situation is more complex. It is important to remember that the upper-surface boundary layer starts at the attachment line, which is actually on the lower surface, and flows up around the leading edge and over the upper surface. The upper-surface boundary layer may: 1) start as a laminar layer and transition somewhere downstream, 2) start as a turbulent layer and continue as such to the trailing edge, or 3) start as a turbulent boundary layer, relaminarize and later transition back to a turbulent boundary layer. Figure 9 shows case 3.

Figure 9 shows a laminar separation bubble on the upper-surface leading edge. Laminar bubbles occur when a laminar boundary layer experience an adverse pressure gradient which forces it to separate. The boundary layer then separates from the surface, transition occurs in the free-shear layer and the boundary layer reattaches as a turbulent boundary layer. Laminar bubbles can often be observed as a very small constant pressure region on the surface and cause a small increase in the airfoil drag.

With the slat open, the leading edge of the main element aerodynamically effects the upper surface of the airfoil. This is important to note, because the attachment line location varies with the angle of attack, and therefore, care must be taken when modelling the lower-surface boundary layer. The attachment line will move further back as the angle of attack is increased. If a trip strip is placed too far forward on the model lower surface, and the slat is open, the trip will affect the upper surface and will not cause transition of the lower-surface boundary layer. This is shown in Fig. 10. Additionally, it will be shown that the attachment line location does not noticeably effect the closed slat case, but for the open slat case there is a noticeable effect on the drag when the attachment line moves aft of the trip strip.

Figure 11 and 12 show the lift coefficient plotted versus the drag coefficient (drag polar) and the lift versus the angle of attack for the clean airfoil. These figures show that

as the Reynolds number was increased the drag coefficient was reduced at a given lift coefficient. This was especially true in the 5-9 million range of Reynolds number. Figure 4 shows the corresponding effect on the maximum lift coefficient. A small increase in $C_{l,max}$ occurs between 5 and 9 million Reynolds number with less variation seen in the 9 to 16 million range. The effect on the lift curve slope is minimal. This result combined with the problem of boundary-layer scaling of the roughness was the reason that this test was performed at near-flight Reynolds numbers.

It is also important to understand the aerodynamic effects of opening the gap between the main element and the leading edge slat. The effect on the sectional drag coefficient is shown in Fig. 13. This figure shows that opening the slat increases the minimum drag, but allows lower drag at high lift coefficients. The location of the intersection of these curves may be Reynolds number and configuration dependent. Takeoff with the slat open may improve the takeoff performance for some configurations and is used on some recent designs. Therefore, it was necessary to run both the slat sealed and the slat open cases in this study. The slat open case also has a higher maximum lift coefficient than the slat closed case, Fig. 14. Many aircraft which takeoff slat sealed provide automatic opening of the slat gap at a set high angle of attack to take advantage of the higher maximum lift as a safety feature.

Using the information stated about the flow interactions, and the fact that the attachment line varies with the angle of attack, Fig. 15 shows an interesting phenomenon. Note, at lift coefficients greater than 2.4 (angles of attack greater then 8 deg.), the 12% transition strip case has a significantly lower drag than the clean case. It is believed that this indicates the presence of a laminar separation bubble on the clean airfoil main element as indicated in Fig. 9. Therefore, in this range of lift coefficient it appears that the attachment line has moved aft of the trip strip. In doing this, the trip strip now transitions the flow on the upper surface from laminar to turbulent. This eliminates the laminar separation bubble and reduces the drag.

Figure 16 shows the same case, but with the slat gap closed. For this case, there is no flow around the leading edge of the main element, and thus the transition strip does not alter the flow in the upper surface boundary layer. Here the trip strip causes only a small drag reduction. These plots show that the transition location is not as critical for the slat closed case as it is for the slat open case. Also, from the slat open case, it is possible to see that for an accurate estimate of the effect of frost on drag, one must determine if a laminar separation bubble actually exists on the 3-D transport aircraft wing of interest. However, the information on this point available in the open literature is inconclusive. Therefore, the laminar bubble must be considered when determining the proper baseline case for comparison.

In determining the proper baseline for comparison to a frost simulation, 3 factors must be considered. These are whether the slat is open or closed, the location of the frost simulation (12-60 or 20-60 percent) and whether the baseline is to be with or without

a laminar separation bubble. The various baselines used are shown in Table 9. When the slat was closed, no bubble was present in the experiment and, therefore, all slat closed cases are for no bubble. If the frost starts at 12 percent, the data with a boundary-layer trip at 12 percent (trip#2) is the proper baseline. For the frost starting at 20 percent, the trip#4 baseline is used. Note that trip#3 data for a larger trip at 20 percent were taken. However, the drag data for this trip were somewhat large, due probably to too large a grit size on this trip.

The slat open case has 4 possible baselines when the 2 frost locations tested are considered in combination with the possibility that a bubble may or may not exist. The trip#4 data with the trip at 20 percent chord did not affect the bubble and is used as the baseline for the bubble present case. The no bubble case uses trip #2 or #4 depending on the starting location of the frost simulation.

5.2 Slat Closed Results

The main results obtained from the 2-dimensional test for the slat closed case are presented in Figs. 17-23. These results are presented in several forms. For several typical sets of data, the drag polar and the lift curves are presented. Using, these curves, as well as other pertinent data sets, the data were reduced to increments of the lift coefficients and drag coefficients from specified baseline cases.

Figures 17-19 present the lift and drag results for the slat closed baseline, the large frost/ice case, and the typical frost case. From Fig. 17, it is possible to see that increments in the sectional drag taken at a constant sectional lift will vary with the lift coefficient at which the increment is evaluated. Further, it was found that sectional loading during climb at V_2 is typically in the range of lift coefficients from 2.55 to 2.65. Therefore, the drag increments presented later were averaged over this range.

The effect of the frost on the sectional lift coefficient is shown in Fig. 18. It should be noted that the lift curve slope was reasonably unaffected by the frost size, but the maximum lift coefficient was usually reduced slightly as the frost size was increased. Note, however, that the typical frost case actually had a slightly higher maximum lift coefficient than the baseline, trip #2 case. The increase was within the experimental error quoted earlier of 0.03. Next, Fig. 19 shows the effect of frost/ice size on the drag polar. The large ice simulation produces approximately a 10 count drag increase in the lift coefficient range around V_2. However, the large ice simulation was intended as a worst case and may be unrealistically large compared to actual operations.

In Figs. 20-23, the data are reduced to increments of sectional drag and sectional lift coefficients from the baseline case. Remember that ΔC_d and $\Delta C_{l,max}$ are calculated by subtracting the baseline value from the frost/ice simulation value. Therefore, the usual case with frost is a drag increase with a positive ΔC_d and a decrease in maximum lift with a negative $\Delta C_{l,max}$. Figures 20 and 21 are for the case with frost/ice simulation from 12

to 60 percent chord. For the drag increments, the worst case was the large ice where ΔC_d is about 9 counts. Very little difference occurred from the typical frost to the large frost/ice case where the drag increment is only slightly larger than the estimated experimental error. The change in maximum lift was somewhat less predictable with the large frost/ice case having the largest lift penalty. The other two cases actually experienced slight increases in $C_{l,max}$. It is important to note that the uncertainty for the incremental loss of the sectional lift coefficient is 0.03.

The effect of frost from 20-60% chord on the sectional aerodynamic coefficient increments is shown in Figs. 22 and 23. Figure 22 shows that both cases resulted in drag decreases but were within the repeatability of the data. Additionally, typical frost resulted in no significant reduction in the maximum sectional lift coefficient. The effect of typical frost and large frost/ice on maximum lift and drag was within the repeatability of the measurements and was therefore considered to be insignificant.

5.3 Slat Open Results

The slat open case was more complex and less easily understood than the slat closed case. This was due to the presence of the laminar separation bubble as discussed earlier. Figure 24 shows the drag polar for the airfoil clean, with trip #2 and with two frost/ice simulations. Here the trip is at 12 percent chord and the frost/ice simulations also start at 12 percent chord. Note that above a lift coefficient of 2.4, the trip #2 data have a lower drag than the clean drag by about 10-12 drag counts. The clean airfoil was experiencing a laminar separation bubble on the main airfoil upper surface which caused a drag increase. At about 8 degrees angle of attack (C_l = 2.4), the stagnation point moved behind the trip causing it to force transition on the upper surface boundary layer and thus eliminating the bubble. The elimination of the bubble caused the reduction in drag.

The large frost/ice case has drag values very similar to the clean case for lift coefficients above 2.4. Here the frost/ice simulation is causing transition which eliminates the bubble and reduces the drag, but the extra roughness above that needed to just trip the flow adds another 10-12 counts of drag. Therefore, by coincidence, the drag values return to the clean case. However, comparing the large frost/ice to the large ice, the large ice has less drag than the large frost/ice. This is not completely understood , but it is hypothesized that this phenomenon may have been caused by the different roughness density of the two ice simulation cases. Specifically, the densities of each simulation were chosen to be representative of the case being modelled. Therefore, the large ice simulation had a lower roughness density, and this may have reduced the drag.

Figure 25 shows the lift coefficient versus angle of attack data for the same cases as in Fig. 24. The large frost/ice simulation caused a small reduction in $C_{l,max}$ while the large ice simulation caused a more significant reduction in maximum lift. As observed in other cases, the effect of frost/ice simulation on the lower surface has almost no effect

on lift curve slope. So while the open slat case and the resulting upper surface laminar bubble resulted in a very complex drag situation, the lift performance was as expected.

From the drag polar and the lift curves, the increments to the sectional lift and drag values were evaluated as stated for the slat closed data. These results are presented in Figs. 26-31. However, the slat open case was complicated by the presence of the laminar separation bubble. Therefore, the choice of a baseline in each case required consideration of the presence of the separation bubble.

If it is desired to model a transport aircraft wing with no laminar separation bubble, then Figs. 26 and 27 summarize the results. For the no bubble case, Fig. 26 shows the effect of frost or ice from 12-60% chord. For these cases, the sectional drag increases are large compared to the slat closed results. Again the large frost results in higher drag than the typical frost. However, the lower drag for large ice than the large frost\ice case is probably a result of the different densities used. For these cases Fig. 27 shows the corresponding reduction in the sectional maximum lift coefficient. As expected, each case reduced the maximum lift, and the loss in maximum lift increased as the size of the frost/ice was increased.

When the frost was located from 20-60% chord, the question of the laminar separation bubble was no longer pertinent. Specifically, the frost was far enough aft that the stagnation point remains well ahead of the frost. Thus, whether or not the separation bubble is present, the sectional increments are the same since only the lower surface boundary layer was affected. The sectional drag increments for these cases, which are shown in Fig. 28, indicate that the frost effects on the drag are small. In fact, the frost/ice simulation actually decreased the drag slightly. The results for the change in sectional lift coefficient are presented in Fig. 29. This figure shows that the typical frost reduced the maximum lift, but the results are within the repeatability of the data. The large frost/ice simulation increased the maximum lift slightly. Note that the large ice simulation was not tested with coverage from 20 to 60 percent chord.

For the case of frost from 12-60% chord with the slat open and assuming a laminar bubble on transport aircraft wings, the results are presented in Figs. 30 and 31. These figures show that the effect of the frost on the drag results in a large reduction of the drag. This occurred due to the drag reduction obtained when the upper surface laminar separation bubble was eliminated by the frost/ice. However, for each case the frost resulted in a reduction of maximum lift with the reduction due to the large ice approximately -0.12.

5.4 Summary

In general, the two-dimensional test data acquired at the LTPT showed small, but noticeable, increases in drag and reductions in maximum lift. For the slat closed case, the change in drag was more noticeable than the reduction of the maximum lift

considering the repeatability of the results. For the slat open case, the presence of a laminar separation bubble complicated the results, and the effect on drag was larger for the no bubble case than for the case with a laminar separation bubble. Further, no increase in drag was observed if the frost was located at 20-60% chord.

The effect on the maximum sectional lift coefficient was similar to the drag results. Specifically, the reductions were larger for the no bubble case when the frost coverage extended from 12-60% chord. Additionally, for the 20-60% chord coverage case the reduction in the maximum lift coefficient was within the repeatability of the results.

6. RESULTS AND DISCUSSION OF THE AIRCRAFT ANALYSIS

The results of the aircraft analysis were obtained following the procedures outlined in section 4 and using the two-dimensional data presented in section 5. Since the effects of frost were in many cases of the same order of magnitude as the uncertainty in the data, it was important to estimate the uncertainty in the 3-D results due to the uncertainty in the 2-D data. By doing this, it was possible to gain an understanding of the threshold above which the 3-D results are significant.

The three-dimensional uncertainty values are presented in Table 10. These were obtained by applying the uncertainties in the airfoil measurements discussed in section 3.4 to the 3-D aircraft performance analysis. Uncertainties in the values for the stall speed, ΔW to maintain the clean stall speed and ΔW to maintain the climb angle are shown. In each case, the percentage change from the clean aircraft value is shown in parentheses. These uncertainties are not small compared to the frost/ice effects and should be considered when interpreting these data.

6.1 2-Jet Transport

The two-dimensional to three-dimensional analysis was performed for the three frost/ice cases: typical frost, large frost/ice, and large ice. The analysis procedures used were presented in chapter 4. The results for the twin-jet are presented in Tables 11-13. These tables present the weight penalties required to restore full performance or full safety margin and the increase in the stall speed due to the frost or ice if the weight was not reduced. These calculations for the 3-D effects are very conservative. The assumption was made that the entire lower surface below the fuel tanks was uniformly covered with frost. Since the fuel tanks are seldom that full upon landing, and the frost growth under the fuel that uniform, this was indeed conservative.

From the typical frost case, Table 11, the maximum weight penalty based on maintaining the climb angle was 226 pounds for the slat open no bubble case. This was significant in terms of the estimated uncertainty, but represented only 0.16 percent of the

twin-jet aircraft weight. The maximum increase in stall speed was only 0.65 knots which was only slightly greater than the uncertainty. Note that this was only transport aircraft are required to know the stall speed within 0.5 knots. This is approximately the same magnitude as the data uncertainty. The largest weight penalty was the 1526 lb weight reduction required to maintain the same stall speed and therefore the same stall margins. However, the uncertainty in this value is 1156 lbs. In summary, the typical frost simulation has barely a measurable effect on the twin-jet performance.

For the large frost/ice case, once again the worst case, based on the drag increase (climb performance), occurred with the slat open, no laminar separation bubble, and coverage from 12-60% chord. This case resulted in a weight penalty of 432 pounds with full frost coverage. The weight penalty based on the maximum lift (stall speed) analysis was a maximum of 1834 lbs for the slat closed case. This case was within 700 pounds of the uncertainty value, and corresponded to an increase in the stall speed of only 0.66%. If only one-half of the lower surface under the wing tanks was covered with ice the effects would be approximately one-half that reported in the table. Using this assumption, which may be more reasonable, the maximum weight penalty drops to 917 lbs which is less than the uncertainty.

Finally, the effect of frost for the absolute worst case of large ice covering the entire fuel tank area is presented in Table 13. Compared to the loss of lift results, the drag increase results are small with all of the weight penalties under 320 pounds. However, for the large ice case the loss of lift with total frost coverage was significant. Both of the cases with increased stall speeds increased the stall speed around 2 percent. Additionally, the weight reductions required to restore the original stall speed are large, but it should be noted that this large ice case may well be unrealistically conservative.

6.2 4-Jet Transport

The results of the three-dimensional analysis performed on the 4-jet transport aircraft are presented in Tables 14-16. Two observations should be made when comparing these data to the data for the 2-jet aircraft case. Specifically, the large gross takeoff weight of the 4-jet aircraft results in larger weight penalties. However, these penalties are lower percentages of the gross takeoff weight in most cases. Additionally, the effects on reduction of the maximum lift are greater for the 4-jet case because it has a lower maximum total lift coefficient and, therefore, the lift reductions are a larger percentage of the clean value.

From Table 14, the worst case weight penalty to maintain climb performance for typical frost resulted in a 975 pound weight penalty. This corresponds to a 0.13% reduction of the gross takeoff weight. The uncertainty in this number is 288 lbs. The results of the loss of maximum lift analysis, as expected, are more severe. Once again since stall speed is only known to within 0.5 knots, only the slat open no bubble case is

significant. Further, this results in a weight penalty of 9223 lbs which is only 2200 pounds over the weight penalty based on the data uncertainty.

The results of the analysis performed for the large frost/ice simulation are presented in Table 15. In general, as was expected the results indicate higher weight penalties for the large frost/ice than the typical frost. As Table 15 shows, the largest weight penalty from the drag analysis (climb performance) occurs for the slat open no bubble case. The weight penalty for this case in 1834 pounds. While this value is large, it still only represents 0.24% of the gross takeoff weight. The results of the maximum lift reduction analysis show that only two of the cases studied resulted in noticeable increases of the stall speed. These are the slat closed and slat open with no bubble with frost coverage from 12-20% chord. In both cases, the increase in the stall speed is under 1%. However, due to the high gross takeoff weight of the 4-jet aircraft, the weight reductions required to restore the original stall speed for the worst case was 11083 lbs.

The effect of the large ice on the takeoff performance is presented in Table 16. Once again, it should be noted that this case is unrealistically conservative. One interesting result observed is the fact that the largest weight penalty from the drag analysis (climb performance) occurred for the slat closed configuration and not the slat open no bubble configuration. The weight penalty for this case is 1359 pounds or 0.18% of the gross takeoff weight. However, the effect of the large ice on the maximum lift is much more significant. For the worst case, the stall speed is increased by 2.08%, and the weight reduction required to restore the stall speed is 4.03% of the gross takeoff weight. These penalties are significant, however, these values results from the absolute worst possible case which is not expected to occur in operation.

The weight of the frost itself has not been considered up to this time. Using the estimated frost weights per unit area given in Table 1, the weight of the frost can be estimated. If the worst case is taken of a uniform growth of ice (simulation 4) over the entire lower surface area under the fuel tanks, the weight for the 2-jet aircraft is 18 pounds and 76 pounds for the 4-jet aircraft. Compared to the weight penalties resulting from the loss in aerodynamic performance these are indeed small and can be neglected.

7. SUMMARY

In this section, the results of this study will be summarized and conclusions and recommendations will also be drawn. Limitations of the study will also be presented so that the results can be understood more clearly and so that any conclusions drawn will be with the clear understanding of the study's limitations.

7.1 Summary and Conclusions

A 2-D test was conducted to evaluate the effect of underwing frost on a typical transport airfoil section in a takeoff configuration. The test was run in the NASA Langley Low-Turbulence Pressure Tunnel to obtain a Reynolds number (5 to 16 million) more characteristic of takeoff. The frost or ice was simulated using geometrically scaled roughness elements applied to the wing lower surface. Three frost/ice simulations were tested applied from 12 to 60 percent chord, and 2 of these were also tested from 20 to 60 percent chord. Baseline data were acquired clean and with the boundary layer tripped.

The most significant effects were found with the slat open. In this configuration a laminar separation bubble occurred on the airfoil's upper surface, leading edge. A frost simulation or a boundary-layer trip at 12 percent chord on the lower surface affected this bubble at angles of attack greater than 8 deg. as the stagnation point moved behind this point. This caused the roughness to effectively be on the airfoil's aerodynamic upper surface. The largest penalties were seen when the frost was at 12 percent chord and a baseline simulating an airfoil with no bubble was used.

These 2-D data were converted to approximate 3-D increments in aircraft maximum lift and parasite drag. Using the drag increments due to frost/ice, weight penalties were calculated to maintain the engine-out, first and second segment climb performance. Weight penalties were also calculated from the frost/ice increment in maximum lift data to maintain the clean aircraft stall speed. The stall speed for the aircraft with frost/ice and at the clean gross weight were also presented. Results for a typical 2-jet and large 4-jet aircraft are presented. The 3-D analysis based on the 2-D wind tunnel results found that:

1) The effect of underwing frost on takeoff ground roll was insignificant.

2) Weight penalties to maintain climb as a percent of gross weight are larger for a 2-jet aircraft as compared to a 4-jet aircraft.

3) The largest weight penalty to maintain climb angle was 0.31%, or 432 lbs, for the 2-jet aircraft.

4) Stall speed increased less than 0.72 percent for frost and less than 2.1 percent for ice.

5) The largest weight penalties were those to maintain stall speed at the clean value. Here the percentage penalties were the highest for the 4-jet with frost at a maximum of 1.43% and ice at 4.03%. (Operations with underwing ice are not allowed.) However, the experimental uncertainty was largest here at 0.91%.

It is important to note when interpreting these results that several conservative assumptions were made in the 2-D test and 3-D analysis. Some of these assumptions are:

1) The frost covers the wing surface under the tanks uniformly in the chordwise direction. (assumption in the 2-D test)

2) The large frost size of 0.059 inches and the large ice size of 0.125 inches are conservatively large.

3) The frost covers the entire area under the fuel tanks in a spanwise direction. (assumption in the 3-D calculations)

4) The assumed density in terms of roughness elements per unit area for the large ice simulation #4 is extremely conservative.

All of these assumptions result in larger aircraft weight penalties. For example, operational experience indicates that frost does not accrete on the entire area under the fuel tanks. Due to wing dihedral, the fuel remaining in the tanks when the aircraft lands is in the inboard part of the tanks, not distributed uniformly throughout the tank. A more realistic worst case estimate of the frost/ice coverage spanwise might be one-half of the tank area. This would result in approximately one-half the weight and stall speed penalties reported above and in Tables 11-16. If the frost and frost/ice penalties are reduced by 1/2, and the large frost case is ignored as being unrealistically conservative, the effect of underwing frost on transport aircraft takeoff is indeed very small. The only weight penalty which might be considered significant is that to maintain a constant V_{stall}. However, if this is viewed from the change in stall speed view point, the corresponding change in stall speed due to 1/2 coverage of frost is less than the 0.5 knot flight measurement accuracy in all but one case.

7.2 Limitations of the Study

A careful evaluation of this study identifies areas in which limitations arise. This does not invalidate the study, but merely provides a better foundation for evaluation of the conclusions or in planning future research. These limitations are:

1) The roughness height and density for ice on the undersurface of the wing is not known accurately.

2) Only one airfoil, slat and flap combination was tested.

3) It is possible that moving the frost further forward on the airfoil lower surface would increase the adverse effect of frost. Only 2 locations, $x/c=0.12$ and 0.20, were tested.

4) Trends in the data indicate that the aerodynamic effects of frost are less at higher Reynolds number. Most of the data were taken at 9 million.

5) In the most critical slat open and no bubble case the lower-surface boundary layer was not tripped at high angle of attack.

6) There is currently no data available to estimate how accurately the extrapolation of the 2-D data to the 3-D aircraft has been done.

7.3 Recommendations

The recommendations made here are with respect to the accuracy and completeness of the study. Three recommendations are made which would expand the applicability and accuracy of the 2-D and 3-D results. These recommendations are:

1) Conduct 2-D experiments to carefully examine the effect of airfoil configuration, forward frost location and Reynolds number on aerodynamic performance.

2) Conduct experiments to validate the extrapolation of 2-D frost/ice data to a 3-D wing.

3) Since only one airfoil and 2 representative aircraft were used in the aircraft performance calculations, the effect of frost/ice on each aircraft type of interest should be carefully examined.

8. REFERENCES

1. Ljungstroem, B. L. G., Wind Tunnel Investigation of Simulated Hoar Frost on a 2 Dimensional Wing Section With and Without High Lift Devices", FFA-Au-902, April 1972.

2. Bragg. M. B. and Gregorek, G. M., "Environmentally Induced Surface Roughness Effects on Laminar Flow Airfoils: Implications for Flight Safety", AIAA Paper 89-2049, 1989.

3. Brumby, R. E., "Wing Surface Roughness - Cause and Effect", *D. C. Flight Approach*, No. 32, Jan. 1979.

4. Lynch. F. T., Valarezo, W. O., and McGhee, R. J., "The Adverse Aerodynamic Impact of Very Small Leading-Edge Ice (Roughness) Buildups on Wings and Tails", AGARD Fluid Dynamics Specialists Meeting on *Effects of Adverse Weather on Aerodynamics,* Toulouse France, 29 April - 1 May, 1991.

5. Bragg, M. B. and Gregorek, G. M., "Performance Analyses for Aircraft Icing Conditions", AIAA Paper 84-0180, 1984.

6. Kind, R. J. and Lawrysyn, M. A., " Effects of Frost on Wing Aerodynamics and Take-Off Performance", AGARD Fluid Dynamics Specialists Meeting on *Effects of Adverse Weather on Aerodynamics*, Toulouse France, 29 April - 1 May, 1991.

7. Dietenberger, M., "A Proposed Simple and Sake Aircraft Take-Off or Landing Procedure with Wing Roughness or Protuberances", AIAA Paper 83-0604, 1983.

8. van Hengst, J. and Boer, J. N., "The Effect of Hoar-Frosted Wings on the Fokker 50 Take-Off Characteristics", AGARD Fluid Dynamics Specialists Meeting on *Effects of Adverse Weather on Aerodynamics*, Toulouse France, 29 April - 1 May, 1991.

9. Thompson, J. K., "Frost on Parked Aircraft", WADC Technical Note 57-197, 1957.

10. Langston, P. A. S., "Hoar Frost on Aircraft Surfaces", BEA Engineering, Technical Note No. P/570, 1968.

11. Kind, R. J. and Lawrysyn, M. A., "Aerodynamic Characteristics of Hoar Frost Roughness", presented at AIAA 29th Aerospace Sciences Meeting, Reno, NV, Jan. 1991 AIAA paper 91-0686.

12. Brumby, Ralph., private communication, February, 1992.

13. Zierten, Thomas, private communication, February, 1992.

14. Braslow, Albert, L. and Knox, Eugene, C., "Simplified Method for Determination of Critical Height of Distributed Roughness Particles for Boundary-Layer Transition at Mach Numbers From 0 to 5", NACA TN 4363, September, 1958.

15. Rae, William H. and Pope, Allan, *Low-Speed Wind Tunnel Testing, John Wiley and Sons, New York, 1984.*

16. McCormick, Barnes W., *Aerodynamics, Aeronautics and Flight Mechanics*, John Wiley and Sons, New York, 1979.

17. Lan, C. E. and Roskam,J., *Airplane Aerodynamics and Performance*, Roskam Aviation and Engineering Corporation, Ottawa, Kansas, 1980.

18. Raymer, Daniel P., *Aircraft Design a Conceptual Approach*, AIAA Education Series, American Institute of Aeronautics and Astronautics, Washington DC, 1989.

19. Mack, M. D. and McMasters, J. H., "High Reynolds Number Testing in Support of Transport Airplane Development", AIAA Paper No. 92-3982, July, 1992.

(page intentionally left blank)

Table 1. Aircraft frost/ice roughness simulation

FULL SCALE

Simulation	Ice/Frost Simulated	k in. (mm)	Concentration per sq. in.	k/c*	Weight gm/ft^2
1	Typical frost	0.016 (0.4)	30	0.00011	3
2	Large frost/ ice	0.059 (1.5)	12	0.00040	6
3	not used	---	---	---	---
4	Large Ice	0.125 (3.7)	10	0.00085	10

*** assumes c = 12.21 ft.**

Table 2. Desired model roughness simulation values

Simulation	Ice/Frost Simulated	Roughness extent x/c	k in.	Concentration per sq. in.
1	Typical frost	0.12-0.60	0.0024	1330
1	Typical frost	0.20-0.60	0.0024	1330
2	Large frost/ice	0.12-0.60	0.0089	532
2	Large frost/ice	0.20-0.60	0.0089	532
3	not used	---	---	---
4	Large Ice	0.12-0.60	0.0190	377

Table 3. Actual simulation with measured densities

Simulation	Ice/Frost Simulated	Roughness extent x/c	k in.	Concentration per sq. in.
1	Typical frost	0.12-0.60	0.0029-0.0035	852
1	Typical frost	0.20-0.60	0.0029-0.0035	852
2	Large frost/ice	0.12-0.60	0.0083-0.0098	480
2	Large frost/ice	0.20-0.60	0.0083-0.0098	480
3	not used	---	---	---
4	Large Ice	0.12-0.60	0.0165-0.0197	135

Table 4. Model lower surface boundary-layer transition strips, "trips"

Trip #	x/c	k	Density
1*	---	0.003	---
2	0.12	0.006	1445
3	0.20	0.009	867
4	0.20	0.006	363

*** Trip #1 was never used**

Table 5. Underwing frost test run number matrix

Re	Slat Position	Clean	Trip 2	Trip 3	Trip 4	Sim 1	Sim 1A	Sim 2	Sim 2A	Sim 4
5	closed	20	4	---	---	---	---	10	---	---
5	open	---	--	---	---	---	---	---	---	---
9	closed	19	5	23	32	28	29	11	14	34
9	open	16	8	24	31	25	30	9	15	35
12	closed	33(18)	6	22	---	27	---	12	---	---
12	open	---	--	---	---	---	---	---	---	---
16	closed	17	7	21	---	26	---	13	---	---
16	open	---	--	---	---	---	---	---	---	---

*** All runs: slat @ 20°, flap @ 15° frost @ x to 60% chord**

Table 6. 2-jet aircraft data

GTOW (lbs.):	140,000	**VS1g (kts):**	119
S (ft^2):	1270	**V1 (kts):**	139
b (ft.):	110.4	**VR (kts):**	142
bflap/b:	0.67	**VLOF (kts):**	147
AR:	9.6	**V2 (kts):**	148
ΛC/4 (°):	24.5	**CLmax:**	2.3
Thrust (lbs.):	41,310	**Tank spanwise location (2y/b):**	0.09-0.64

Table 7. 4-jet aircraft data

GTOW (lbs.):	775,000	**VS1g (kts):**	152
S (ft^2):	5500	**V1 (kts):**	147
b (ft.):	196	**VR (kts):**	150
bflap/b:	0.70	**VLOF (kts):**	168
AR:	7.0	**V2 (kts):**	172
ΛC/4 (°):	37.5	**CLmax:**	1.8
Thrust (lbs.):	192,648	**Tank spanwise location (2y/b):**	0.11-0.71

Table 8. Minimum required climb gradients

	Minimum climb gradient for Aircraft with n engines, %(deg.)		
Takeoff climb	n=2	n=3	n=4
First segment	0 (0)	0.3 (0.17)	0.5 (0.29)
Second Segment	2.4 (1.37)	2.7 (1.55)	3.0 (1.72)

Table 9. Baseline cases for the frost/slat cases modelled

Slat	Frost/ice location	Laminar bubble	Baseline
Closed	0.12-0.60	No	Trip #2 (x/c=0.12)
Closed	0.20-0.60	No	Trip #4 (x/c=0.20)
Open	0.12-0.60	No	Trip #2 (x/c=0.12)
Open	0.20-0.60	No	Trip #4 (x/c=0.20)
Open	0.12-0.60	Yes	Trip #4 (x/c=0.20)
Open	0.20-0.60	Yes	Trip #4 (x/c=0.20)

Table 10. 3-D data uncertainty from 2-D data uncertainty

	2-Jet Aircraft	4-Jet Aircraft
ΔV_S (kts.):	± 0.45 (0.38%)	± 0.63 (0.42%)
ΔW (lbs.): from C_{Lmax}	± 1162 (0.83%)	± 7053 (0.91%)
ΔW (lbs.): from C_{D0}	± 68 (0.05%)	± 288 (0.04%)

Table 11. Effect of typical frost (simulation 1 and 1a) on the 2-jet aircraft

Aircraft Configuration	Tank Location x/c	Weight Penalties (lbs.)			Increase in Stall Speed (kts.)
		Segment 1	Segment 2	C_{Lmax} Loss	
Slat Closed	0.12	115 (0.08%)	114 (0.08%)	0	0
Slat Closed	0.20	0	0	0	0
Slat Open No Bubble	0.12	226 (0.16%)	220 (0.16%)	1526 (1.09%)	0.65 (0.55%)
Slat Open Bubble	0.12	0	0	560 (0.40%)	0.24 (0.20%)
Slat Open	0.20	0	0	700 (0.50)	0.30 (0.25%)

Table 12. Effect of large frost/ice (simulations 2 and 2a) on the 2-jet aircraft

Aircraft Configuration	Tank Location x/c	Weight Penalties (lbs.)			Increase in Stall Speed (kts.)
		Segment 1	Segment 2	C_{Lmax} Loss	
Slat Closed	0.12	115 (0.08%)	114 (0.08%)	1834 (1.31%)	0.79 (0.66%)
Slat Closed	0.20	0	0	420 (0.30%)	0.18 (0.15%)
Slat Open No Bubble	0.12	432 (0.31%)	416 (0.30%)	1554 (1.11%)	0.67 (0.56%)
Slat Open Bubble	0.12	0	0	602 (0.43%)	0.26 (0.22%)
Slat Open	0.20	0	0	0	0

Table 13. Effect of large ice (simulation 4) on the 2-jet aircraft

Aircraft Configuration	Tank Location x/c	Weight Penalties (lbs.) Segment 1	Segment 2	C_{Lmax} Loss	Increase in Stall Speed (kts.)
Slat Closed	0.12	320 (0.23%)	310 (0.22%)	0	0
Slat Open No Bubble	0.12	194 (0.14%)	190 (0.14%)	5166 (3.69%)	2.26 (1.90%)
Slat Open Bubble	0.12	0	0	4200 (3.00%)	1.83 (1.54%)

Table 14. Effect of typical frost (simulations 1 and 1a) on the 4-jet aircraft

Aircraft Configuration	Tank Location x/c	Weight Penalties (lbs.) Segment 1	Segment 2	C_{Lmax} Loss	Increase in Stall Speed (kts.)
Slat Closed	0.12	458 (0.06%)	479 (0.06%)	0	0
Slat Closed	0.20	0	0	0	0
Slat Open No Bubble	0.12	938 (0.12%)	975 (0.13%)	9223 (1.19%)	0.91 (0.60%)
Slat Open Bubble	0.12	0	0	3410 (0.44%)	0.34 (0.22%)
Slat Open	0.20	0	0	4263 (0.55%)	0.42 (0.28%)

Table 15. Effect of large frost/ice (simulations 2 and 2a) on the 4-jet aircraft

Aircraft Configuration	Tank Location x/c	Weight Penalties (lbs.) Segment 1	Segment 2	C_{Lmax} Loss	Increase in Stall Speed (kts.)
Slat Closed	0.12	480 (0.06%)	501 (0.06%)	11083 (1.43%)	1.10 (0.72%)
Slat Closed	0.20	0	0	3255 (0.42%)	0.32 (0.21%)
Slat Open No Bubble	0.12	1768 (0.23%)	1834 (0.24%)	9455 (1.22%)	0.93 (0.61%)
Slat Open Bubble	0.12	0	0	3643 (0.47%)	0.36 (0.24%)
Slat Open	0.20	0	0	0	0

Table 16. Effect of large ice (simulation 4) on the 4-jet aircraft

Aircraft Configuration	Tank Location x/c	Weight Penalties (lbs.) Segment 1	Segment 2	C_{Lmax} Loss	Increase in Stall Speed (kts.)
Slat Closed	0.12	1309 (0.17%)	1359 (0.18%)	0	0
Slat Open No Bubble	0.12	785 (0.10%)	817 (0.11%)	31233 (4.03%)	3.16 (2.08%)
Slat Open Bubble	0.12	0	0	25420 (3.28%)	2.56 (1.68%)

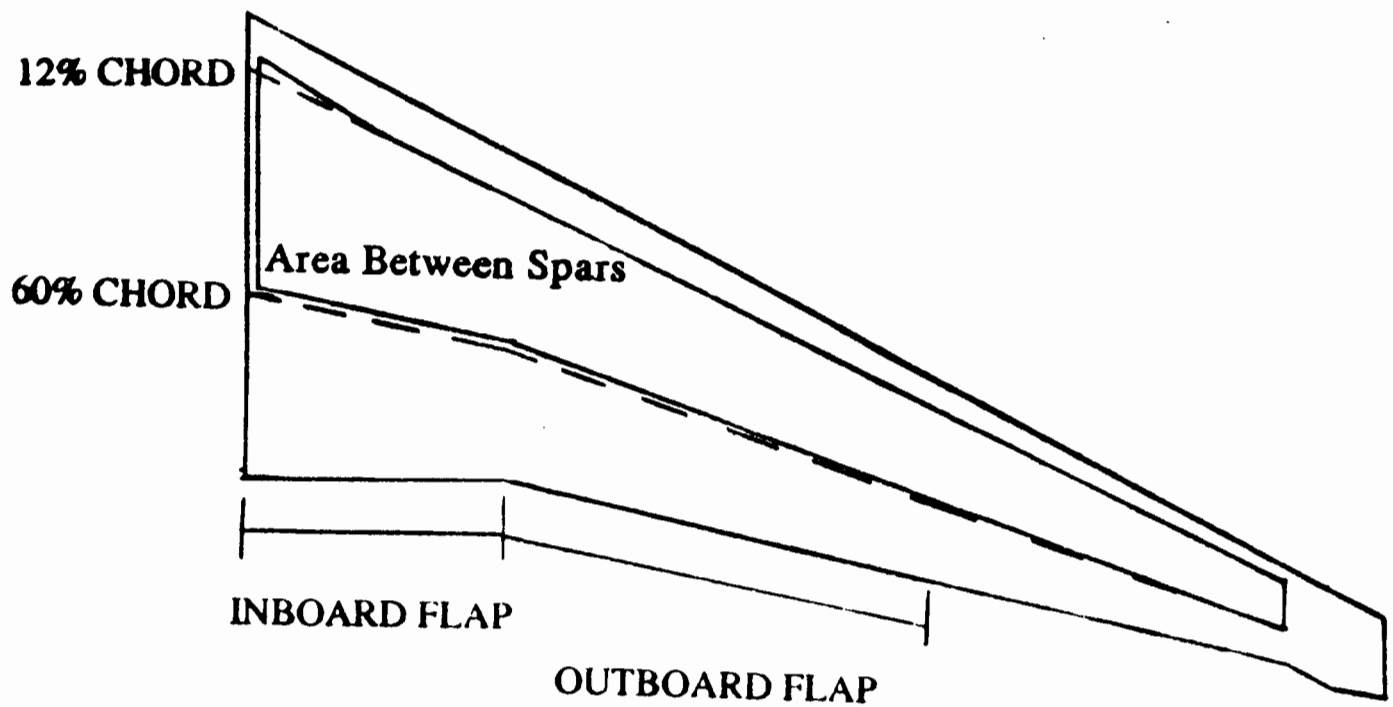

Figure 1. MD-80 wing planform

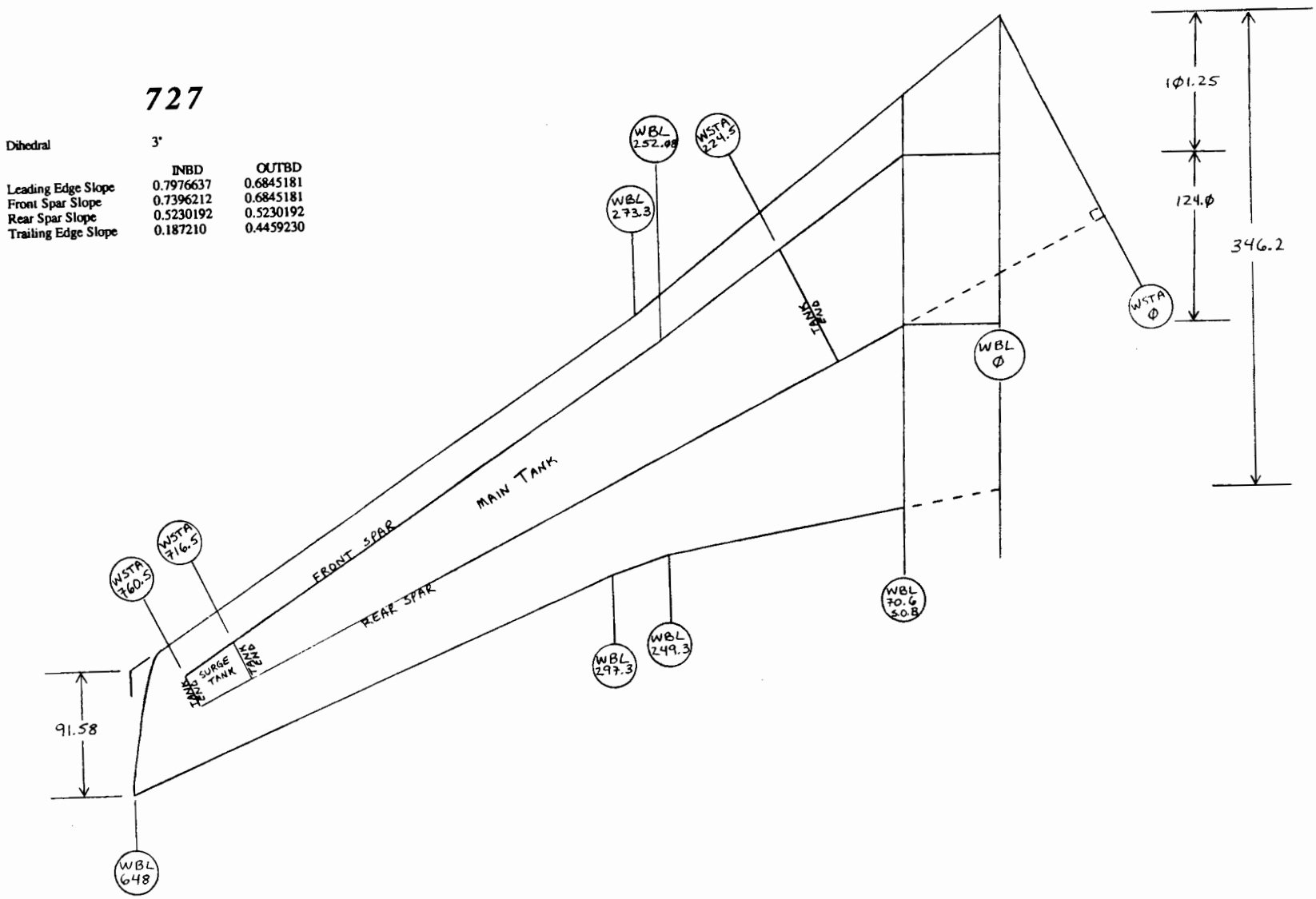

Figure 2a. B727 wing planform

737

Area	1,023.37 ft^2	
Span	1,086.02 in	
AR	8.0035	
Dihedral	6°	
	INBD	OUTBD
Leading Edge Slope	0.7254559	0.5223086
Front Spar Slope	0.8079792	0.5223086
Rear Spar Slope	0.2731394	0.3704739
Trailing Edge Slope	0	0.2983048
Flaps 1 ΔC_{w_f}	9.6 in	5.3 in
Flaps 5 ΔC_{w_f}	22.4 in	15.2 in
Flaps 15 ΔC_{w_f}	29.9 in	23.0 in
Flaps 1 δ_{feff}	1.5°	1.0°
Flaps 5 δ_{feff}	8.5°	6.9°
Flaps 15 δ_{feff}	19.7°	17.6°
Flaps 1 and 5 δ_{slat}	17° - Sealed	
Flaps 15 δ_{slat}	28° - Gapped	

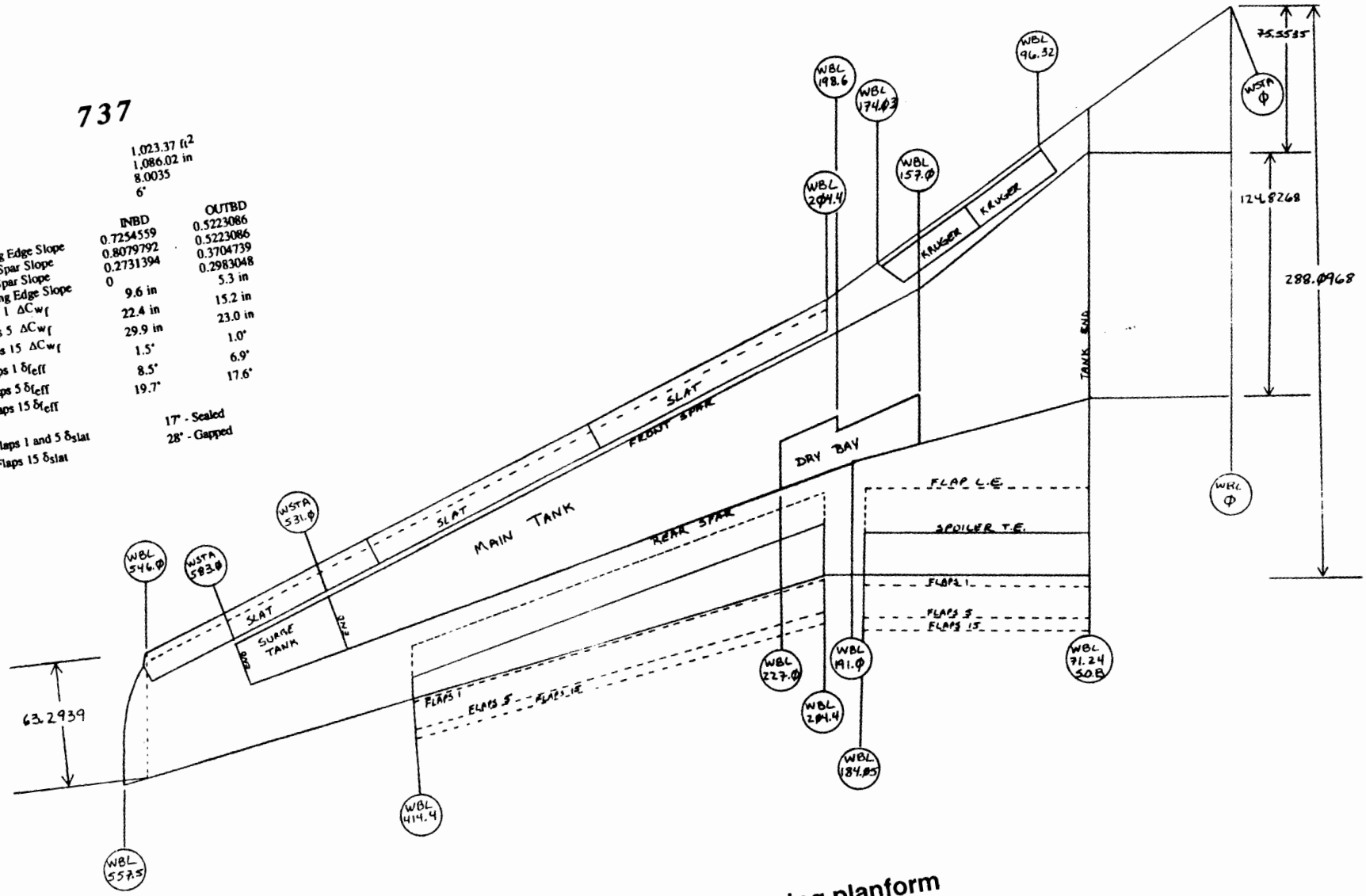

Figure 2b. B737 wing planform

747

Area	5,632.88 ft^2
Span	2,330.50 in
AR	6.6958
Dihedral	7°

	INBD	OUTBD
Leading Edge Slope	0.9098890	0.8290133
Front Spar Slope	0.8435035	0.8290133
Rear Spar Slope	0.6639348	0.6639348
Trailing Edge Slope	0.3203257	0.5822674
Flaps 10 ΔC_{w_f}	57.9 in	39.3 in
Flaps 20 ΔC_{w_f}	64.3 in	43.0 in
Flaps 10 $\delta_{f_{eff_{ave}}}$	23.27°	18.5°
Flaps 20 $\delta_{f_{eff_{ave}}}$	37.31°	28.5°

$\delta_{k_{ave}}$	66.55°
$\delta_{v_{ave}}$ - Mid Section	66.55°
$\delta_{v_{ave}}$ - Outbd Sectn	59.05°

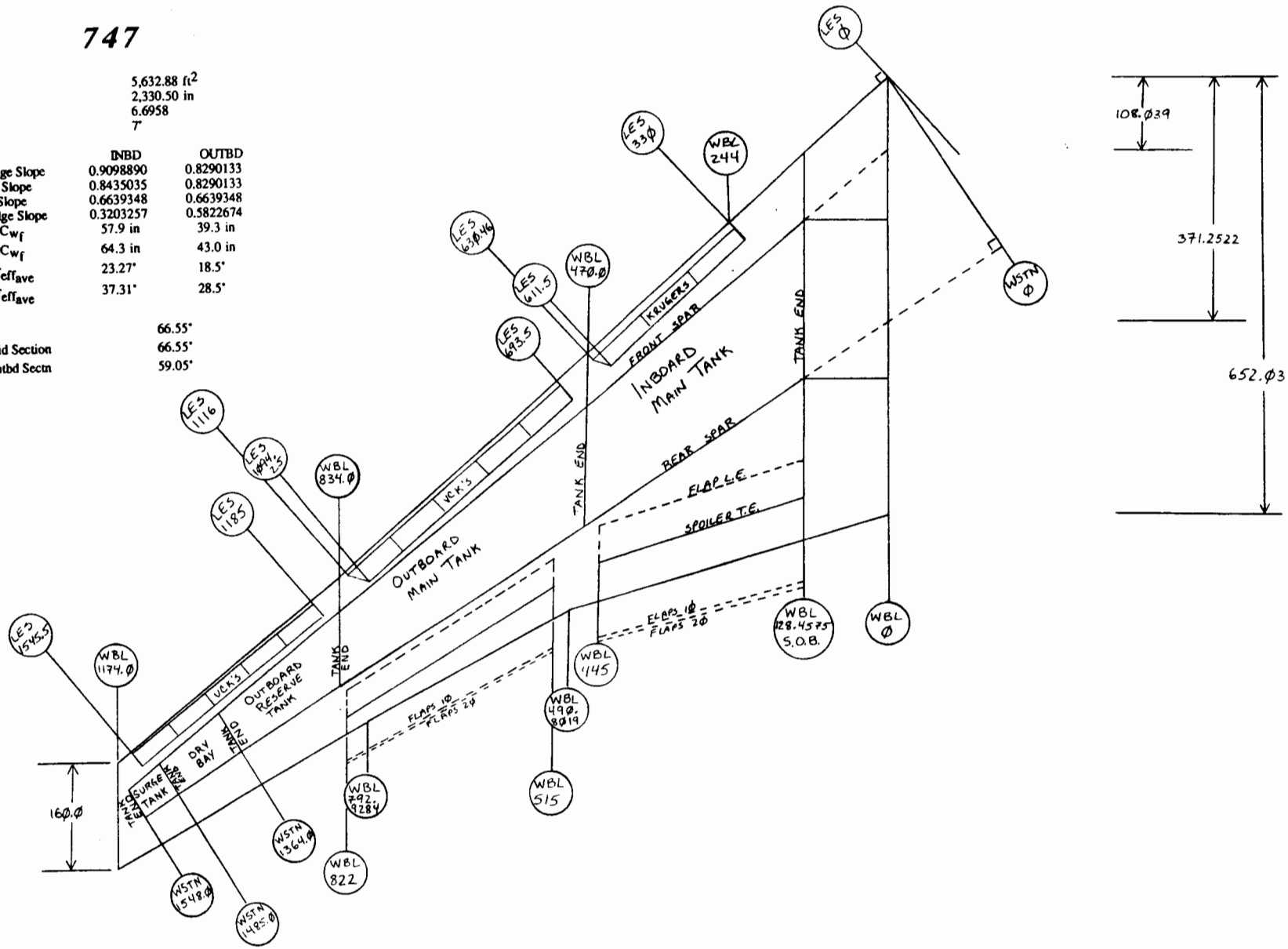

Figure 2c. B747 wing planform

757

Dihedral	5°	
	INBD	OUTBD
Leading Edge Slope	0.5391416	0.5391416
Front Spar Slope	0.5324119	0.5324119
Rear Spar Slope	0.4198578	0.3128151
Trailing Edge Slope	0	0.2478083

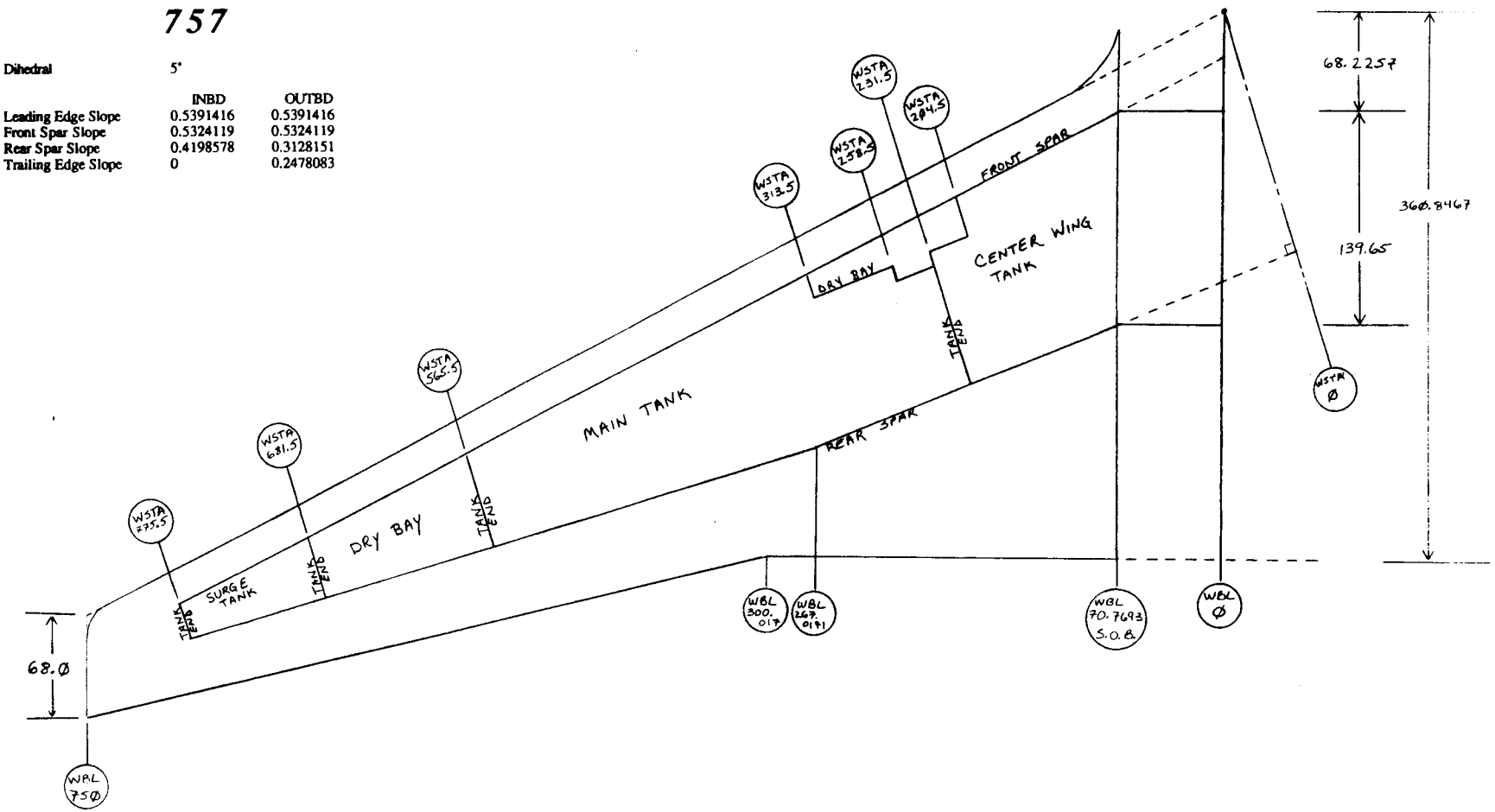

Figure 2d. B757 wing planform

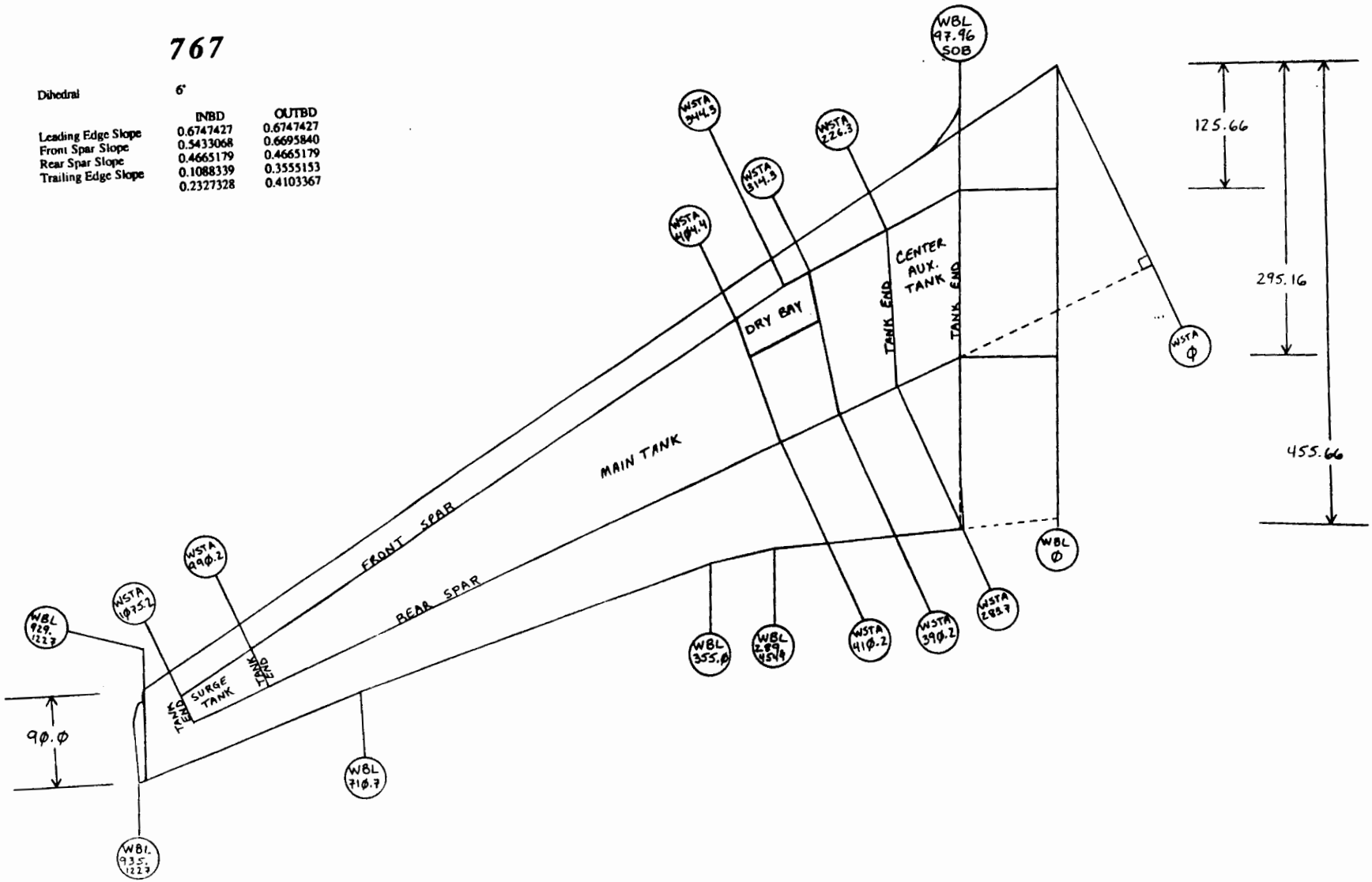

Figure 2e. B767 wing planform

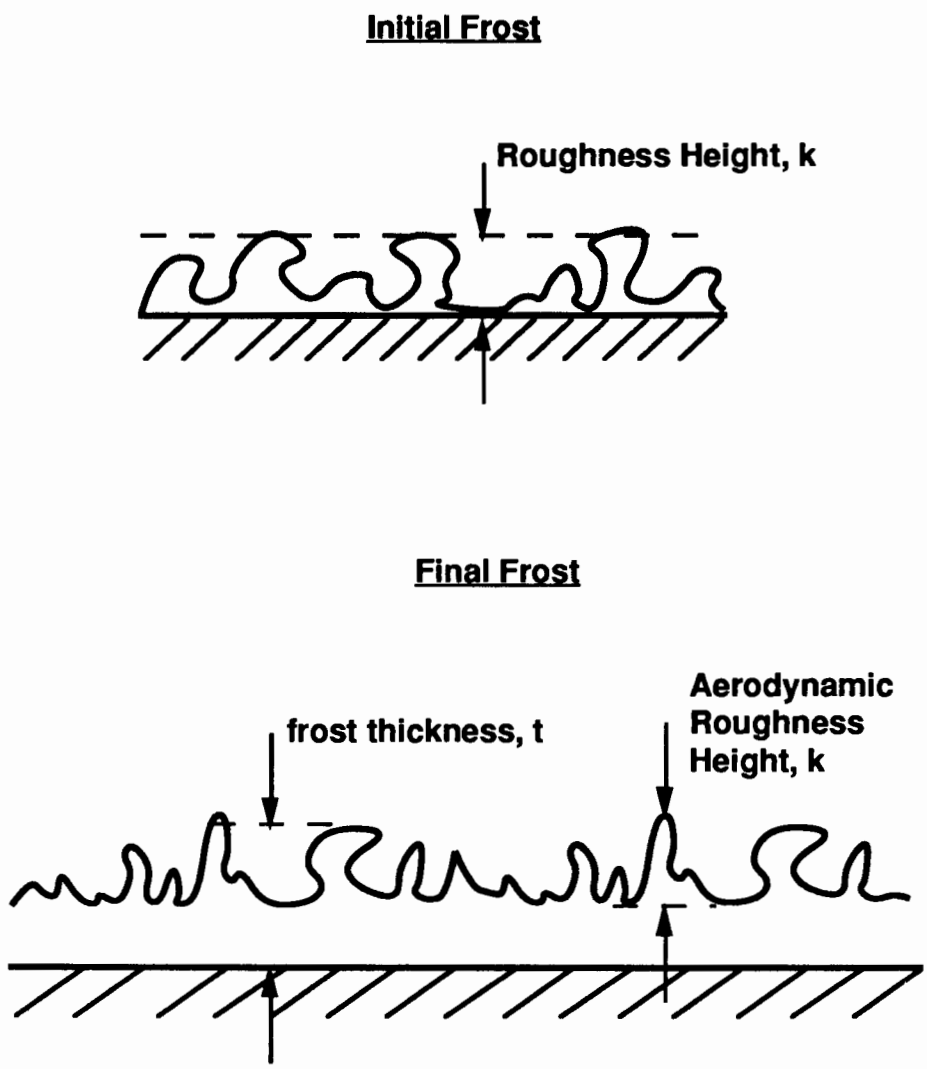

Figure 3. Frost accretion

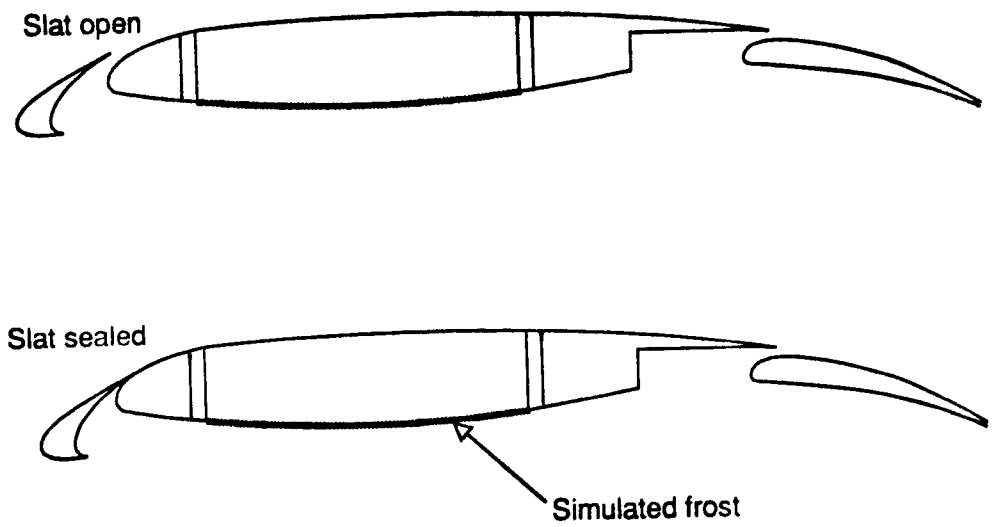

Figure 4. Airfoil model in takeoff configuration

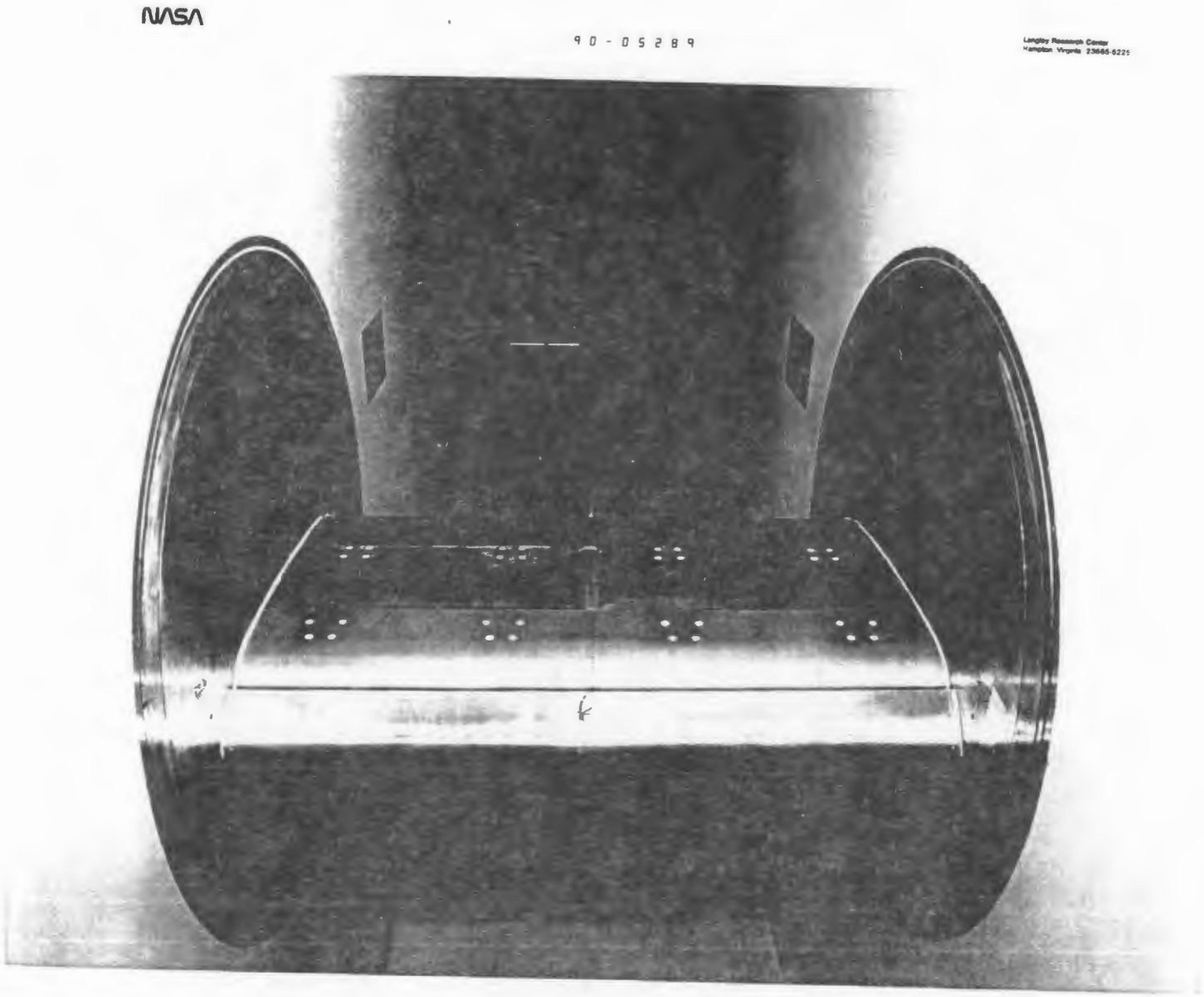

Figure 5. High-lift transport airfoil installed in the low-turbulence pressure tunnel.

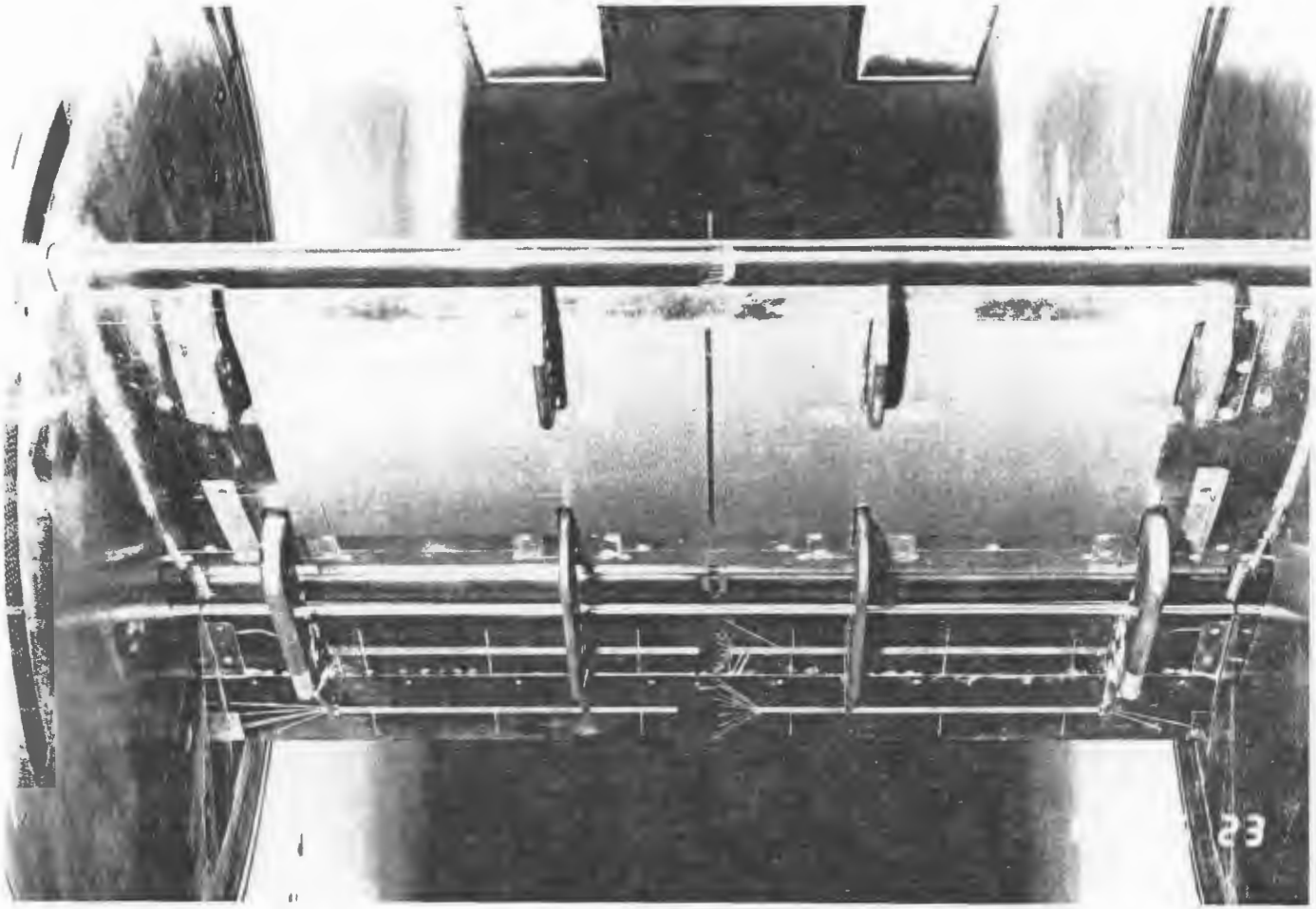

Figure 6. Underwing frost simulation installed on the airfoil lower surface from 12-60% chord.

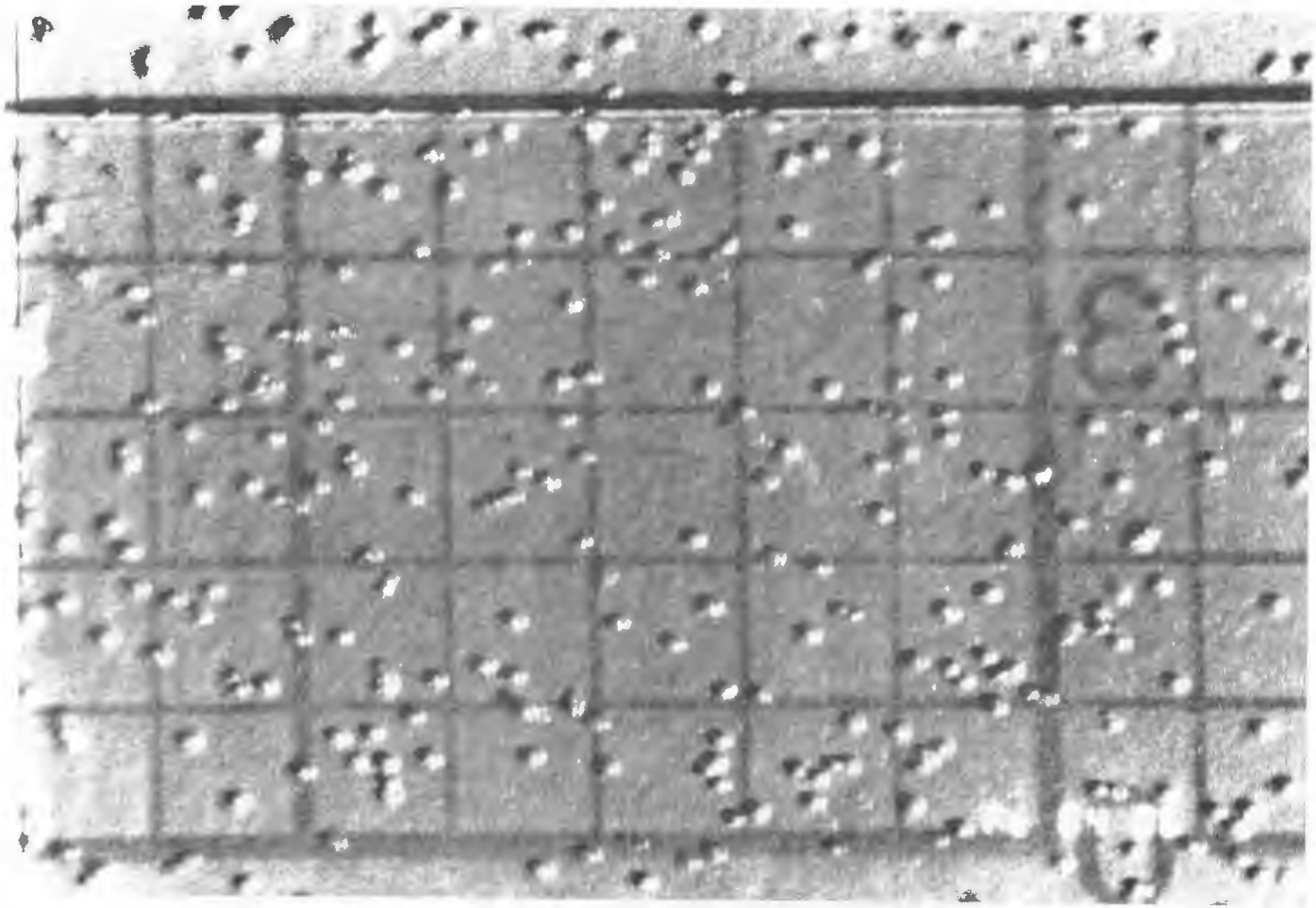

Figure 7. Close-up of the frost simulation with 1/100th in^2 overlay.

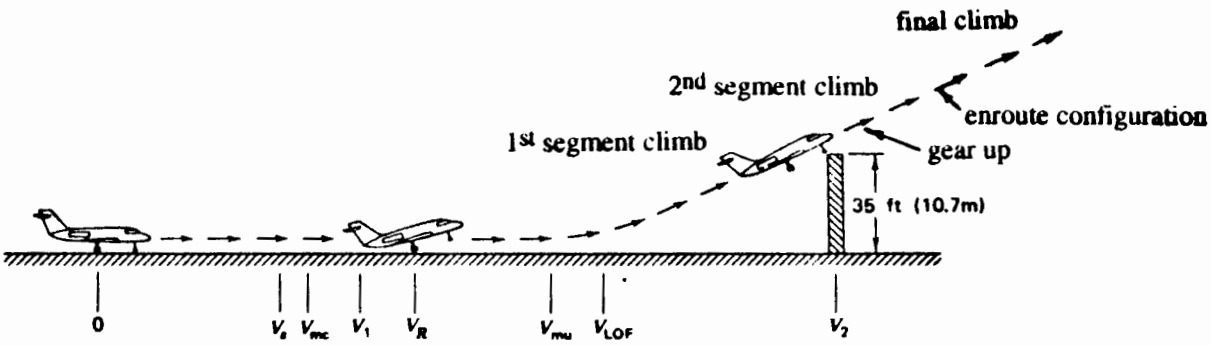

Ref. McCormick

- **Key Airspeeds**
  V1: Critical engine failure speed
  VR: Rotation speed
  VLOF: Lift-off speed
  V2: Takeoff climb speed

Figure 8. Transport aircraft takeoff

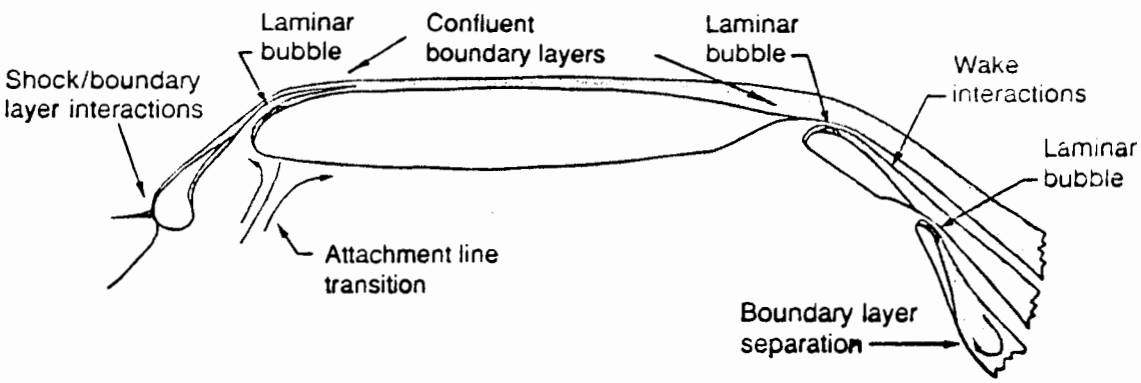

Ref. Mack and McMasters, AIAA 92-3982

Figure 9. Flow on 2-D high-lift airfoils

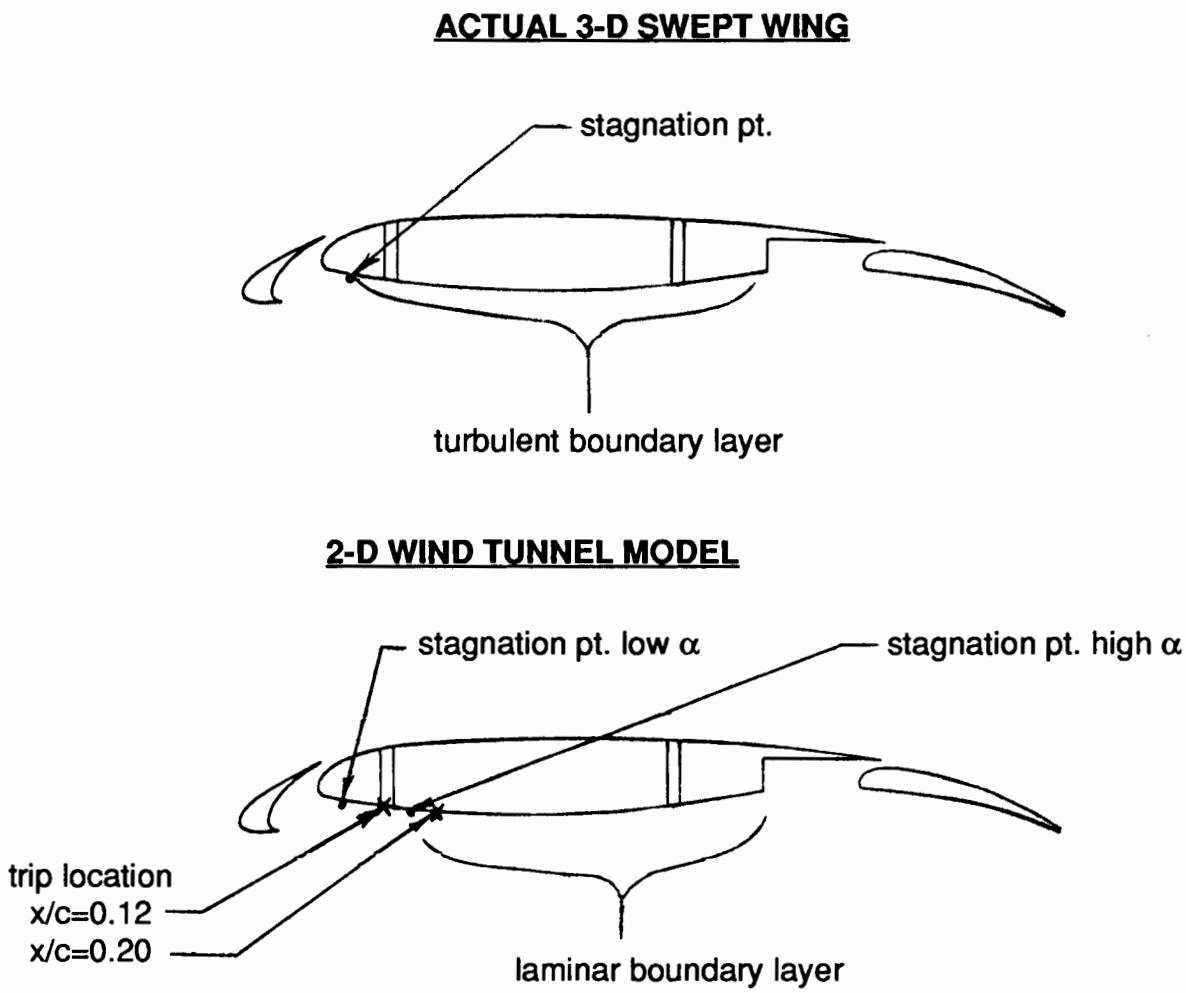

Figure 10. Boundary layer transition modelling

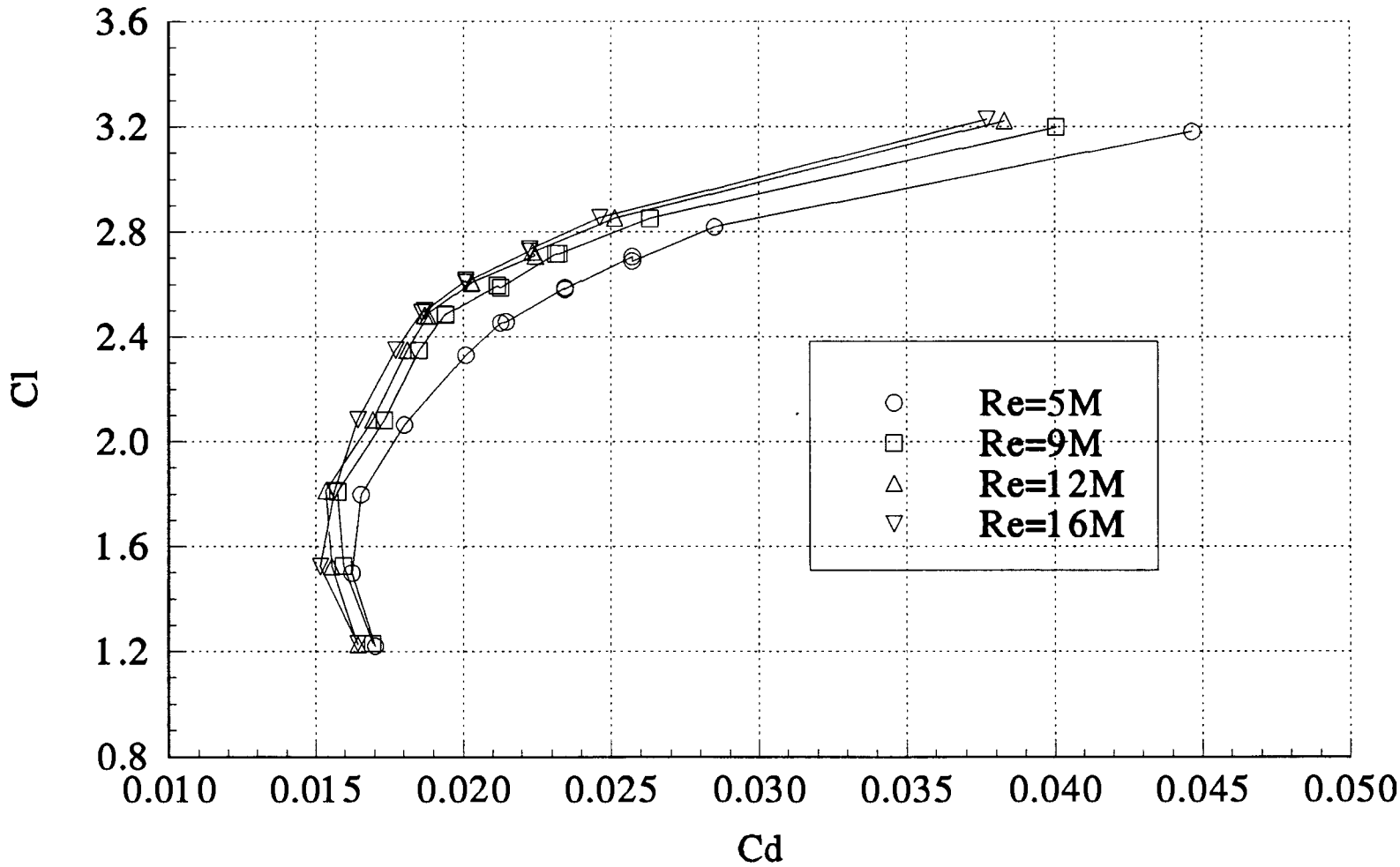

Figure 11. Reynolds number comparison of drag polars for the slat closed clean airfoil

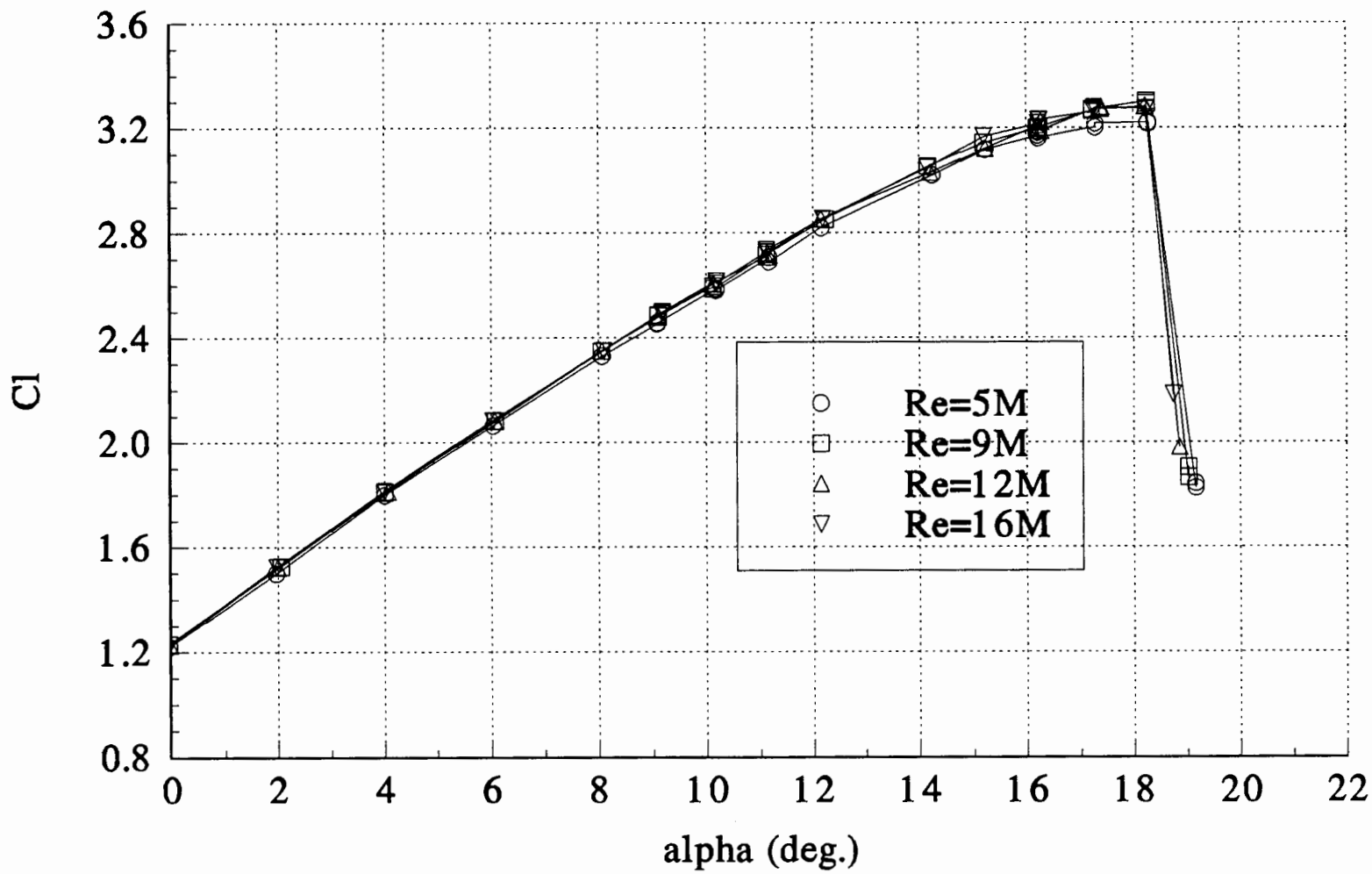

Figure 12. Reynolds number comparison of lift curves for the slat closed clean airfoil

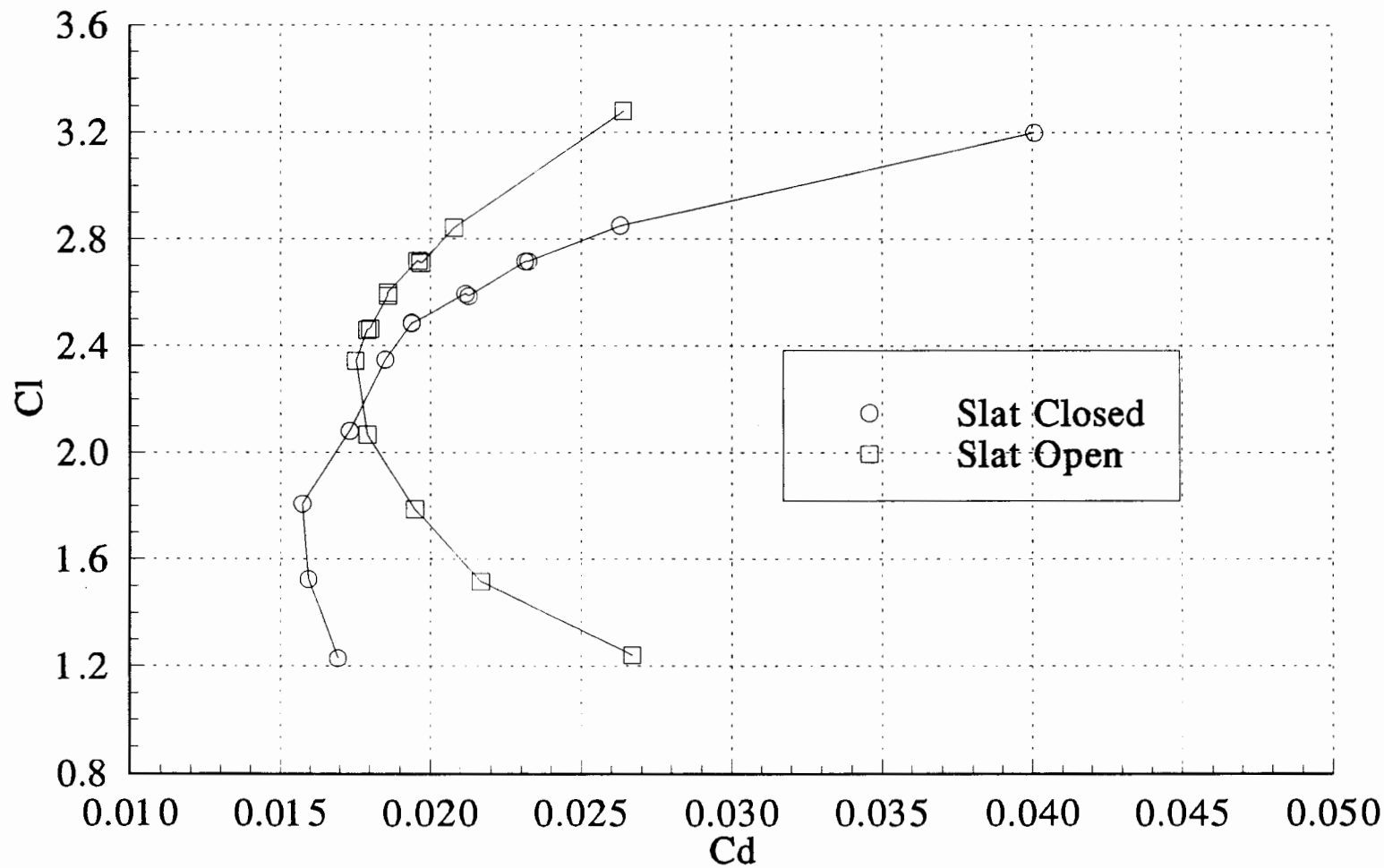

Figure 13. Slat position comparison of drag polars for the clean airfoil at Re=9M

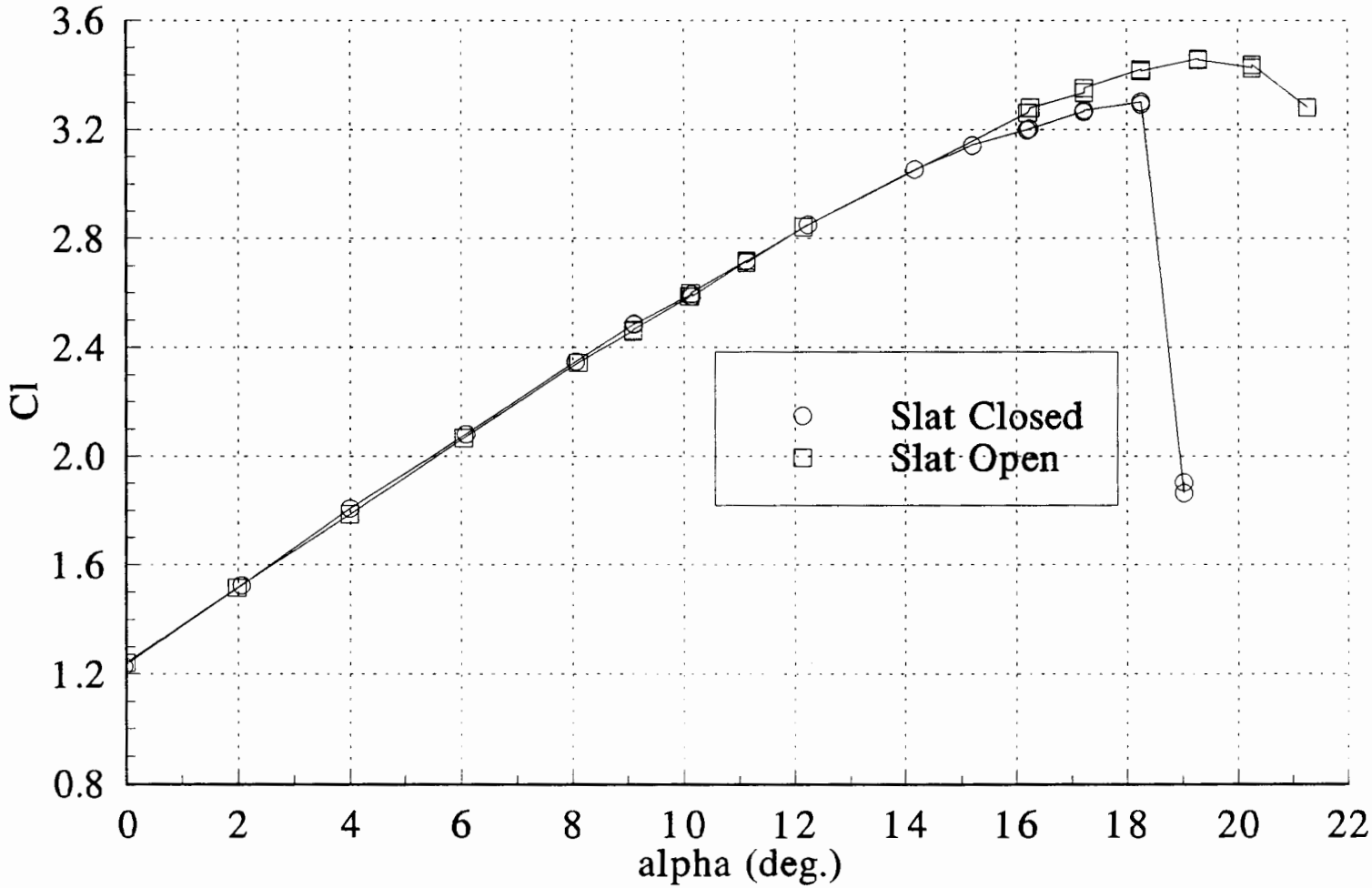

Figure 14. Slat position comparison of lift curves for the clean airfoil at Re= 9M

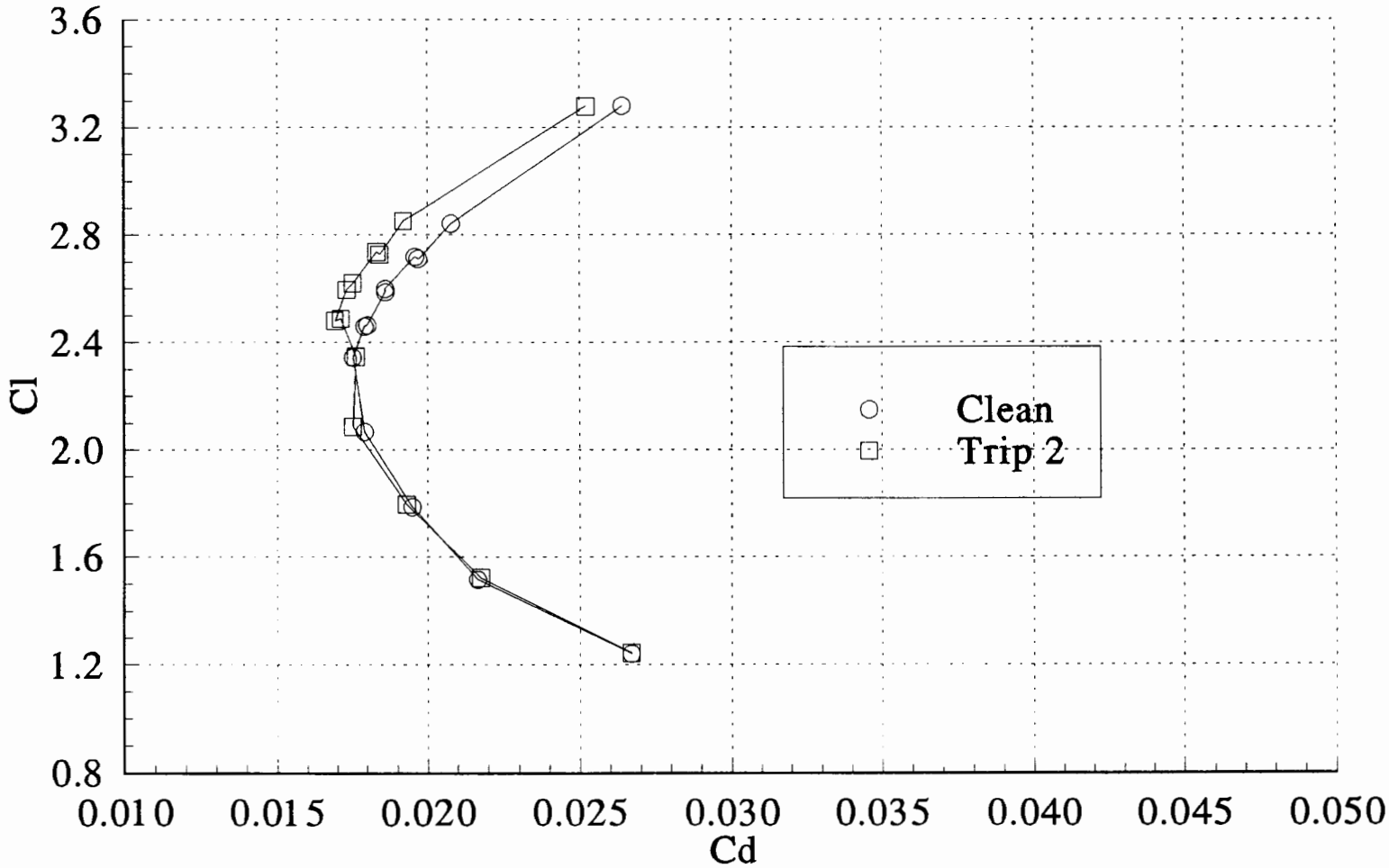

Figure 15. Slat open comparison of drag polars for the clean airfoil versus Trip 2 at Re=9M

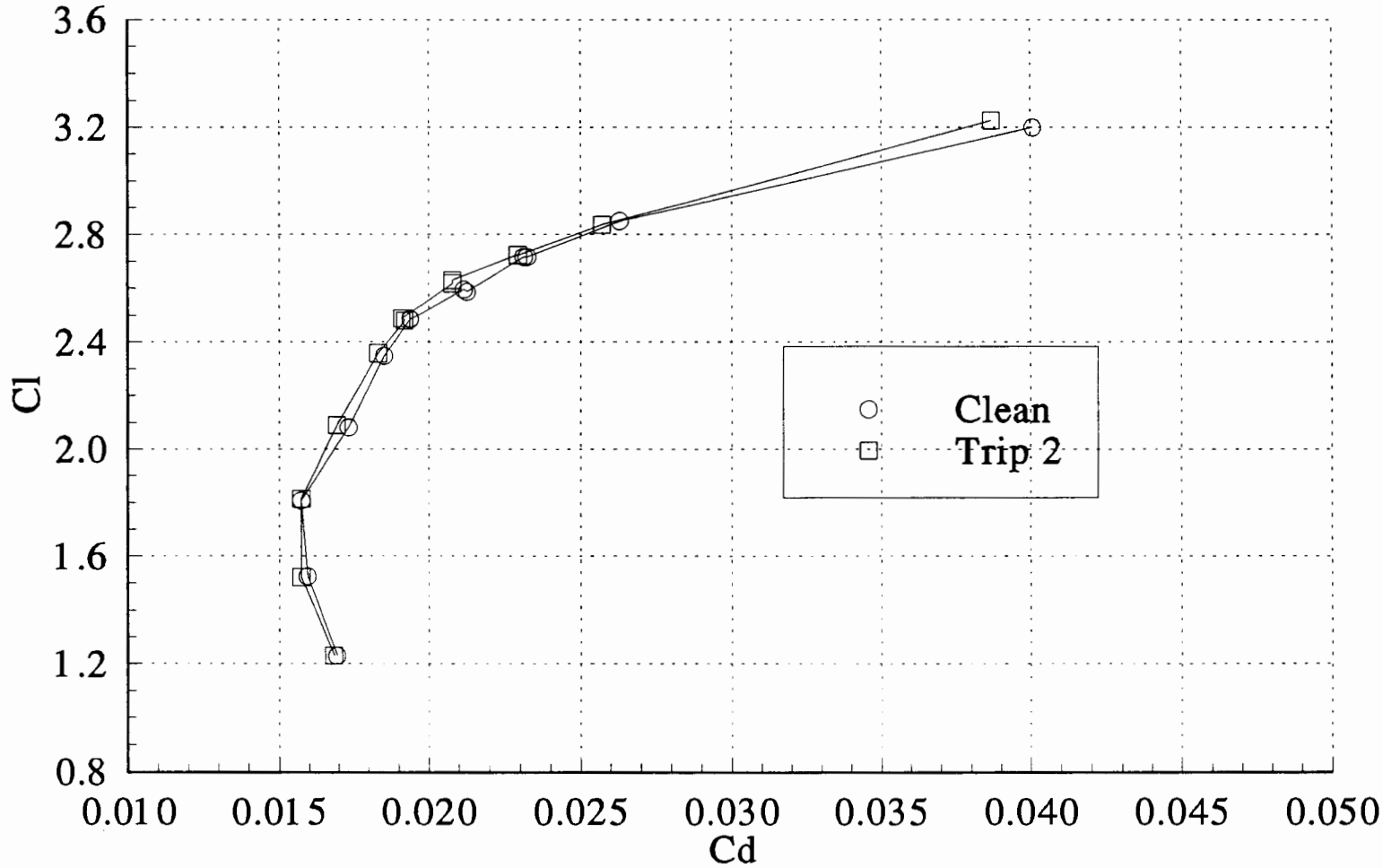

Figure 16. Slat closed comparison of drag polars for clean airfoil versus Trip 2 at Re=9M

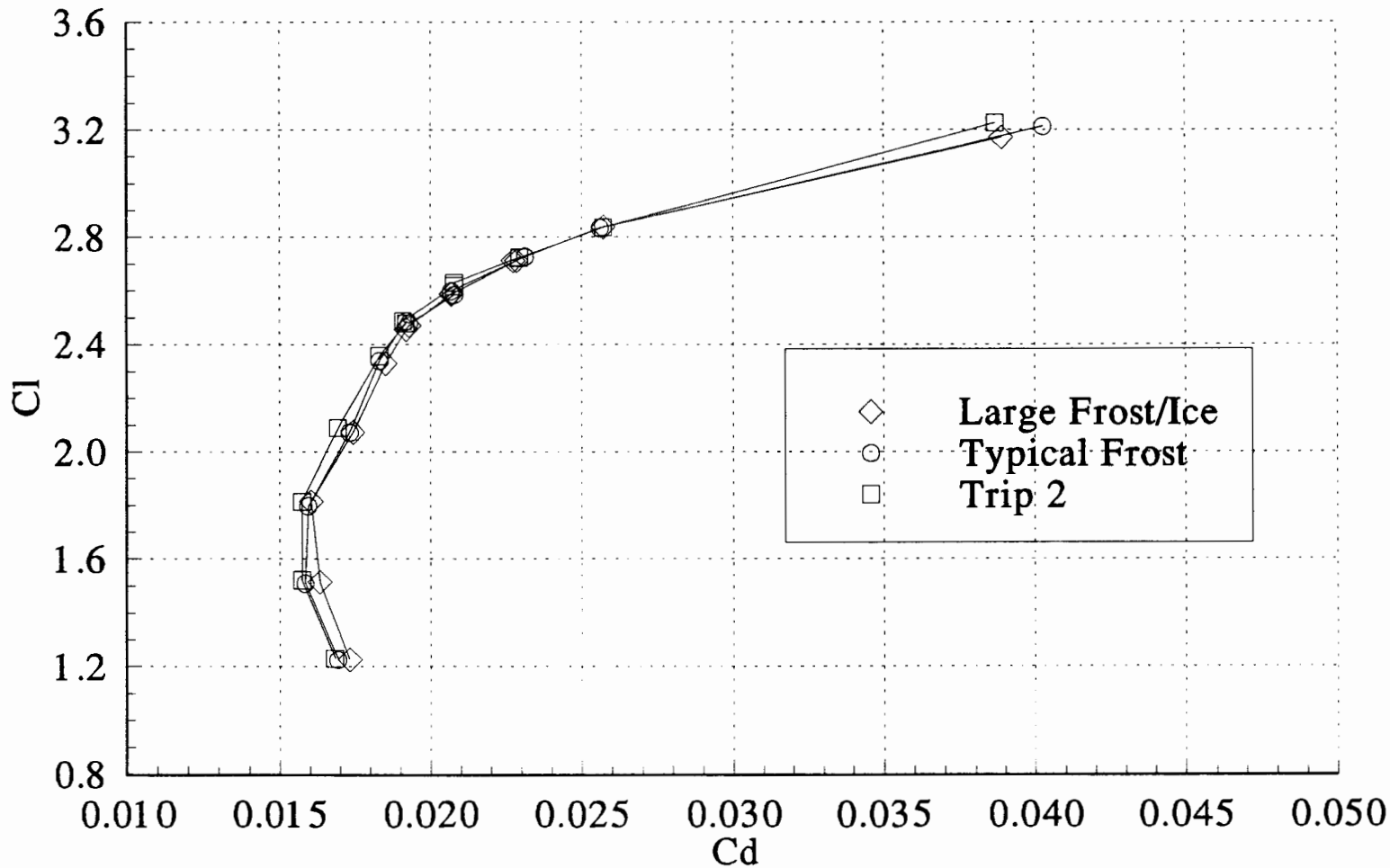

Figure 17. Slat closed comparison of drag polars for frost cases and trip 2 at Re=9M

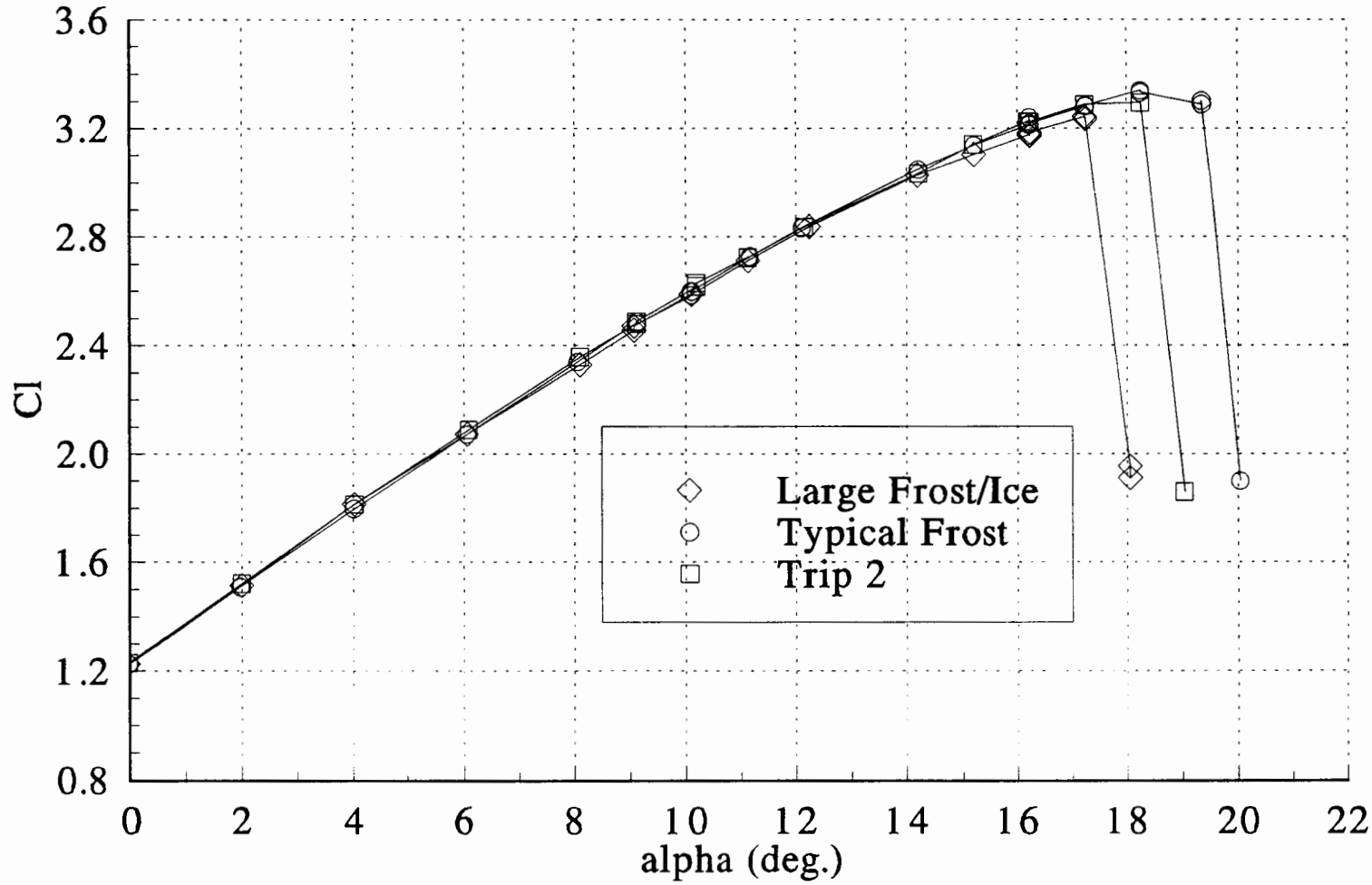

Figure 18. Slat closed comparison of lift curves for the frost cases and trip 2 at Re= 9M

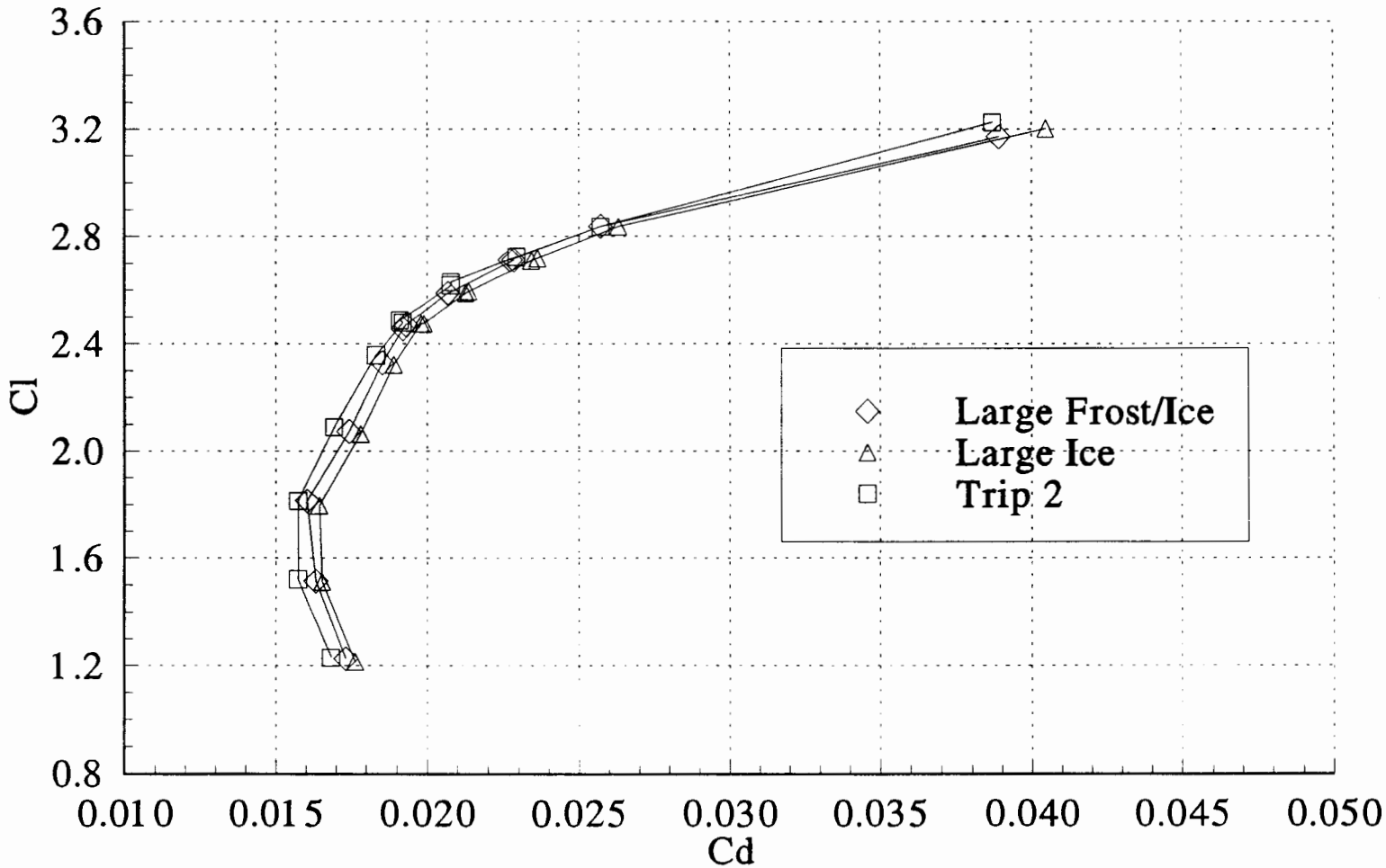

Figure 19. Slat closed comparison of drag polars for the ice cases and trip 2 at Re=9M

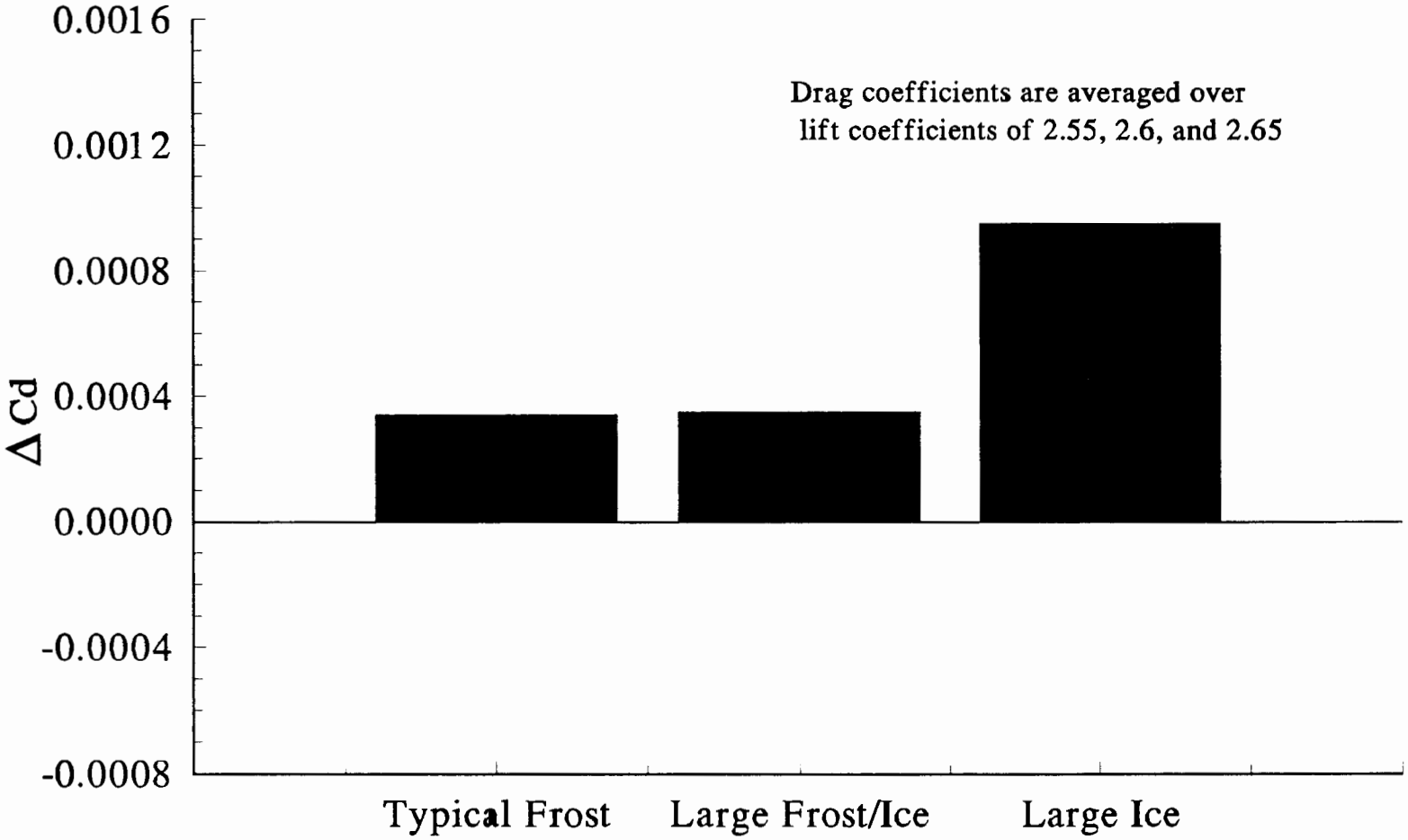

Figure 20. Drag coefficient increase from the slat closed trip 2 baseline at Re=9M

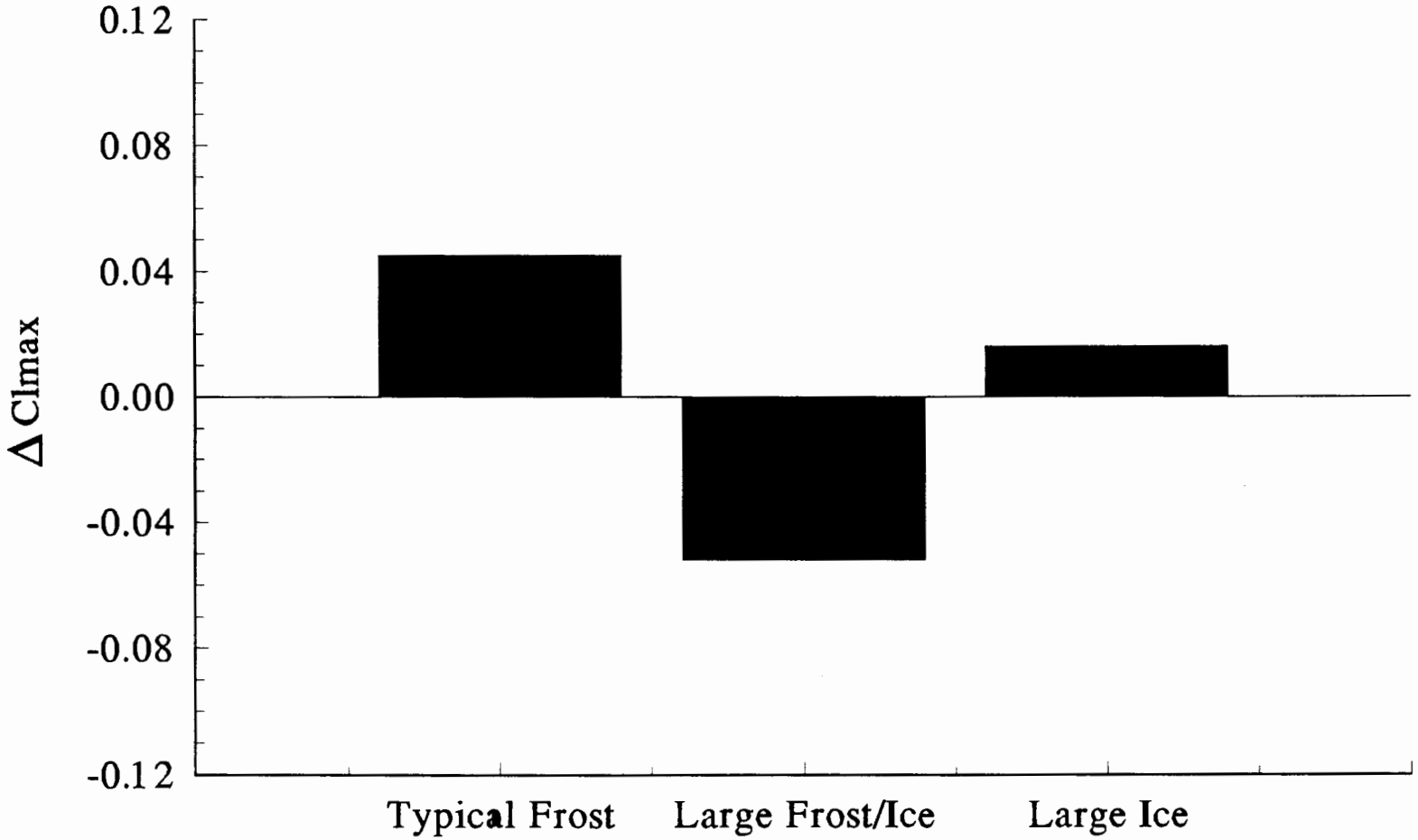

Figure 21. Max lift coefficient increase from the slat closed trip 2 baseline at Re=9M

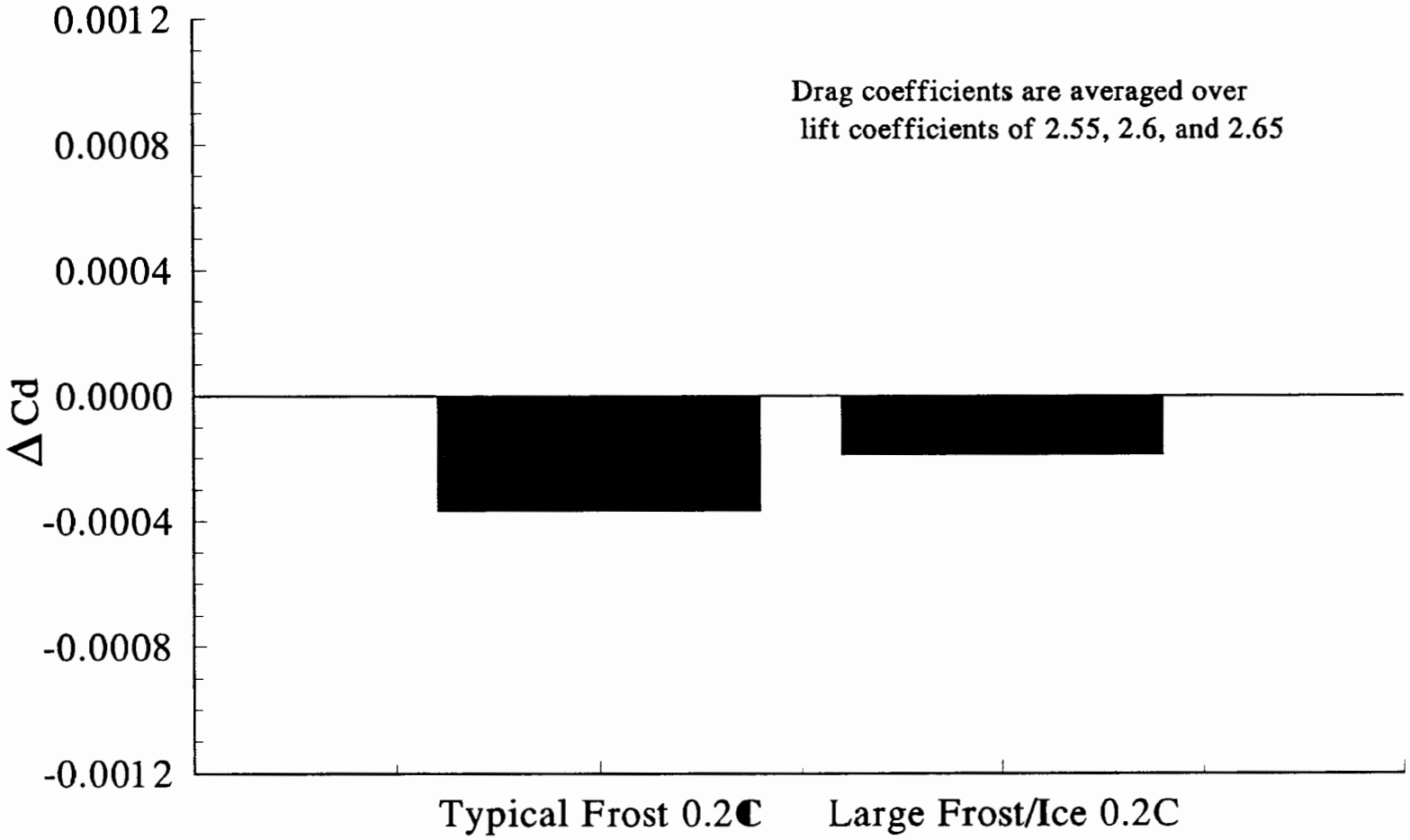

Figure 22. Drag coefficient increase from the slat closed trip 4 baseline at Re=9M

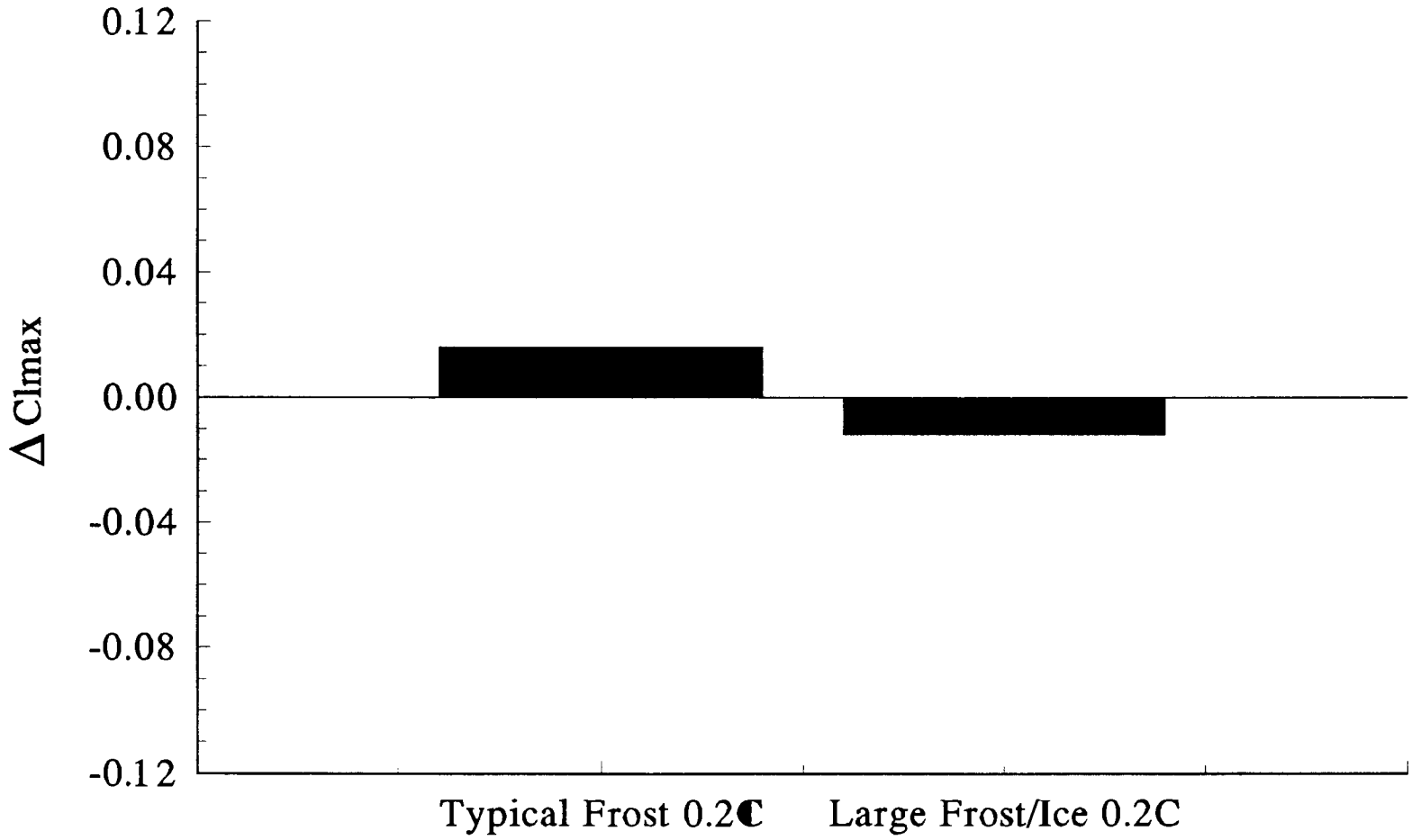

Figure 23. Max lift coefficient increase from the slat closed trip 4 baseline at Re=9M

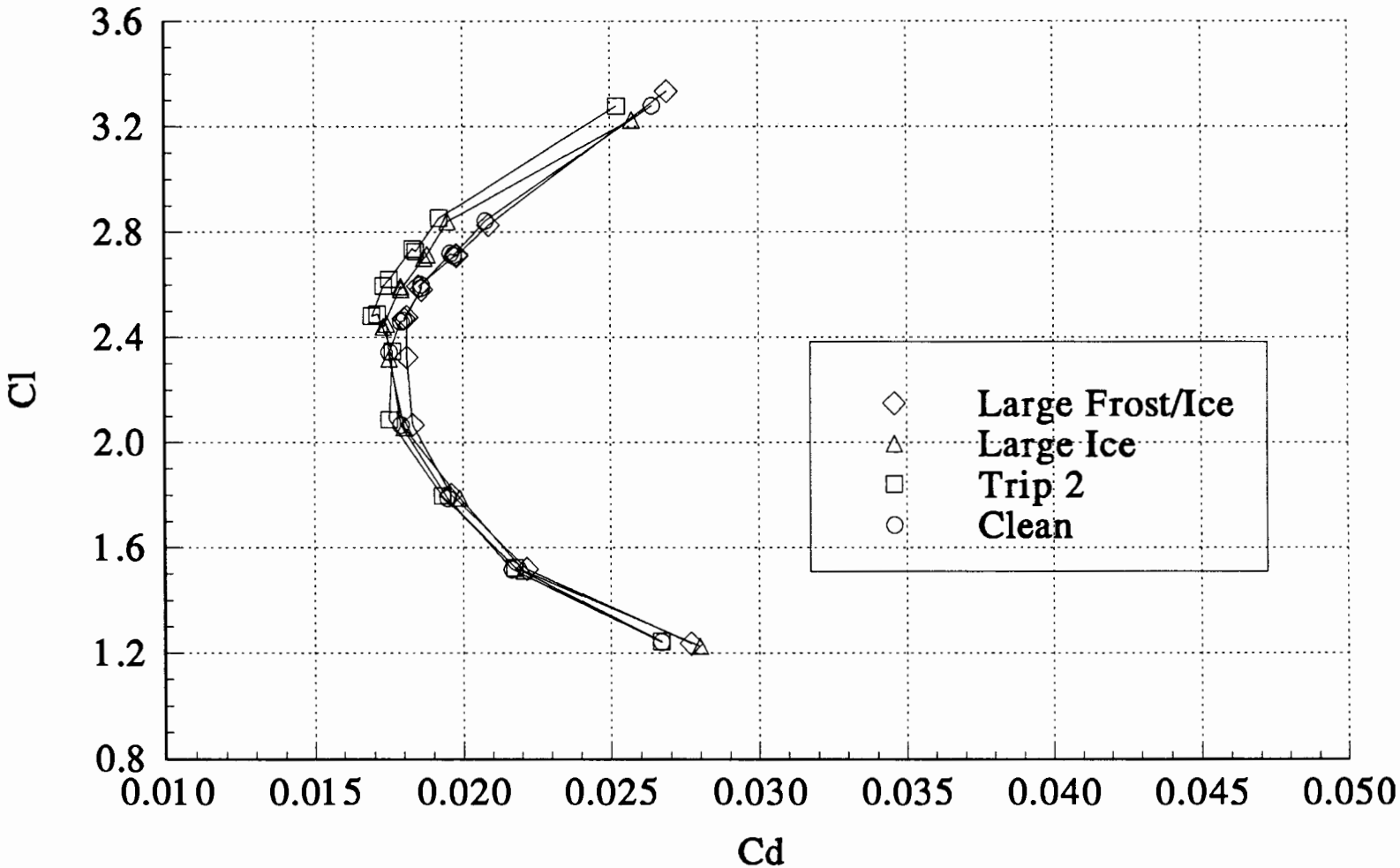

Figure 24. Slat open comparison of drag polars for the ice, trip 2 and clean cases at Re=9M

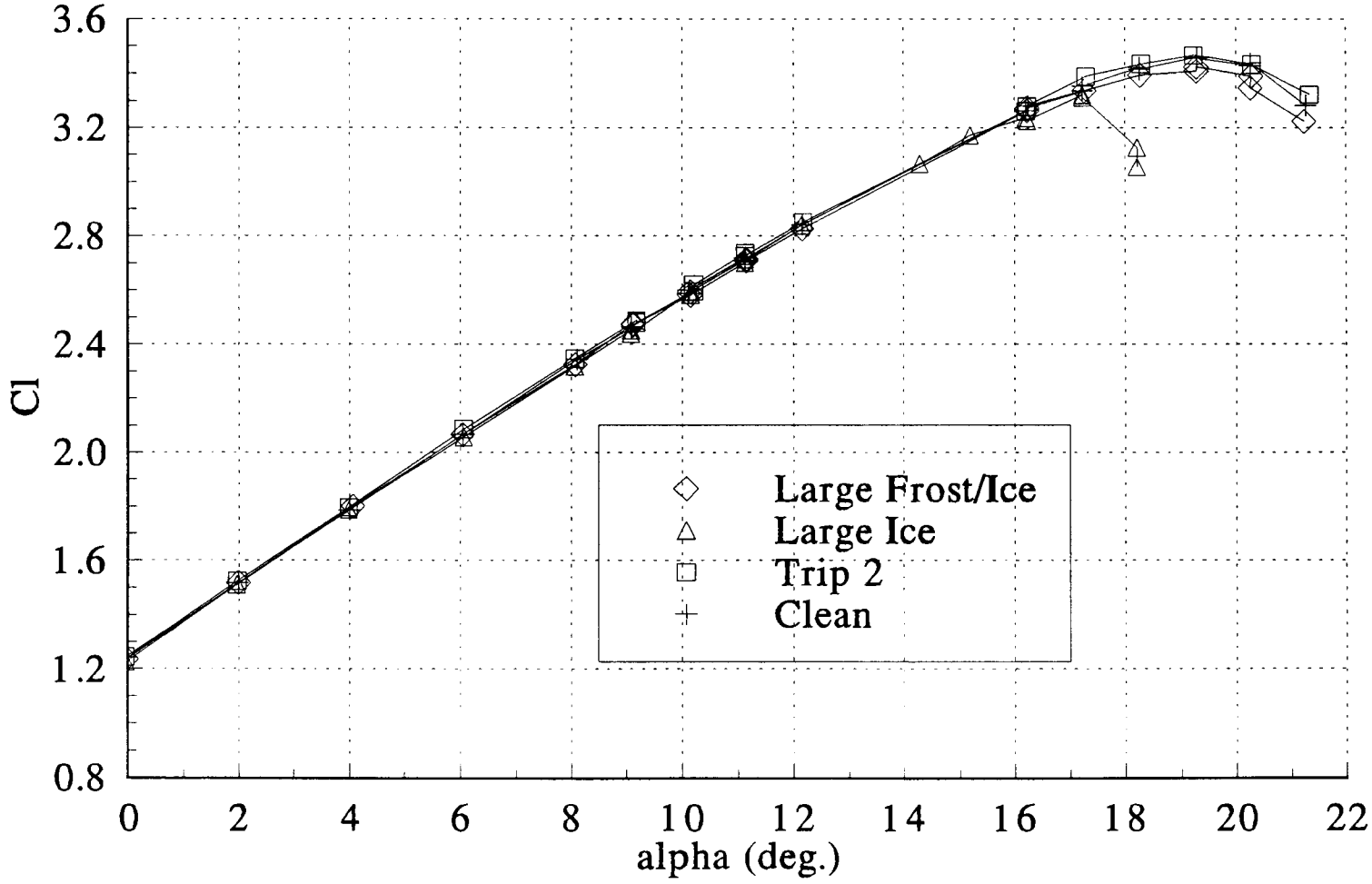

Figure 25. Slat open comparison of lift curves for the ice, trip 2 and clean cases at Re= 9M

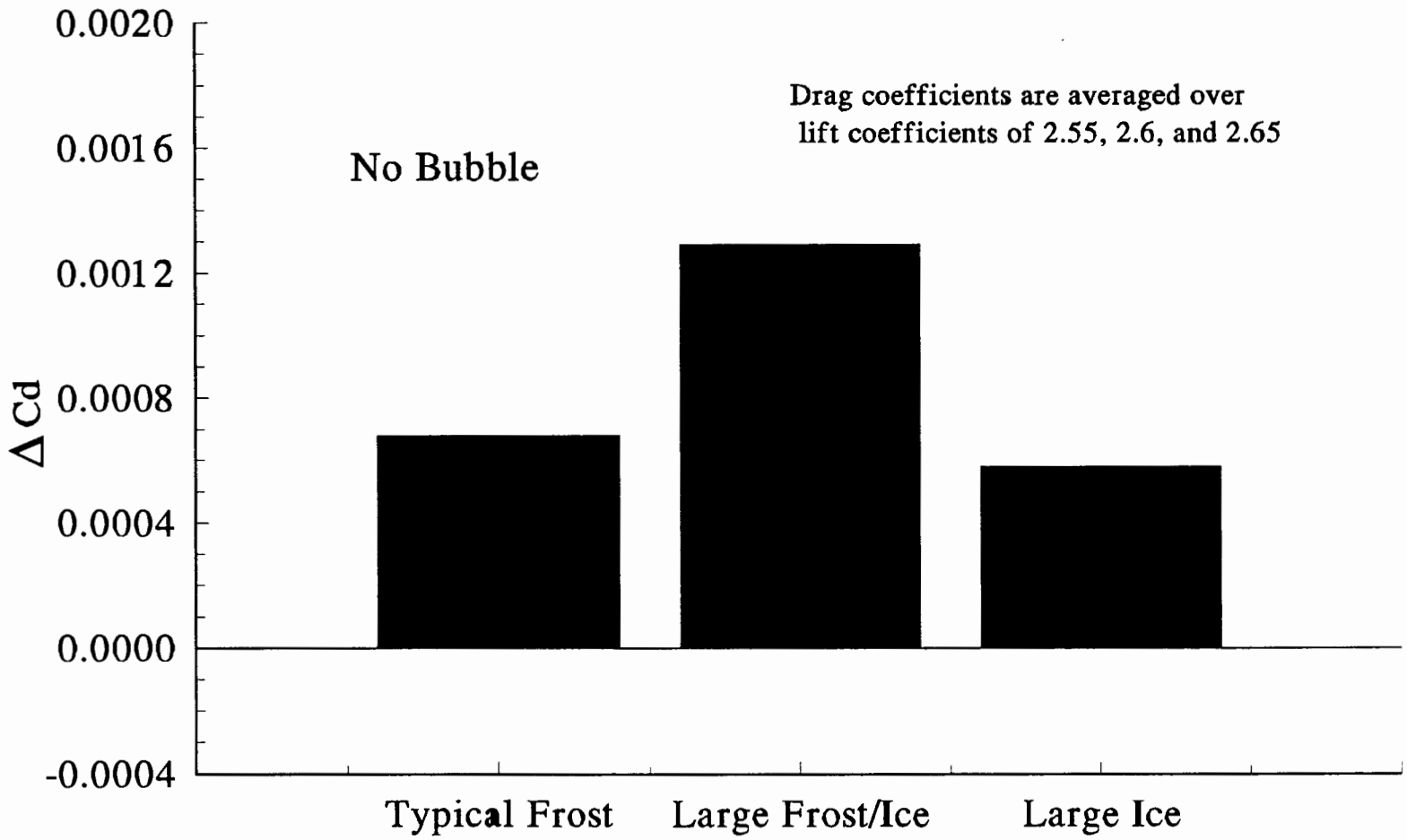

Figure 26. Drag coefficient increase from the slat open trip 2 baseline at Re=9M

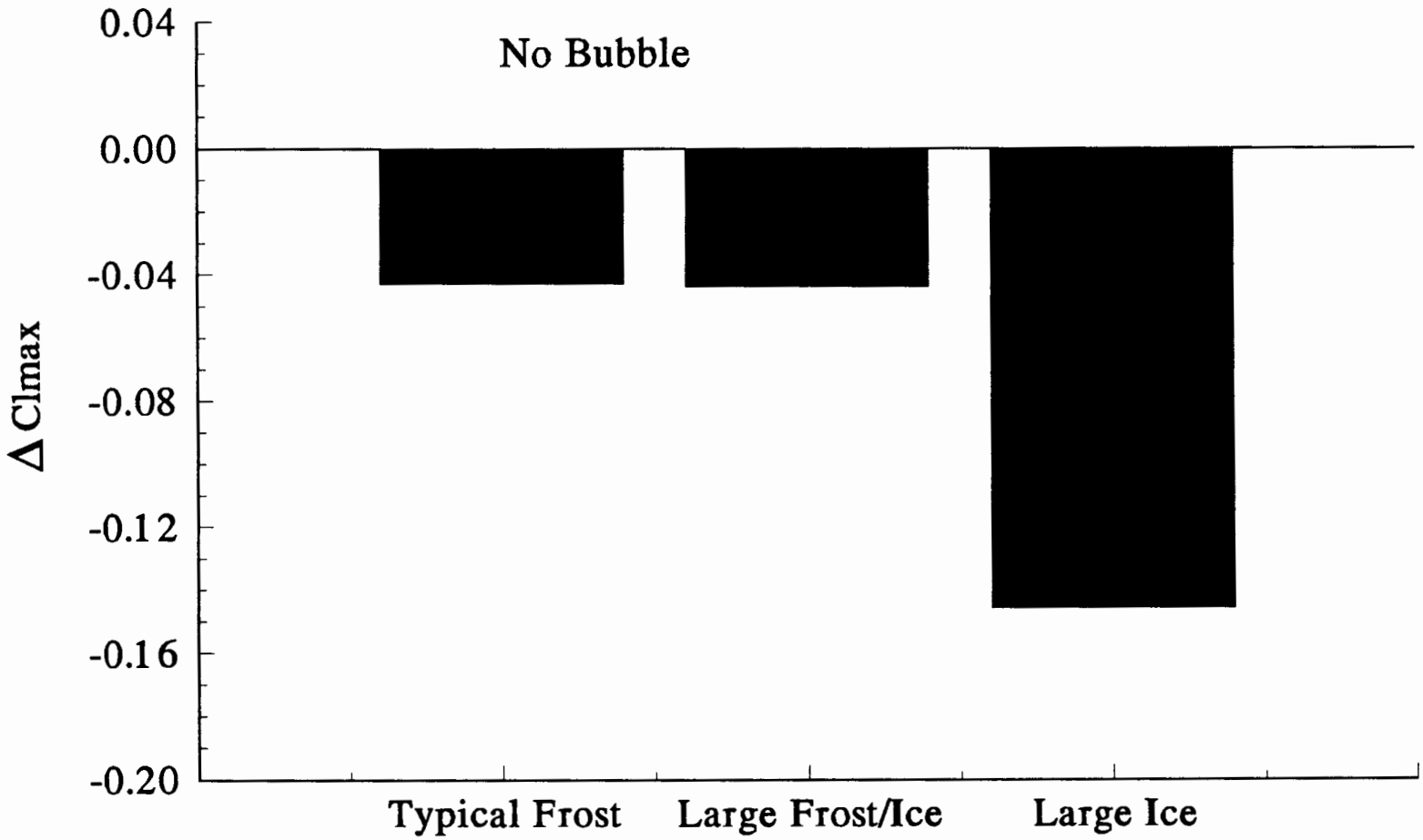

Figure 27. Max lift coefficient increase from the slat open trip 2 baseline at Re=9M

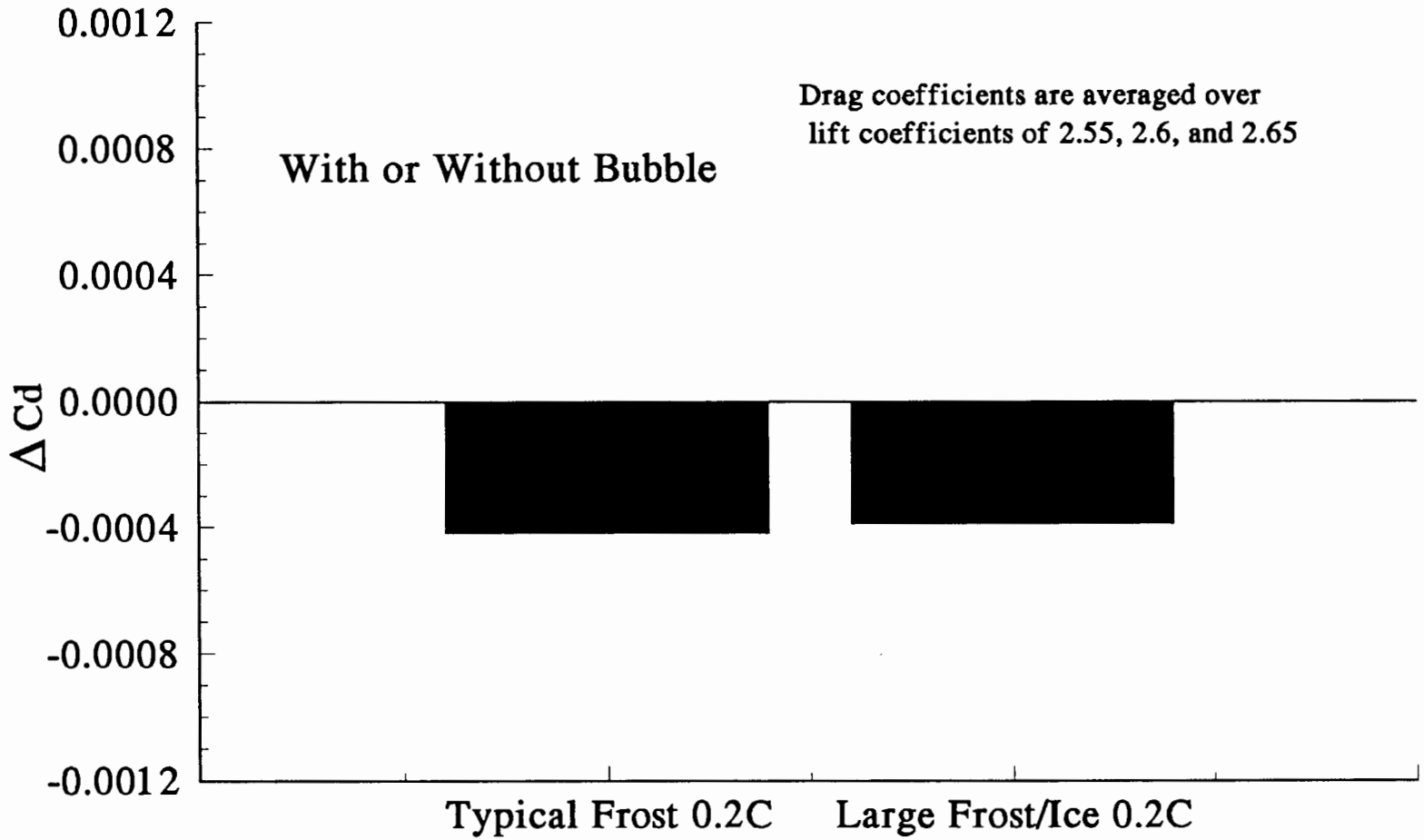

Figure 28. Drag coefficient increase from the slat open trip 4 baseline at Re=9M

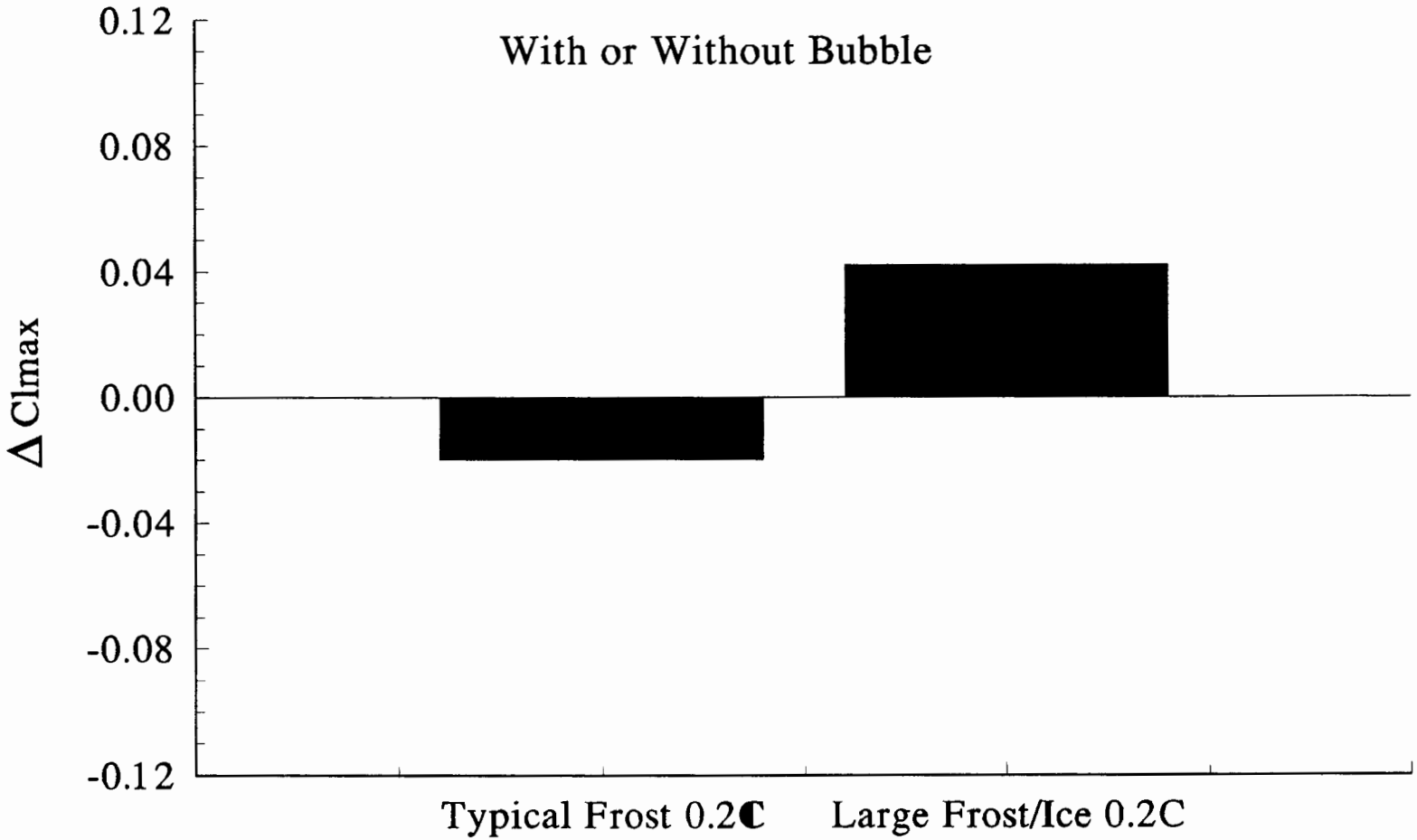

Figure 29. Max lift coefficient increase from the slat open trip 4 baseline at Re=9M

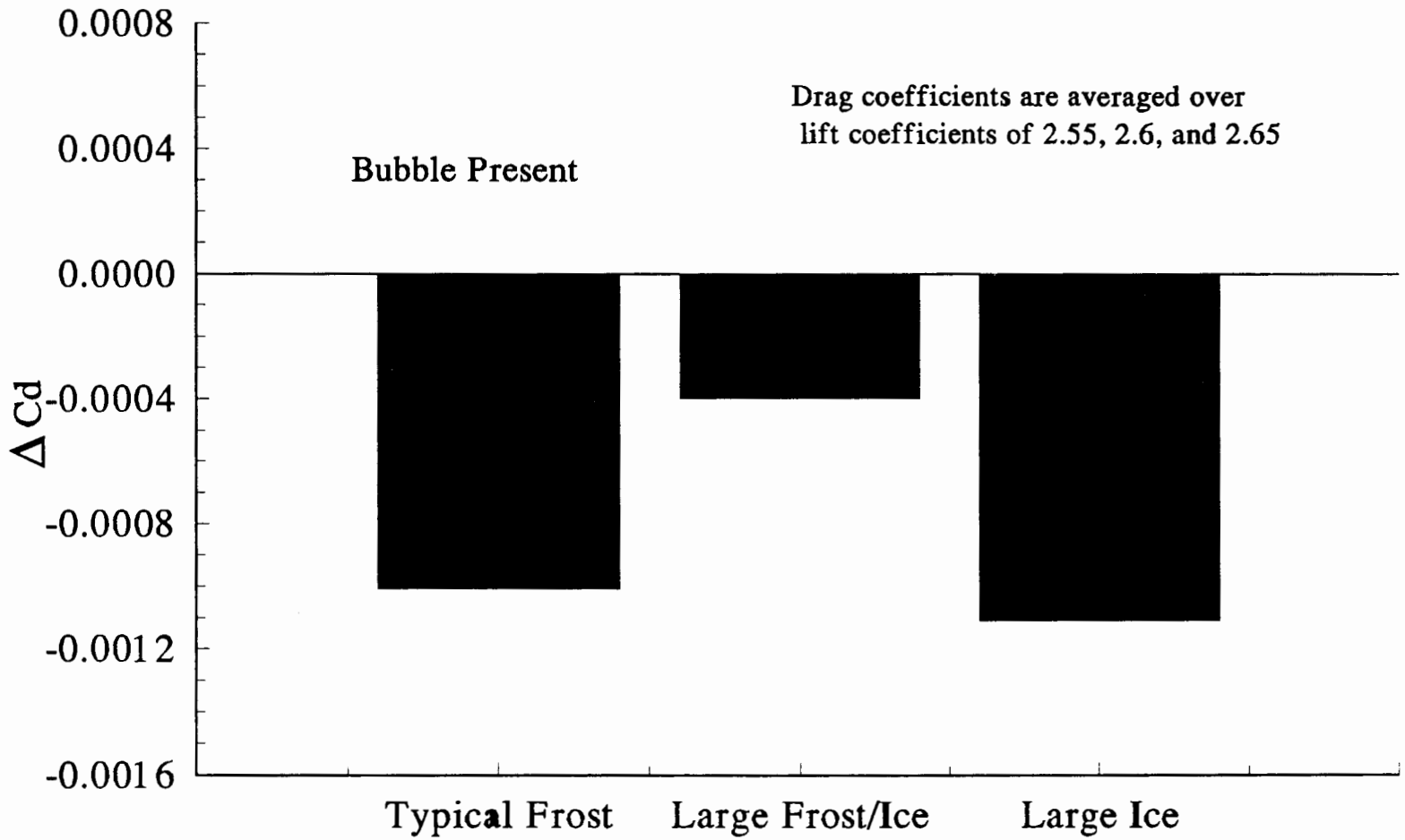

Figure 30. Drag coefficient increase from the slat open trip 4 baseline at Re=9M

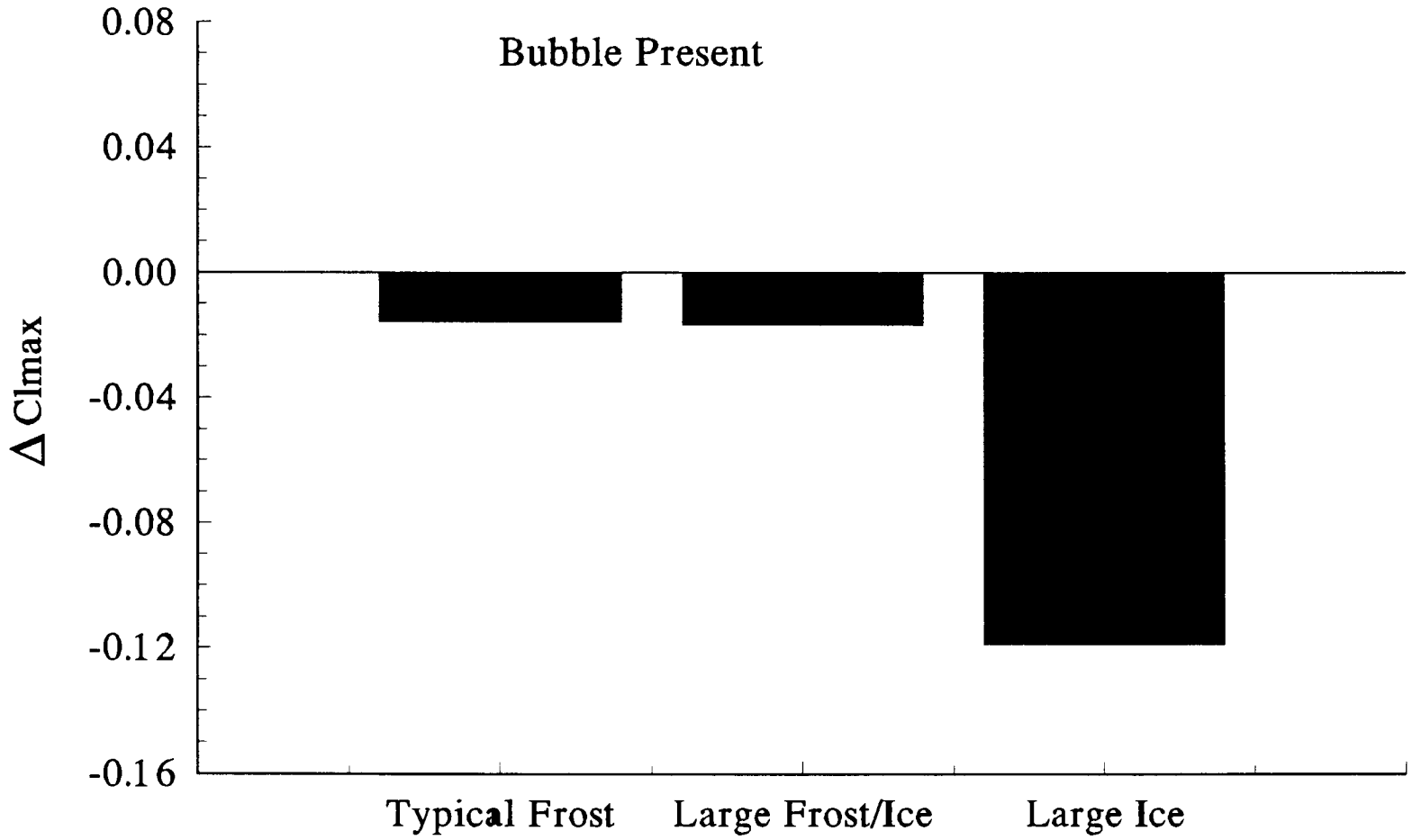

Figure 31. Max lift coefficient increase from the slat open trip 4 baseline at Re=9M

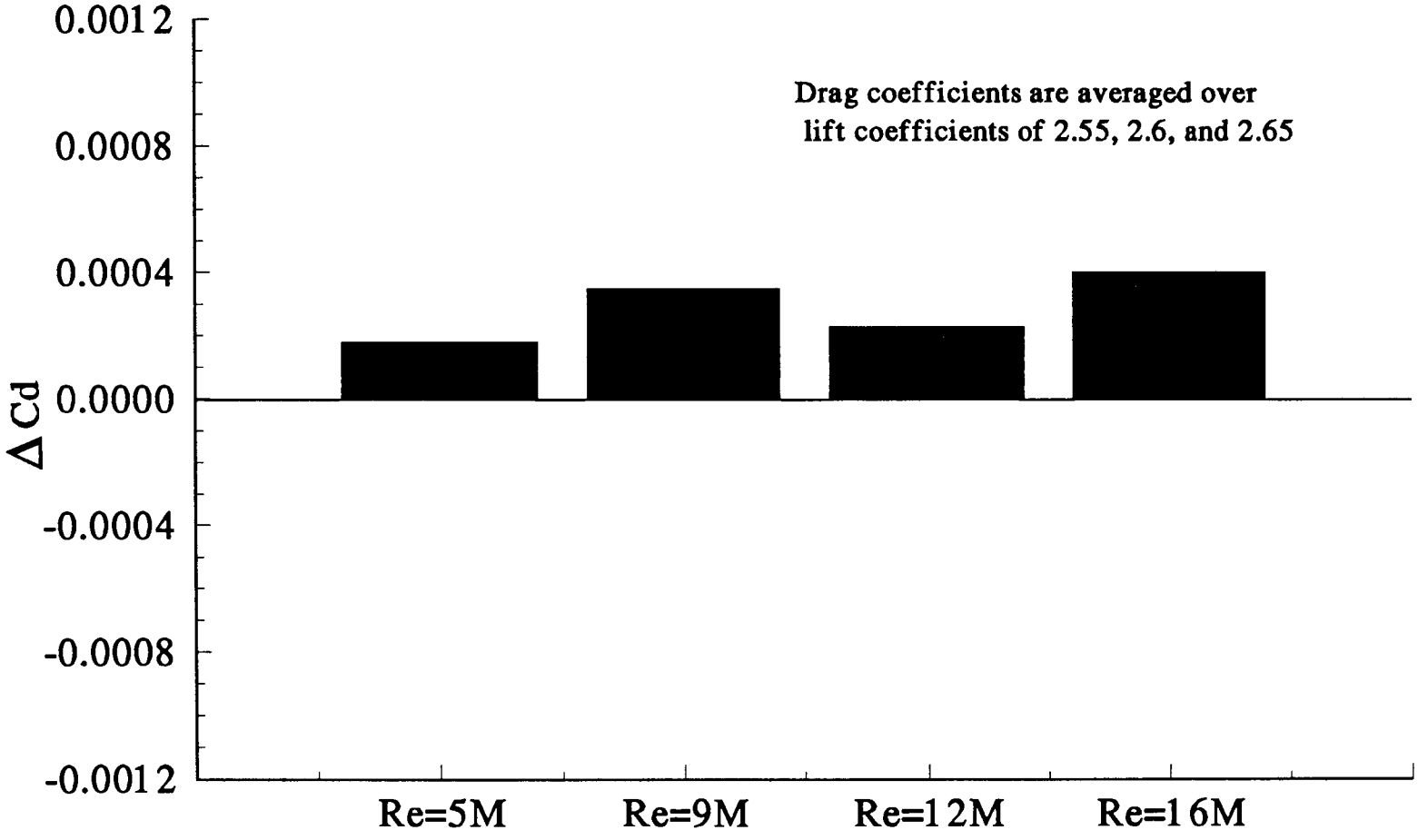

Figure 32. Drag coefficient increase from the slat closed trip 2 baseline for large frost/typical ice

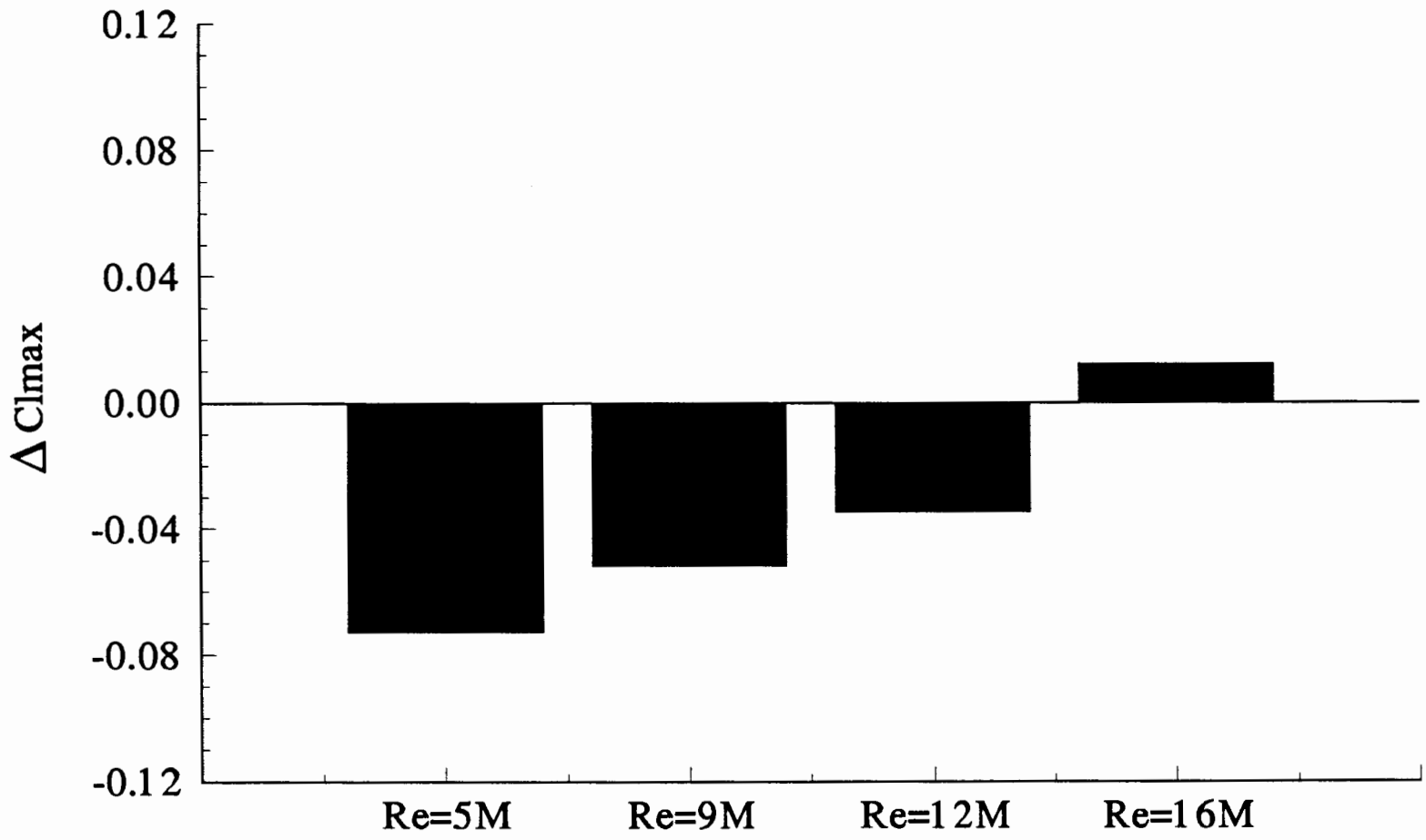

Figure 33. Max lift coefficient increase from the slat closed trip 2 baseline for large frost/typical ice.

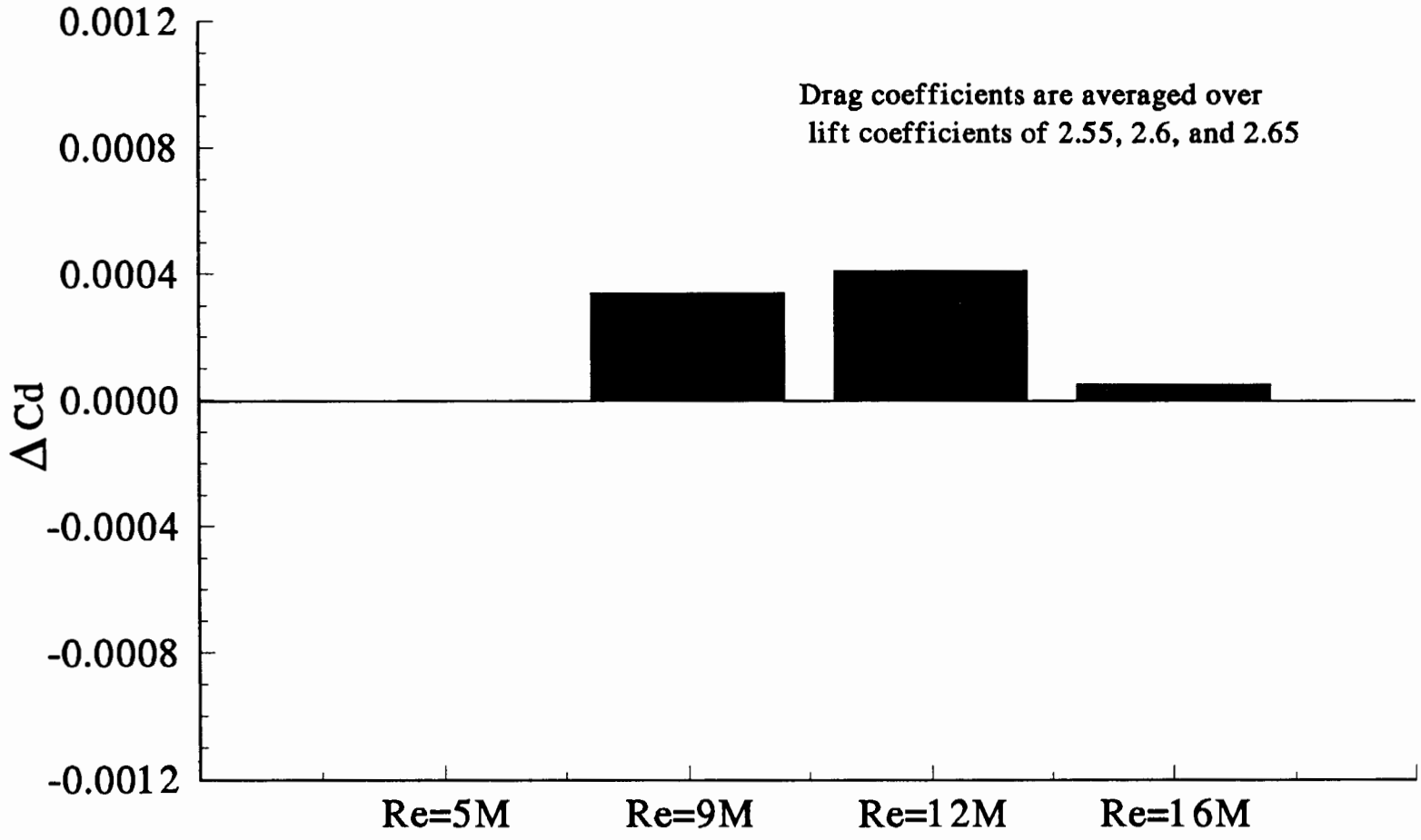

Figure 34. Drag coefficient increase from the slat closed trip 2 baseline for typical frost

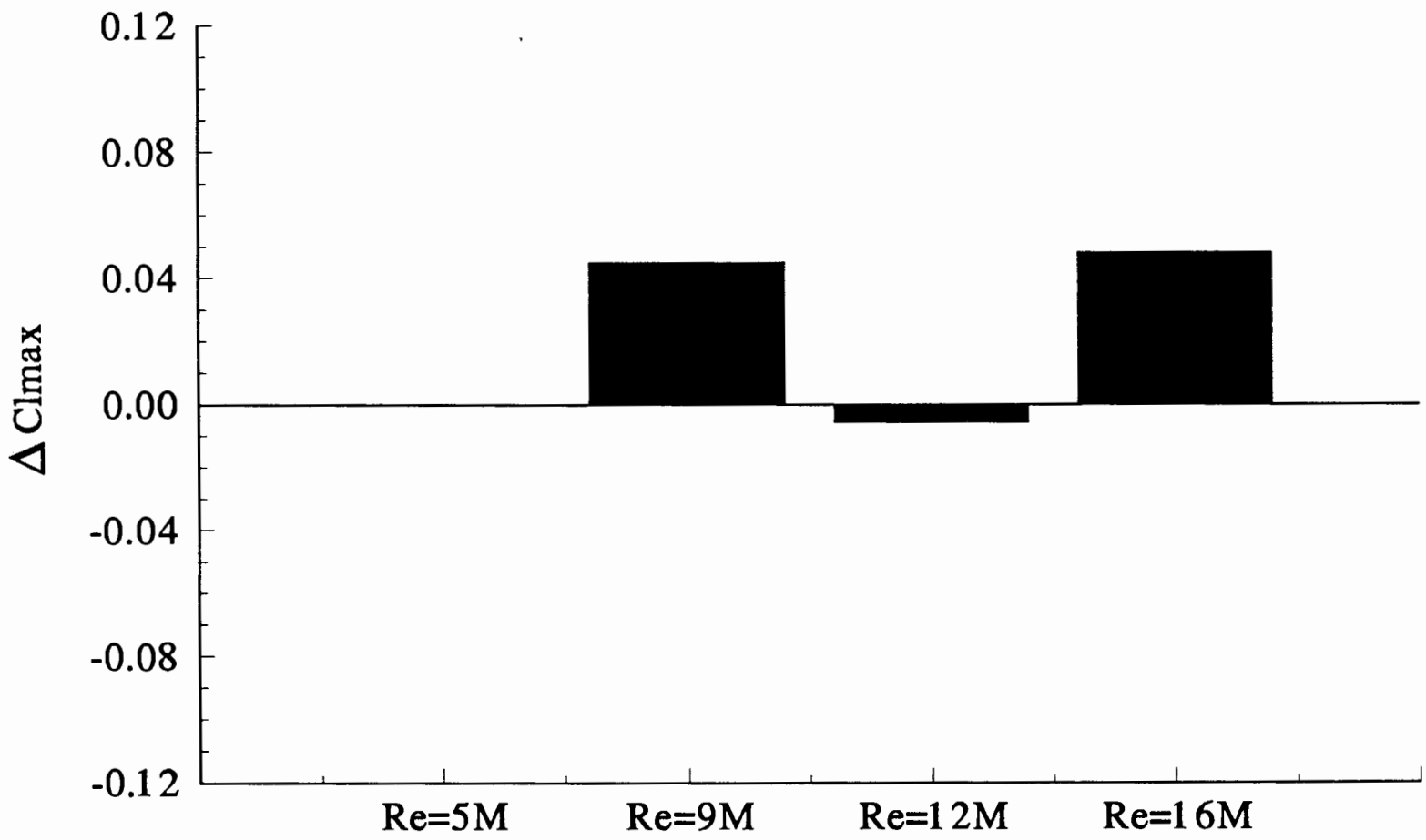

Figure 35. Max lift coefficient increase from the slat closed trip 2 baseline for typical frost

APPENDIX
REYNOLDS NUMBERS EFFECTS

The original test plan called for the slat closed data to be acquired at a Reynolds number of 16 million. However, the wind tunnel's main air compressor was not operational during the majority of the testing and therefore lower tunnel pressures and hence Reynolds numbers had to be used. All configurations were tested at 9 million and these are the data presented in the main body of this report. Reynolds number was varied for the typical frost and large frost/ice cases with the slat closed. The $\Delta C_{l,max}$ and ΔC_d data for these cases are shown in Figs. A.1, A.2, A.3, and A.4. The drag data for the large frost/ice case in Fig. A.1 shows no trend with Reynolds number within the repeatability of the data. In Fig. A.2 $\Delta C_{l,max}$ decreases (becomes a smaller negative number) as the Reynolds number increases. At 16 million the maximum lift of the model with the large frost/ice simulation is actually slightly higher than the baseline case. This trend is significant since it is larger than the data uncertainty of 0.03 and shows that the 9 million data are conservative.

Figures A.3 and A.4 show the drag and lift increments due to the typical frost simulation at 9, 12 and 16 million Reynolds number. The drag increments show no Reynolds number trend when the 0.0002 uncertainty is considered. The lift increments for this case do not show the same trend as in Fig. A.2, but instead no trend with Reynolds number is seen. Of the limited data available, only the maximum lift data for the large frost/ice simulation shows a significant Reynolds number trend. The other 3 cases do not. Based on the data presented here the Reynolds number effects on the high-lift airfoil with simulated lower surface frost or ice are inconclusive.

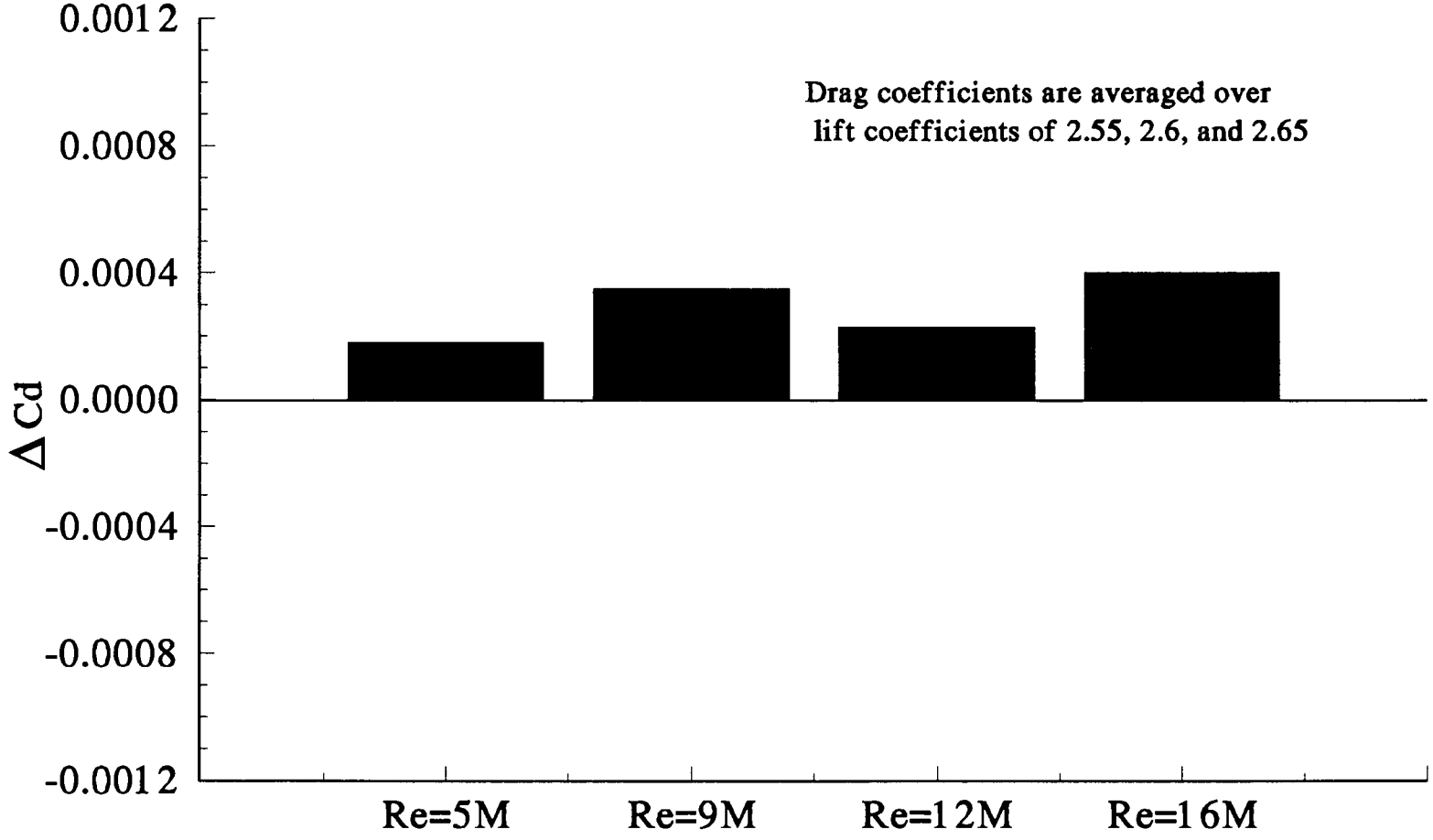

Figure A.1. Drag coefficient increase from the slat closed trip 2 baseline for large frost/typical ice

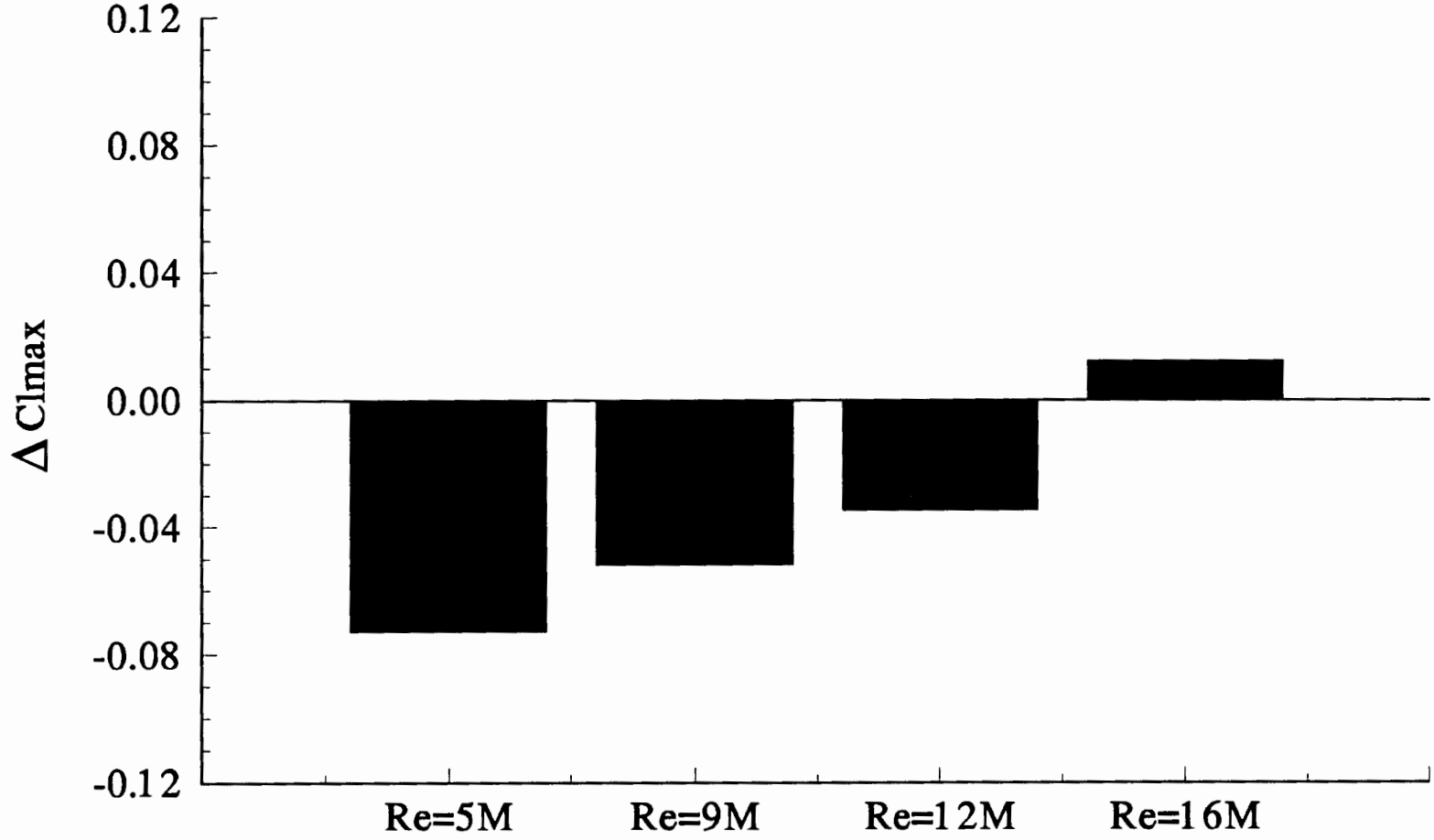

Figure A.2. Max lift coefficient increase from the slat closed trip 2 baseline for large frost/typical ice.

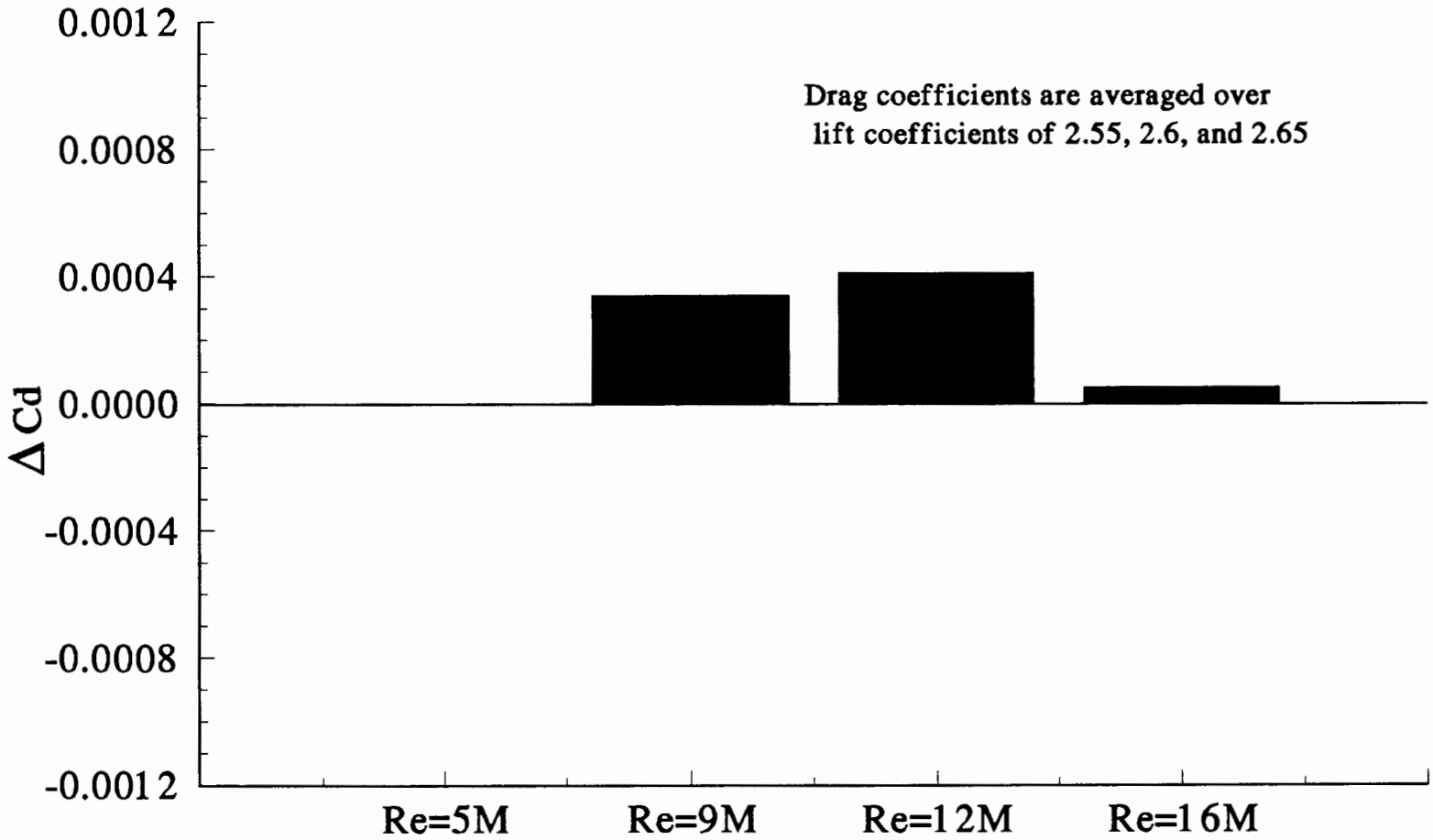

Figure A.3. Drag coefficient increase from the slat closed trip 2 baseline for typical frost

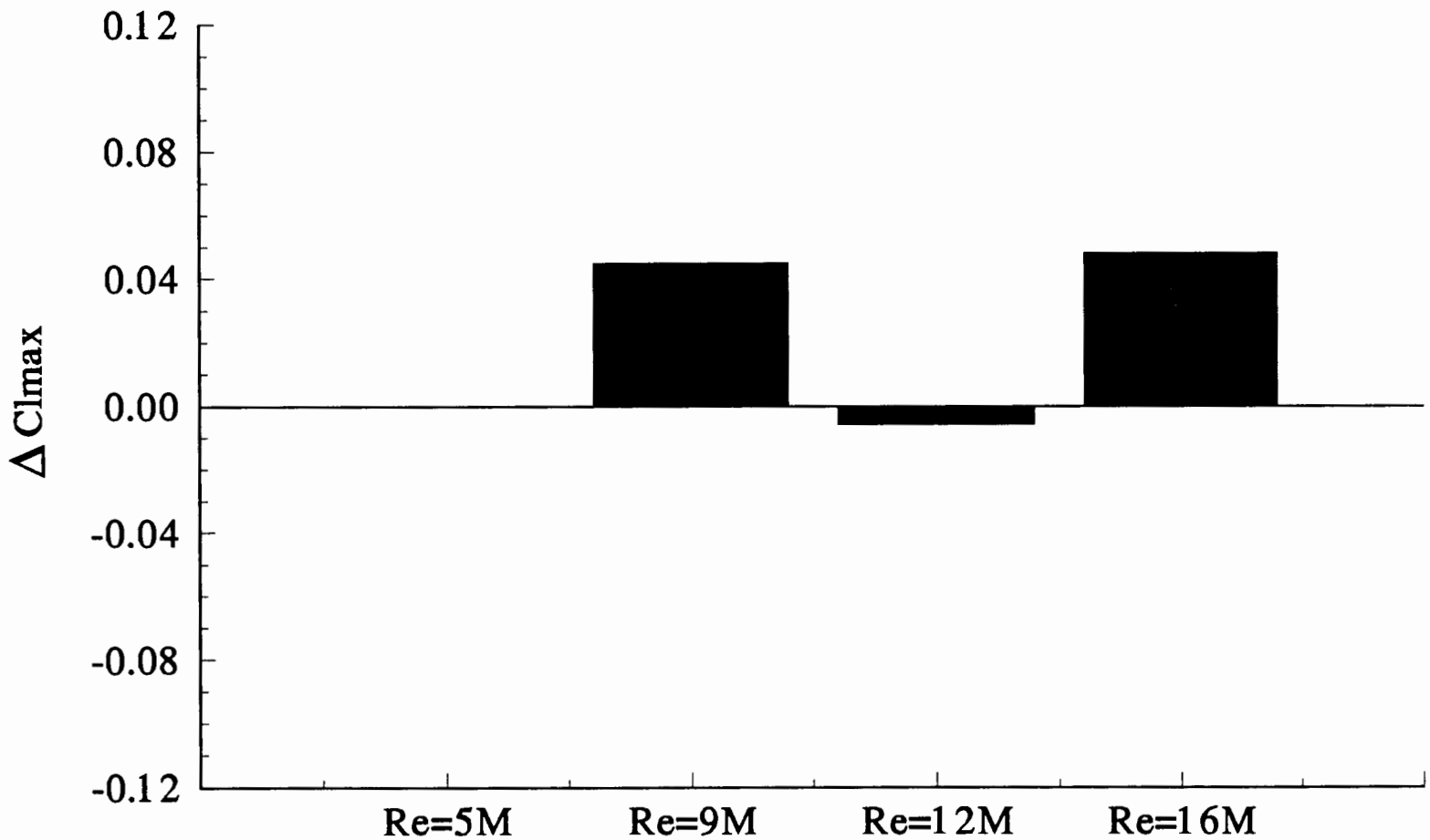

Figure A.4. Max lift coefficient increase from the slat closed trip 2 baseline for typical frost

☆U.S. GOVERNMENT PRINTING OFFICE: 1993 - 704-078/80056